3-D EXPERIMENTAL FRACTURE ANALYSIS AT HIGH TEMPERATURE

Supported by the
U.S. DEPARTMENT OF ENERGY
Grant Number DE-FG03-97ER14770

Final Report

A 3-DIMENSIONAL EXPERIMENTAL AND NUMERICAL ANALYSIS OF THE T^*_ε INTEGRAL IN ALUMINUM FRACTURE SPECIMENS

September 14, 2001

College of Engineering
UNIVERSITY OF WASHINGTON

University of Washington

Abstract

A 3-DIMENSIONAL EXPERIMENTAL AND NUMERICAL ANALYSIS OF THE T^*_ε INTEGRAL IN ALUMINUM FRACTURE SPECIMENS

By John H. Jackson and Albert S. Kobayashi

The T^*_ε integral, an elastic-plastic toughness parameter which is based on the incremental theory of plasticity, has been calculated experimentally and numerically in two-dimensional (2-D) metallic specimens. These established methods for 2-D characterization of the T^*_ε integral are used to expand this relatively new elastic-plastic toughness parameter to 3-D elastic-plastic fracture problems. This is a necessary step toward completely validating T^*_ε integral as an elastic-plastic toughness parameter capable of characterizing unloading and crack propagation. Since the T^*_ε parameter was originally derived to overcome inherent shortcomings involved with the use of creep fracture toughness parameters such as the C^* integral, its use in creep fracture is also briefly reviewed.

The early foundation that has been set for the T^*_ε integral is further expanded in this dissertation as a viable alternative to the J-integral for use as a toughness characterizing parameter in the presence of a 3-D flaw. Since the J-integral is based on the deformation theory of plasticity, it lacks the capacity for characterizing a growing flaw that will inevitably include unloading and extensive plasticity. Further, the J-integral is calculated along a constant sized contour that moves with the crack tip, meaning it is a measure of only the energy release rate at the crack tip. The T^*_ε integral approach attempts to overcome these drawbacks by utilizing incremental (flow) plasticity and a growing integration contour to capture the material behavior at the advancing crack tip as well as behind. A 2024-T351, aluminum alloy, which is considered a ductile material, is used for

proof of concept in this study. The research includes experimental work for validation of, and application to, a numerical model in a generation phase approach for a toughness-characterization curve. Issues including near field integration contour size, method of calculation, and comparison between near, and far field *J*-integral and T^*_ε are discussed. An extensive numerical study including the calculation of the T^*_ε contour integral via the equivalent domain integral (EDI) method is performed to meet this end.

A numerical model is built incorporating tunneling behavior observed in experimental work. The behavior in a case of extreme tunneling is relatively unknown so attempts are made wherever possible to compare to baseline behavior of established parameters. Comparisons are made between T^*_ε calculated along an idealized straight crack front, deformation theory *J*-integral along an idealized straight crack front, incremental *J*-integral calculated in the extreme tunneling case, and T^*_ε calculated using nodal displacements and the deformation theory of plasticity on a truncated contour. The T^*_ε integral is observed to behave similarly in a qualitative sense to the *CTOA* for the case of extreme tunneling and as the mid-plane of the specimen is approached. The T^*_ε calculated on the surface of the specimen with experimentally obtained surface displacements is found to compare quantitatively with near surface, numerically obtained, T^*_ε values.

TABLE OF CONTENTS

LIST OF FIGURES

Number *Page*

LIST OF TABLES

LIST OF ABBREVIATIONS

COA	Crack Opening Angle
COD	Crack Opening Displacement
CMOD	Crack Mouth Opening Displacement
CN	Center Notched
CT	Compact Tension
CTOA	Crack Tip Opening Angle
CTOD	Crack Tip Opening Displacement
EDI	Equivalent Domain Integral
FEA	Finite Element Analysis
SENB	Single Edge Notched Bend
VCE	Virtual Crack Extension

1

INTRODUCTION

Nonlinear behavior in fracture has been a topic of recent interest, as current knowledge in this area is known to be inadequate. Most agree that fracture mechanics, as it pertains to the extension of a crack in a material, is well established only to the point of fracture initiation. Beyond crack initiation, and with large-scale plastic deformation, even the well-known *J*-integral approach loses its validity. Hence, an important class of materials, namely those exhibiting lower strength and high toughness in which crack instability may be preceded by extensive stable tearing, are largely uncharacterized. Alternative fracture parameters must be explored in order to overcome these difficulties associated with the development of large plastic zones and to allow characterization of toughness in materials exhibiting extensive stable crack growth.

The concepts of damage tolerance, and life extension are closely tied in with the need to characterize the regime of stable crack extension. In applications utilizing ductile materials (high toughness), i.e. boiler pressure vessels, aircraft skins, etc., the ability to predict the behavior of an existing, growing flaw is of utmost importance. As noted by Dawicke et al [1], residual strength prediction in an aircraft fuselage requires a fracture criterion capable of accounting for large-scale stable tearing in thin-sheet materials. It is apparent that, in comparison to elastic (brittle) fracture, relatively few studies involving toughness characterization beyond the small-scale yielding regime have been performed [2]. Thus, in recent years, several stable tearing toughness parameters have been proposed.

This research is intended to be an exploration of the existing stable crack tearing characterizing parameters through an experimental-numerical study aimed at extending the capabilities of elastic-plastic fracture to encompass stable tearing behavior. This will include an extension of 2-D to 3-D analyses. Recent experimental results are reviewed, and the current research is explained in detail in this chapter.

CHAPTER 1: REVIEW OF CURRENT KNOWLEDGE

1.1 CRACK TIP GEOMETRY PARAMETERS

1.1.1 COD AND CTOD

Beginning with the work of Wells [3] in 1961, crack tip geometry parameters were viewed as possible means of characterizing toughness in the event of large plastic deformation. The first of these parameters was designated as Crack Opening Displacement (*COD*), and was observed to be somewhat of a material constant which could be reliably measured, even in the presence of significant yielding [3, 4]. It was noticed that, once initiated, a crack propagates with a characteristic bluntness, leading to the concept of a material dependent, critical *COD* [2]. *COD*, as it is used in this context, is typically measured very close to the crack tip and is therefore also referred to more accurately as Crack Tip Opening Displacement (*CTOD*). Figure 1.1 is a graphical definition of *CTOD* or *COD* and Crack Tip Opening Angle (*CTOA*), which will be discussed shortly.

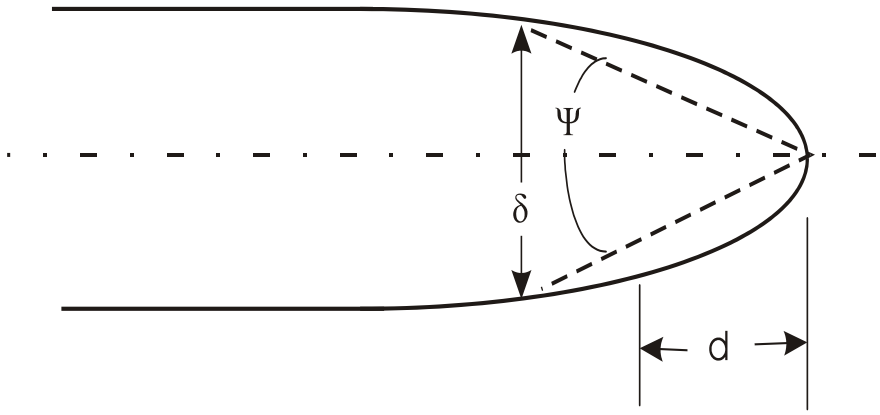

Figure 1.1: Definition of CTOD and CTOA.

CTOD is typically applied in instances of small scale yielding where it may be related to Griffith's energy release rate as in equation (1.1) with Irwin's plastic zone correction, or equation (1.2) with the strip yield model [5]. Here, G is Griffith's energy release rate, σ_{YS} is the yield strength, and m is a parameter set equal to 1.0 for the case of plane stress, and 2.0 for the case of plane strain.

$$\delta = \frac{4}{\pi}\frac{G}{\sigma_{YS}} \tag{1.1}$$

$$\delta = \frac{G}{m\sigma_{YS}} \tag{1.2}$$

In addition, *CTOD* may be related to Rice's *J*-integral [6] as in equation (1.3). Here λ is a material dependent parameter.

$$\delta = \frac{J}{\lambda\sigma_{YS}} \tag{1.3}$$

Although *CTOD* is a direct function of the *J*-integral through equation 1.3, this relationship is no longer valid in the presence of unloading or crack extension, thus CTOD will not inherit the many difficulties relating to the use of *J*-integral as a fracture toughness characterization. Critical *CTOD*, measured at the initiation of stable fracture, corresponds to critical *J* (J_{IC}).

Typically, *CTOD* is applied in what is known as a *COD* design curve approach. This approach, originally developed by Burdekin and Dawes [7], involves plotting critical CTOD normalized by the half crack length against the failure strain normalized by the elastic yield strain [5]. Any state of stress lying above this design curve was considered safe because all observed experimental failures were below the curve. It is noted that, when producing a *COD* design curve, the specimen tested must be of the same thickness

as the structure to which the design curve is applied. Accordingly, it is necessary to carry out tests on materials representing different regions within a component [5].

1.1.2 CRACK TIP OPENING ANGLE (CTOA)

A more recently studied, similar parameter that has been found to be significant in terms of quantification of stable crack extension is the Crack Tip Opening Angle (*CTOA*). This is defined in either of two ways, as a Crack Opening Angle (*COA*), which is the ratio of the original *CTOD* to the crack extension, or strictly as *CTOA* (local *COA*) which is a measure of the angle of the crack face immediately behind the current crack tip [8]. Obviously, measurement becomes more difficult as the crack tip is approached and the crack tip behavior becomes more detached from measurement as a crack extends. Thus, *CTOA* is typically measured as close to the crack tip as is convenient within the capability of experimental measurement so that accuracy may be maintained. As noted by Shih et al [9], the opening profile has a vertical tangent right at the crack tip, corresponding to a *CTOA* of 180 degrees. Therefore, the *CTOA* must be defined at a small, but reasonably finite distance from the extreme tip in order to have meaning. *CTOA* (ψ) is typically defined as in equation (1.4), using *CTOD* (δ) measured a specified distance (d) from the current crack tip.

$$\psi = 2\tan^{-1}\left(\frac{\delta/2}{d}\right) \tag{1.4}$$

Shih et al [9], provide one of the first significant studies in which the *CTOA* (or *COA*) was utilized as a toughness parameter in studies of stable crack extension. Results were compared with five different fracture criteria, including *CTOA* for A533B steel Compact Tension (CT) specimens and Center Cracked (CN) panels. In their computational approach, two different measures of *COA* were employed for comparison with experimental results. The first is an average *COA* based on the crack extension (a-a_0) measured from the original crack tip, and on the *COD* (δ_0) measured at the original crack

tip. The second is a so-called local *COA* (or *CTOA*) based on the opening displacement δ_l measured at a fixed distance, Δa, behind the current crack tip. These are similar measurements at slightly differing scales. Both the local *COA* (*CTOA*), and average *COA*, denoted α_l and α_0, respectively, showed considerable variation between experimental and numerical results near initiation but exhibited a leveling off trend as the crack extended in a stable fashion (Figure 1.2). The *CTOA* was found to be mildly sensitive to the mesh size in the finite element model, but was seen as a better measure of the local deformation characteristics. Based on this work, a *CTOA* modulus approach to stable tearing was proposed as an alternative to the previously used, *J*-integral based tearing modulus (*dJ/da*). Equation (1.5) is the proposed *CTOA* based tearing modulus, where it is seen that the *CTOA* ($d\delta/da$) must be very large in comparison to the yield strain. The *CTOA*, as it is used here, was also observed to be mildly dependent on the specimen geometry, which is seen as a drawback in terms of its use as a stable tearing characterization parameter. However, the achievement of a steady state value is a favorable characteristic for stable tearing.

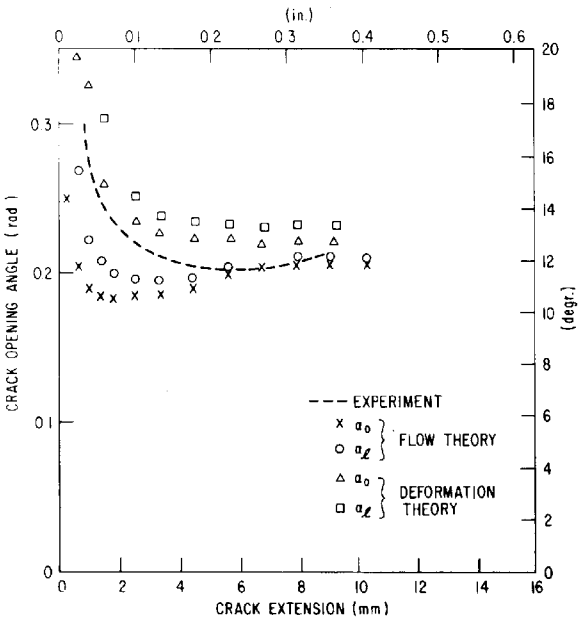

Figure 1.2: CTOA (α_0) and COA (α_l) [9].

$$T_\delta = \frac{d\delta}{da}\frac{E}{\sigma_0} >> 1 \qquad (1.5)$$

In a similar study, Kanninen et al [10] used "generation" and "application" phase finite element analysis (FEA) studies to observe various elastic-plastic fracture criteria, including *COA* and *CTOA*. In this procedure, the "generation" phase consists of matching FEA values of load or displacement and crack extension for differing criteria, with experimentally observed values. In the "application" phase, these previously evaluated parameters are applied to predict the fracture behavior. In the same spirit as the study discussed previously, a set of 'valued' criteria are outlined, and the various elastic-plastic fracture criteria are examined with respect to these criteria. It was concluded from this study that *CTOA* (local *COA*) was a viable stable tearing characterization parameter as it met most of the desired criteria. Table 1 shows the comparisons made in this study. Note that $\mathcal{G}$ and $\mathcal{R}$ are generalized energy release rate and toughness, respectively and F_c is the critical crack tip node force in a FE model of a crack growth process.

Table 1: Listing of appraised ductile fracture parameters (starred quantities indicate relative superiority to other parameters in this particular area) [10].

Desirable Features	F_c	$\mathcal{G}_{oc}$	$\mathcal{R}$	$(COA)_c$	$(CTOA)_c$	J_c	$(dJ/da)_c$	R
Constant during stable crack growth with fixed fracture mode	Y*	Y	Y	N	Y	N	N	N
Independent of geometry	N	N	Y	Y	Y	N	N	N
Computer model independent	N	N	Y*	Y*	N	Y*	Y	Y
Possibility of direct measurement	N	N	N	Y*	Y	N	N	N
Computational Efficiency	Y*	Y	N	Y*	Y*	Y*	Y	Y

Brocks and Yuan [11] observed ductile crack growth phenomena in CT, Center Cracked Tension (CCT), and Single Edge Crack Bend (SECB) specimens using FEA analyses for both plane stress, and plane strain cases. Analyses of the plastic zones at the momentary crack tip showed that the *J*-integral could no longer represent the stress state during stable crack extension. The *J* and δ_5 (displacement at initial crack tip [12]) resistance curves were found to depend on the specimen geometry, but the *CTOA* curves were found to be mostly unaffected by geometry during crack extension and by the development of full plasticity. Through these analyses, it was shown that a linear relationship between *J* and *CTOD* existed only for tension specimens during stable crack growth.

Newman et al [13] provided numerically determined *CTOA* results for thin sheet aluminum alloys by observing three different crack configurations, including a blunt notch to ensure the capability for characterization under conditions of extreme plastic yielding. These results were later verified using two different finite element algorithms [14, 15]. The trends observed in these studies showed an initial high value, attributed to tunneling, followed by a relatively constant, critical value for stable tearing. Later, these numerical results were experimentally verified by Dawicke et al [16], who made measurements of *CTOA* in 2024-T3, aluminum, middle cracked tension (MT) and compact tension (CT) specimens.

As noted by Brocks and Yuan [11], and Newman [17], large variations in *CTOA* (or *CTOD*) values for crack extensions less than approximately twice the material thickness may be due to crack tunneling, or to changes in the triaxial constraint as a crack grows into a highly deformed region. To account for 3-D constraint effects in thicker (2 mm) materials, while still using a 2-D analysis for simplicity in calculation, Newman et al and Dawicke et al [14, 18] and others employed a so-called “plane strain core” (PSC) in their FE analyses. This essentially consists of assigning plane strain properties to a strip of elements around the crack plane. The height of this core was empirically determined, based on a match between calculated and experimental crack opening displacements. This was intended to model the constraint effects in the crack tip after a study by Hom

and McMeeking [19] which showed that, although the global material may be in a state of plane stress, material near the crack tip may approach plane strain behavior.

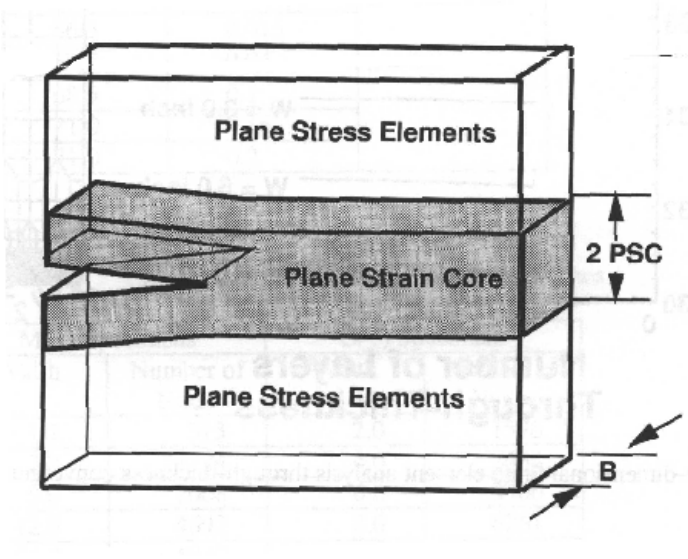

Figure 1.3: Plane Strain Core [14].

Using the 2-D model with a plane strain core, Newman et al [14], Dawicke [18], and others [1, 20] have since shown that a critical *CTOA* may be used in an 'application' phase to correctly model stable crack extension. Most simulations have been run using 2024-T3 aluminum samples of varying thickness with a critical *CTOA* (ψ_c) of between 5 and 6 degrees. Typically, load-crack extension profiles are compared with experimental results for validation of the FE models. Since *CTOA* has been found to be generally independent of specimen geometry, it has significant potential for stable crack tearing characterization. Problems with *CTOA* seem to center around experimental measurement, and finite element mesh sensitivity. This will be discussed in more detail later.

1.2 NONLINEAR-ELASTIC CHARACTERIZATION

1.2.1 J-INTEGRAL AND TEARING MODULUS APPROACH

The use of path independent integrals for the general characterization of energy of fracture has become widespread since the independent contributions of Eshelby [21], Rice [6], and Cherapanov [22]. Specifically, the *J*-integral parameter of Rice [6] has been of practical use in the study of elastic-plastic fracture. It is given in equation (1.6) where w is the strain energy density, T_i is the traction component, u_i is the displacement, and ds is an increment along the counterclockwise integration contour, Γ.

$$J = \int_{\Gamma} \left(w dy - T_i \frac{\partial u_i}{\partial x} ds \right) \tag{1.6}$$

The *J*-integral is interpreted as the energy release rate for an extending crack in an elastic-plastic material, analogous to linear elastic energy release rate, G [23, 24]. It is based on an assumption of non-linear elastic deformation, and has been shown to uniquely characterize crack tip stresses within a so-called *HRR* region by Hutchinson [25], and Rice and Rosengren [26] in materials that exhibit power law hardening behavior. The boundary of this region is defined by a $1/r^{1/n+1}$ singularity in a polar coordinate system, where n is the strain-hardening exponent. These materials may be characterized in the plastic portion of their stress-strain curve with a Ramberg-Osgood type relation as in equation (1.7) where ε is plastic strain, σ is stress, n is the strain hardening exponent, and F is a so-called 'plastic modulus'. The strain-hardening exponent and plastic modulus are obtained by plotting the plastic portion of the stress-strain curve on a log-log plot and performing a linear regression.

$$\varepsilon = \left(\frac{\sigma}{F} \right)^n \tag{1.7}$$

The formation of a crack in a ductile material involves initial blunting, followed by crack initiation. It is at this point that a critical value of the *J*-integral, (J_{IC}), is defined analogous to a 0.2% offset yield stress in a stress-strain curve. Beyond initiation, however, stable crack extension will result in a rising J_R (resistance) curve with a slope indicative of the relative stability of this crack extension [5]. The slope of the J_R curve is typically quantified as part of a non-dimensionalized tearing modulus (equation (1.8)), where σ_0 is the flow stress, and *da* is the incremental crack extension.

$$T_R = \frac{E}{\sigma_0^2}\frac{dJ_R}{da} \tag{1.8}$$

In direct correlation with the *R*-curve concept of linear elastic fracture, crack extension becomes unstable when the driving force curve becomes tangent with the J_R curve. Thus, an applied tearing modulus (1.9) is defined for use here as well. For $T_{app} \leq T_R$, crack extension is stable, and for $T_{app} \geq T_R$, it is unstable.

$$T_{app} = \frac{E}{\sigma_0^2}\left(\frac{dJ}{da}\right)_{\Delta_T} \tag{1.9}$$

Unfortunately, since the *J*-integral is based on the deformation theory of plasticity, it will lose its validity in any instance of unloading. In the event of the development of a large plastic zone in front of the crack tip or for an extending crack, unloading is inevitable. In addition, as a crack extends through a material, a plastic wake zone will form behind the growing crack, also contributing to non-proportional loading. The *J*-integral will remain relatively valid only in instances of *J*-controlled fracture, which in essence means that the flaw size remains very small with respect to in-plane specimen dimensions. In this case, nearly proportional plastic deformation takes place everywhere except within a very small region surrounding the crack tip. Under these circumstances, there is negligible difference between the deformation theory of plasticity and the incremental theory, and an assumption of non-linear elasticity is justified [27].

1.2.2 MULTIPLE PARAMETER APPROACHES (J-Q THEORY)

In an attempt to provide more detail within a *J*-dominant region, researchers such as Li and Wang [28] have derived higher order terms in the *HRR* series to account for asymptotic stress, strain and deformation fields for power law hardening materials. Based on this, Li and Wang [28] developed a two-parameter fracture criterion based on J_{IC} and the state of triaxial stress ahead of the crack tip. As a result, O'Dowd and Shih [29, 30] formed the *J-Q* theory, with the triaxial state of stress represented by a parameter, *Q*. Single parameter fracture mechanics assumes that the state of stress is characterized by the leading term of the *HRR* infinite power series. Under an assumption of small strain theory, the stresses within the plastic zone may be characterized by this series, with the *HRR* singularity as the leading term and a so-called difference field representing higher order terms [5]. The summation of higher order terms, which represents the difference between a single parameter stress field and the actual stress field, is the parameter, *Q*, in *J-Q* theory.

It is noted by Anderson [5] that, while the *J-Q* approach allows characterization of the crack tip constraint, it does not account for any relationship between this constraint and the fracture toughness. Also, in the presence of large scale yielding, constraint parameters lose their physical meaning. Therefore, *J-Q* theory merely gives a more detailed account of near tip stresses in a cracked body than a single parameter characterization. In addition, as noted by Kobayashi [31], *J-Q* theory was formed with a plane strain state in mind. Since the out of plane constraint essentially disappears in thin materials (plane stress), the *J-Q* theory may not be applicable for evaluation of thin-sheet problems.

A more recent variant of the *J-Q* theory, is the *J-*A_2 theory [32] where A_2 is the first of the higher order terms in the Taylor series expansion of the *HRR* field. This method has been used to interpret cleavage fracture events and, unlike the *Q* parameter in *J-Q* theory, the A_2 parameter is an accounting of the actual relationship between crack tip constraint, and

fracture toughness. More importantly, J-A_2 theory may be utilized for fracture events controlled by either stress or strain, or a combination of stress and strain. In contrast to the J-Q theory, the J-A_2 method does not rely on correlation of the elastic plastic stress fields at the crack tip.

Dadkhah et al [33, 34] have calculated experimental values of the J-integral from measured surface displacements and found that, with the exception of small stable crack growth of 1-3 mm, the results agreed well with the known solutions. These experimentally obtained J-integral values were then used in a reverse manner to compute the *HRR* displacements in the vicinity of the crack tip. It was found that the computed tangential displacements compared well, but the radial displacements (parallel to crack) were found to be substantially different. This behavior was also observed in attempts to characterize the displacements with the addition of higher order terms such as (Q). Results of these studies were later verified in a different study by Sciammarella and Combel [35], who compared the experimental and numerical displacements in the vicinity of the crack tip. The invalidity of the *HRR* displacements in these studies suggests that the J-integral does not fully characterize the strength of the *HRR* singular field.

1.2.3 THE I-INTEGRAL

The limitations of the J-integral approach have led to investigations of other line integrals. Moran and Shih [36] considered the I-integral, which applies to steady state crack propagation in a true elastic-plastic material, in a study dedicated to the exploration of generalized line integral interpretations of fracture. The I-integral is given in the same form as the J-integral with two important distinctions. First, the strain energy density function, W, is now interpreted as total stress work density, and therefore depends on the history of deformation and second, the I-integral is only path independent for steady state crack propagation. The singularity of the stress work density is weaker than that of the strain energy density and the I-integral will be zero on a contour very close to the crack

tip, unlike the *J*-integral which is non-zero [37]. Since work must be expended in the fracture process zone as well as the surrounding plastic zone during ductile fracture, the fact that the *I*-integral reduces to zero near the crack tip presents a potential problem.

1.3 CREEP FRACTURE

1.3.1 GENERAL TIME DEPENDENT CONSIDERATIONS

Metallic structures under static load and subjected to temperatures close to the melting point of the material, will exhibit time dependent deformation. Typically, studies have concentrated on uniform structures that develop microscopic cracks during high temperature, long duration loading. It is of perhaps equal importance, however, to consider the stable crack propagation of any existing macroscopic flaw. To account for fracture behavior under creep cracking conditions, a variable of time must be introduced into the fracture analysis.

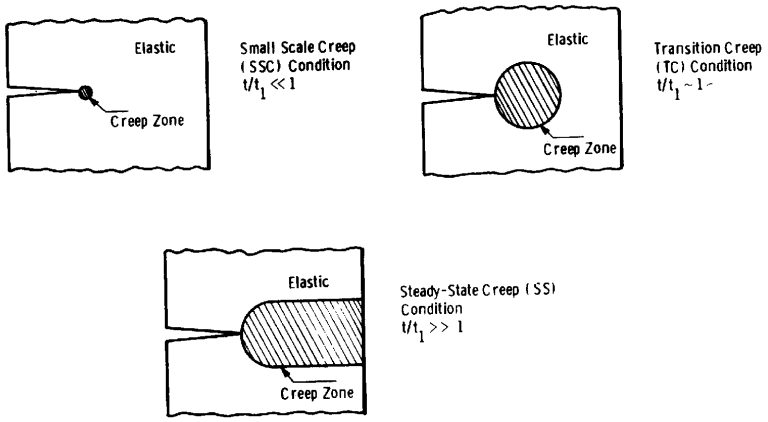

Figure 1.4: Regimes of Creep Behavior [50].

As in any fracture analysis, the characterizing parameter must have the ability to portray crack tip behavior. Toward this end, there were early studies such as that of Siverns and Price [38] which attempted to correlate the linear elastic stress intensity factor, *K*, to

creep crack growth rates. A detectable relationship was observed in this study between K and creep crack growth, but the data exhibited a very high scatter band of approximately 20-30 $MPa\sqrt{m}$. Since creep is primarily an elastic-plastic phenomenon, this approach had limited success but served to prove that the capability for characterization of creep fracture does exist [39]. Based on this study, Siverns and Price [38] concluded that a reasonable description of the creep crack growth data could be given as;

$$da/dt = AK^n \tag{1.10}$$

Where da/dt is the crack growth rate, A and n are empirical constants obtained from regressions of data plotted on a log-log plot, and K is the sharp crack stress intensity factor. This formula provides a rough approximation of the correlation between creep crack growth rate and linear elastic stress intensity factor. It should be stressed that creep crack growth is a primarily plastic phenomenon and, as such, will require a non-linear characterization parameter to provide the required detail.

1.3.2 THE C INTEGRAL APPROACH TO CREEP FRACTURE*

Landes and Begley [39], used a time dependent form of the J-integral, denoted the C^* integral to study high temperature creep crack growth in a Discaloy superalloy. In two-dimensional form, the C^* integral is given as Eq. (1.11);

$$\begin{aligned} C^* &= \int_\Gamma \left(W^* dy - T_i \left(\frac{\partial \dot{u}_i}{\partial x} \right) ds \right) \\ W^* &= \int_0^{\dot{\varepsilon}_{mn}} \sigma_{ij} d\dot{\varepsilon}_{ij} \end{aligned} \tag{1.11}$$

Where W^* is the strain energy rate density, $\dot{u}_i$ is the displacement rate, $\dot{\varepsilon}_{ij}$ is the strain rate, and the other symbols are defined similar to the J-integral. Prior to this study, it had been shown by Goldman and Hutchinson [40], that the C^* integral could be used as a single parameter to characterize the state of the near-tip stress and strain rate fields,

analogous to the *HRR* characterization of near tip stresses and strains by the *J*-integral. In this case, the near tip stress and strain rates are given as Eq. (1.12):

$$\sigma_{ij} = \sigma_0\left[C^*/\alpha\sigma_0\varepsilon_0 I_n\right]^{\frac{1}{n+1}} r^{\left(-\frac{1}{n+1}\right)}\tilde{\sigma}_{ij}(\theta)$$
$$\dot{\varepsilon}_{ij} = \alpha\varepsilon_0\left[C^*/\alpha\sigma_0\varepsilon_0 I_n\right]^{\frac{n}{n+1}} r^{\left(-\frac{n}{n+1}\right)}\tilde{\dot{\varepsilon}}_{ij}(\theta) \tag{1.12}$$

Where ε_0, σ_0, α, and n (creep exponent) are constants defined in the creep law given as Eq. (1.13);

$$\frac{\dot{\varepsilon}}{\varepsilon_0} = \alpha\left(\frac{\sigma}{\sigma_0}\right)^n \tag{1.13}$$

and I_n is a numerical constant which is a function of n and the mode of crack opening. $\tilde{\sigma}_{ij}(\theta)$ and $\tilde{\dot{\varepsilon}}_{ij}(\theta)$ are dimensionless functions which define the stress and strain rate distribution [40]. These stress and strain rate definitions are based on a principle known as Hoff's analogy [41] which states that a nonlinear elastic body that obeys a material law $\varepsilon = f(\sigma)$, and a nonlinear viscous body characterized by $\dot{\varepsilon} = f(\sigma)$, develop the same stress field when subjected to the same loads. It is noted that the *C** integral may only be applied under an assumption that the material being studied follows a steady state creep law as in Eq. (1.14), which is a multiaxial representation of equation Eq. (1.13) [39]. The *C** integral may therefore only be applied to a specific range of crack growth, namely that during which the material is governed by Eq. (1.14) and under steady state conditions (time independent stresses)

$$\frac{\dot{\varepsilon}_{ij}}{\varepsilon_0} = \frac{3}{2}\alpha\left[\frac{\sigma_e}{\sigma_0}\right]^{n-1}\frac{s_{ij}}{\sigma_0} \tag{1.14}$$

where σ_e is the effective stress, and s_{ij} is the stress deviator tensor. It is invalid for primary (Small Scale –SSC) and tertiary creep.

It should be noted that other researchers such as Ohji et al [42], and Nikbin et al [43] were also responsible for the development of this *C** integral. Their work was concurrent with that of Landes and Begley [39], but it seems the Landes and Begley study is sufficiently comprehensive for this review.

For experimental purposes, the *C** integral was calculated by Landes and Begley [39], using a somewhat complex, six step procedure. The first step involves plotting load and crack length versus time, and load versus crack length for several applied displacement rates. The second step was to plot load versus displacement rate for differing crack lengths, which provided a measure of energy rate, or power input. The final four steps essentially involve the derivation of *C** from these first plots. The *C** integral per unit thickness will be the slope of the power input versus crack length curve. This is somewhat analogous to calculating the *J*-integral graphically as in the ASTM standard test method for J-integral testing [44]. When used in this fashion, the C* integral may be expressed as;

$$C^* = -\left(\frac{\partial \dot{U}}{\partial a}\right)_{\dot{\Delta}} \tag{1.15}$$

$$\dot{U} = \int_0^{\dot{\Delta}} P d\dot{\Delta} \tag{1.16}$$

Landes and Begeley's preliminary study of the feasibility of using the *C** integral to correlate creep crack growth rates proved to be moderately successful. The *C** integral was shown to apply in this sense, at least to the Discaloy used in this study. This provided the impetus for future studies in this area. Indeed, other researchers such as Riedel [45] have since shown similar correlation by employing the *C** integral as a creep crack growth rate correlation parameter within the steady state regime. The lifetimes of cracked components are calculated by developing relationships between crack growth rates and the *C** integral. This relationship is given by Riedel [46], and Hui et al [47] for large crack growth increments as;

$$\frac{da}{dt} = \frac{\pi\left[\tilde{\sigma}_e(0)\right]^n A^{1/(n+1)}}{\sin\left[\pi n/(n+1)\right]\varepsilon_f}\left(\frac{C^*}{I_n}\right)^{n/(n+1)}\left[(\Delta a)^{1/(n+1)} - \beta x_c^{\,1/(n+1)}\right] \qquad (1.17)$$

where *da/dt* is the crack growth rate, x_c is a distance ahead of the crack tip of the order of the material's microstructural scale, β is a numerical factor with values of β = 0.85, 0.90, 0.95, and 1 for values of n = 4, 5, 7.5, and ∞, respectively, A is a temperature dependent factor from Norton's creep law, ε_f is the critical strain for local failure, and the rest of the parameters are as defined in the *HRR* solutions. The lifetime of a cracked component may be obtained by performing a time integration of the creep crack growth rate. It is noted [45] that the creep crack growth rate is a function of crack extension, Δa, which leads to a steep increase of the crack growth rate in the early stages of crack growth. The application of this formulation, and observations of growth rate behavior have been experimentally observed by researchers such as Riedel and Wagner [48], and Detampel [49] in 1Cr-1/2Mo and 2 ¼ Cr-1Mo steels, respectively. The characterization of creep crack growth rates within the steady state realm is well documented and does not require further extensive analysis.

1.3.3 THE C_t, AND C(t) INTEGRALS

Naturally, research on the *C** integral extended into the realm of non-steady state, to accommodation for all instances of creep crack growth. Non-steady state creep (fig 1.4) is generally defined as small scale (t~0), transitional (between small scale and steady state), and tertiary creep. Studies such as those by Saxena [50], Ehlers and Riedel [51], and Ainsworth et al [52] first attempted to address this issue. In [50], a parameter designated C_t was introduced to characterize creep crack growth over a wide range of creep crack growth behavior, including small-scale creep and transient creep. C_t is shown to be independent of geometry, and is demonstrated over a wide range of crack growth rates. Under steady-state conditions $(t \to \infty)$, C_t reduces to the path independent integral, *C**. It is interpreted as the instantaneous value of the difference between energy

rates supplied to two creeping, cracked bodies with incrementally differing crack lengths (Eq. 1.18);

$$C_t = -\frac{1}{B}\frac{\partial U_t^*}{\partial a} \tag{1.18}$$

where B is specimen thickness, and ΔU_t^* represents the difference in energy rates supplied to the two creeping bodies. Alternatively, C_t may be defined as;

$$C_t = \frac{P\dot{V}_c}{BW}\frac{F'}{F} \tag{1.19}$$

where

$$\dot{V}_c = \frac{4\alpha\left(1-\nu^2\right)}{E\left(n-1\right)}\left(\frac{P}{B}\right)^3 \frac{F^4}{W^2} t^{3-n/n-1}\left(EA\right)^{2/(n-1)} \tag{1.20}$$

and

$$\alpha = \frac{1}{2\pi}\left(\frac{\left(n+1\right)^2}{2n\alpha_n^{n+1}}\right)^{2/(n-1)} \tag{1.21}$$
$$F = \left(K/P\right)BW^{1/2} \quad , \quad \left(F' = dF/d(a/W)\right)$$

K is the applied stress intensity factor, F is a K calibration factor, A and n are the creep factor and creep exponent, respectively, and $\dot{V}_c$ is the applied load-line deflection rate. Also, P is applied load, W is specimen width, B is thickness, and E is Young's Modulus. This parameter (C_t) has since been applied in studies of power law materials by several other researchers [54-55].

Linkens et al [54] investigated the applicability of procedures for calculating C_t within the transition regime where its definition is questionable, by comparing finite element models with experimental results for simple geometries. Results were found to be

conservative when using the *R5* method [52] where a crack tip parameter *C(t)* is defined using far field estimates of *J* as;

$$C(t) \cong C_{R5}(t) = \frac{J^{n+1}}{(n+1)\int_0^t J^n dt} \tag{1.22}$$

where *n* is the creep exponent, or using the method given by Saxena [50]. Results were generally non-conservative with the use of the Ehlers and Riedel method [51], where a crack tip parameter, $C(t) = C^*(1 + t_1/t)$, is used as an estimate of C_t within the transition region. Here, the ratio t_1/t is representative of the ratio of transition time to test time.

The parameter *C(t)* of Ehlers and Riedel [51], Ainsworth and Budden [52], and Riedel and Rice [55], is interpreted as the amplitude of the crack tip stress fields under elastic-plastic deformation conditions. It is simply an estimate of the C_t parameter of Saxena [50]. Busso et al [56] recently investigated the use of *C(t)* in a study where the calculated amplitudes (*C(t)*) of singular crack tip fields in the non-steady state regime of power law creeping materials and found that opening stresses had a slightly higher order of singularity than *HRR* type fields characterized by the $r^{(-1/(n+1))}$ singularity. Also, Dogan et al [53] compared the use of *C**, *C(t)*, C_t, and *J*-integral as characterizing parameters in relatively brittle, *Ti-6242* alloys and found that crack growth rate, *da/dt*, only correlates with *C(t)* and C_t when the creep component $(\dot{V}_c)$ of deflection rate is dominant. Thus, the use of C_t for characterizing small scale, and steady state creep, and *C(t)* for transition creep may be in question.

Saxena [50], notes that, although it expands the applicability of the *C** integral to primary and small scale creep (SSC) conditions, there are several limitations to C_t. First, its use is restricted to cavitating materials in which creep damage is necessary in the crack tip region for crack growth to occur. Under these conditions, even in the event of primarily elastic behavior, *K* or *J* will not be able to characterize crack growth (see Eqs. (1.19)-

(1.21)) and there will be no unique relation between K and da/dt. There are no well-established correlations between void growth phenomena, and creep fracture parameters. As noted in [8], an interpolation between the small scale (K-dominated) and steady state (C_t, *or C(t)*) region must be used, with the exception of the transition time where no definition is available. In addition, the damage (cavitation) must be very localized. That is, the process zone must be very small in comparison to the region over which the *HRR* type stress and strain rate relations are defined. As noted by Riedel [45], the condition for valid C* testing is; $\Delta a \leq$ (5 to 15)% of a or $W - a$. Further, since C_t is dependent on the extent of creep, it is also time dependent, even at a fixed crack length. For a growing crack, the reference from which t is measured is lost, meaning it is difficult to measure the value of C_t without actually calculating the creep component of deflection rate, $\dot{V}_c$. Thus, it is necessary to have both numerical and experimental results available to make any approximation. Finally, these parameters are valid based on the assumption that a path independent J-integral (non-linear elasticity) could be used to characterize crack tip stress and strains in the event of a stationary crack. As discussed previously, this is not a valid assumption. There is a question concerning the relationship between C_t and the *HRR* field in the small scale, and transition regions [50].

1.4 THE T^*_ε INTEGRAL

1.4.1 ORIGINS OF T^*_ε, ΔT_C

In 1982, Atluri [57] introduced ΔT_c, a general, time dependent path integral that may be used to characterize strain energy in the presence of non-steady state, creep crack extension. This approach was an attempt to overcome the inaccuracies involved in the use of the C_t integral. Another detailed discussion of ΔT_c in the context of creep crack extension came later in the same year from Stonesifer and Atluri [58] in which a numerical model was developed for use with a compact tension (CT) sample. A representation of ΔT_c, which is independent of contour size, is given as;

$$\Delta T_c = \int_{\Gamma_{234}} n_1 \Delta W - n_j \left(\sigma_{ij} - \Delta\sigma_{ij}\right) \frac{\partial \Delta u_i}{\partial x_1} dS - \int_{V_t} \frac{\partial \sigma_{ij}}{\partial x_1} \Delta\varepsilon_{ij} dV \tag{1.23}$$

where W is the stress work density,

$$\Delta W = \left(\sigma_{ij} + \frac{1}{2} \Delta\sigma_{ij} \Delta\varepsilon_{ij} \right) \tag{1.24}$$

and σ_{ij} is understood to be the stress at the beginning of the current time step, Γ_{234} is a

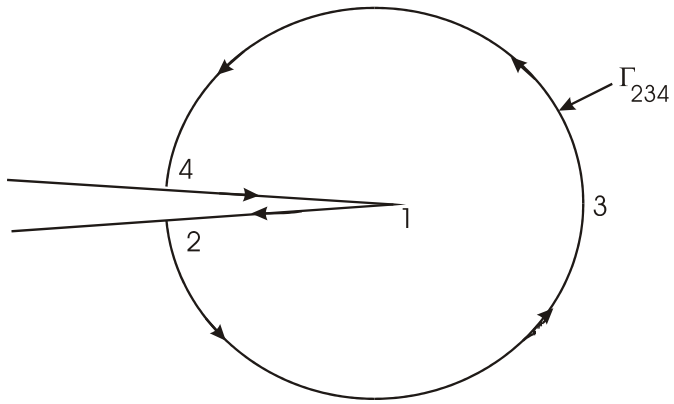

Figure 1.5: Contour of integration for ΔT_c [57].

counterclockwise contour (Figure 1.5) beginning at one crack face and extending to the other, n are unit normals, and V_t is the volume enclosed by the contour. This parameter was compared to the widely accepted, path dependent C^* integral which is typically applied in an instance of steady state creep crack extension and was intended to be an all encompassing creep characterizing parameter including, the linear elastic approach and the C^* integral approach. Figure (1.6) is a depiction of the path dependence, and the relative path independence of the C^* and ΔT_c integrals respectively.

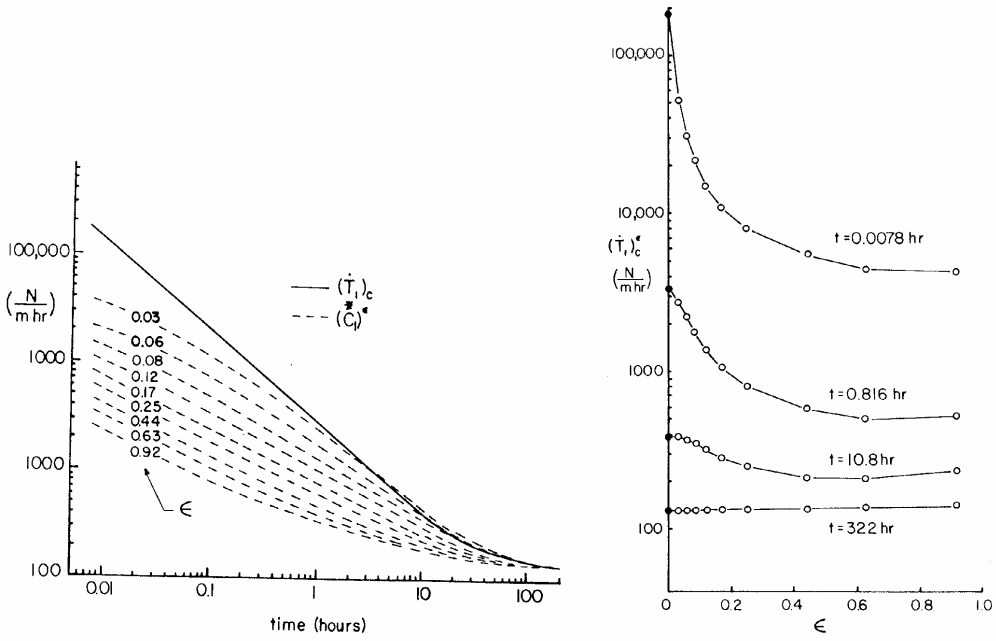

Figure 1.6: Relative path dependence or independence of ΔT_c and C integrals, ε is contour size [58].*

The concept of ΔT_c was slightly modified by Atluri et al [59] to be an incremental form of the *J*-integral which, when integrated along the load path under assumptions of non-linear elasticity, will be equal to *J*. This incremental parameter, denoted ΔT^*_p in this work, was defined as a path-independent integral which could characterize the crack tip fields under a flow theory of plasticity. It was also valid for arbitrary loading and unloading conditions, but under monotonic loading, was equal to the *J*-integral as defined by Rice [6]. The modified form, ΔT^*_p from the initial discussion in [59] is given in equation (1.25) as the incremental form of a measure of the crack-tip stress/strain field. The total value is given as the sum of the incremental steps $(\Sigma \Delta T^*_p)$.

$$\Delta T_p^* = \int_{\Gamma_\varepsilon} \left[\Delta W n_1 - \left(t_i + \Delta t_i\right) \frac{\partial \Delta u_i}{\partial x_1} - \Delta t_i \frac{\partial u_i}{\partial x_1} \right] dS \tag{1.25}$$

1.4.2 THE LOCAL T$_\varepsilon$ INTEGRAL*

Brust et al [60], and Atluri [61] eliminate the need for summation by defining a local value, T^*_ε, defined on a small contour, Γ_ε surrounding the crack tip as;

$$T^*_\varepsilon = \int_{\Gamma_\varepsilon} \left(W n_1 - t_i \frac{\partial u_i}{\partial x_1} \right) d\Gamma \tag{1.26}$$

$$W = \int_0^{\varepsilon_{ij}} \sigma_{ij} d\varepsilon_{ij} \tag{1.27}$$

Here, W is defined as the stress work density, rather than its interpretation as the strain energy density in Rice's J-integral. In this total form, T^*_ε is calculated along a so-called

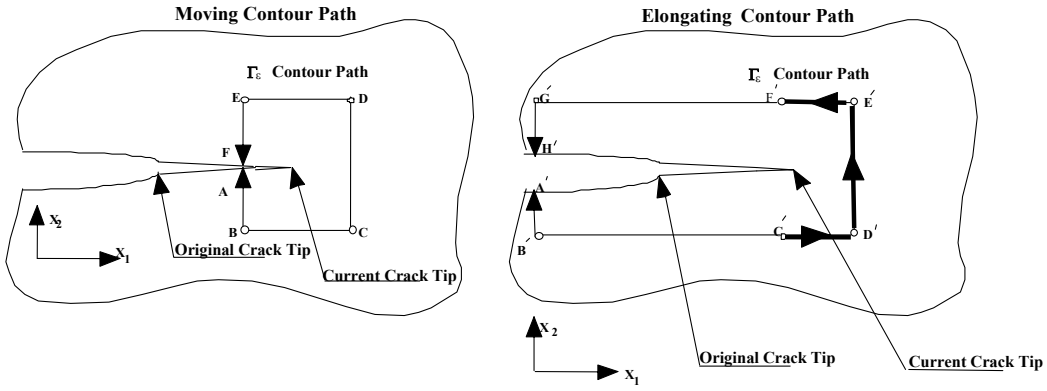

Figure 1.7: Moving and elongating integration contours.

"elongating contour" (Figure 1.7) which grows as the crack extends. Pyo [62] showed, through a series of FEM analyses, that T^*_ε could be used in this form to predict the load carrying capacity of cracked structures if the stresses and strains were obtained using the incremental theory of plasticity. From these definitions, it is seen that T^*_ε is explicitly dependent on strain history, which is an essential characteristic for elastic-plastic crack growth studies.

The divergence theorem may be applied to obtain a representation of Eq. (1.26) as a summation of a far-field, contour integral plus a finite domain integral as in Eq. (1.28) [65]. Here the volume formulation has been generalized to an area domain for 2-D since, in this case, *dz=1.0* such that *dV=dxdy* (area per unit thickness) and out of plane strain gradients are zero. It is noted here that the numeral 1 appearing in the subscript is indicative of the fact that T^*_{ε} is a vector quantity and in this case we are concerned with only the x_1 component.

$$T^*_{1\varepsilon} = \int_{\Gamma}\left(Wn_1 - t_i \frac{\partial u_i}{\partial x_1}\right)d\Gamma - \int_{A-A_\varepsilon}\left(\frac{\partial W}{\partial x_1} - t_{ij}\frac{\partial \varepsilon_{ij}}{\partial x_1}\right)d(A-A_\varepsilon) \tag{1.28}$$

In this equation, it is noted that the first term on the right hand side is equal to Rice's *J*-integral, and that T^*_{ε} differs by the second term. In the limit as the area tends to zero, T^*_{ε} becomes equal to *J* because the second term disappears. In a series of FE analyses, Brust et al [64] observed that the second term became larger as crack growth proceeded. That is, as *J* continued to increase, T^*_{ε} reached a plateau as seen in Figure (1.8).

To overcome inherent large stress and strain gradients in the vicinity of the crack tip, Nikishkov and Atluri [63] introduced the "equivalent domain integral" method for calculating $T^*_{1\varepsilon}$ from remote values as;

$$T^*_{1\varepsilon} = \int_{\Gamma_\varepsilon}\left(Wn_1 - \sigma_{ij}\frac{\partial u_i}{\partial x_1}n_j\right)Sd\Gamma \tag{1.29}$$

Or, by application of the divergence theorem and a 2-D generalization;

$$T^*_{1\varepsilon} = -\int_{A-A_\varepsilon}\left(\frac{\partial}{\partial x_1}(WS) - \frac{\partial}{\partial x_j}\left(\sigma_{ij}\frac{\partial u_i}{\partial x_1}S\right)\right)d\left(A-A_\varepsilon\right) \tag{1.30}$$

where S is an arbitrary, smooth function equal to 1 on Γ, and 0 on Γ_ε, and A-A_ε is the area per unit thickness encompassed by the domain of integration. The S-function used in this capacity is an analog to a similar function utilized by Li et al [64], which may be interpreted as enforcing a unit displacement in the X_1 direction on the nodes along the inner contour, Γ while holding the nodes along the outer contour, Γ_ε, stationary. Hence, it is also analogous to a Virtual Crack Extension technique by virtue of its similarity to the function employed in [64]. Equation (1.29) may be further decomposed [63] into two parts, by application of the chain rule of calculus;

$$\begin{aligned} T^*(S) &= -\int_{A-A_\varepsilon} \left\{ W \frac{\partial S}{\partial x_1} - \sigma_{ij} \frac{\partial u_i}{\partial x_1} \frac{S}{\partial x_j} \right\} dA \\ T^*(W) &= \int_{A-A_\varepsilon} \left\{ \frac{\partial W}{\partial x_1} - \sigma_{ij} \frac{\partial \varepsilon_{ij}}{\partial x_1} \right\} S dA \end{aligned} \tag{1.31}$$

For the case of a linearly elastic, or nonlinearly elastic, homogeneous material, it is noted that $\frac{\partial W}{\partial x_1} \equiv \sigma_{ij} \frac{\partial \varepsilon_{ij}}{\partial x_1}$ so the second term, $T^*(W)$ is equal to zero and the summation of the two is equivalent to the J-integral.

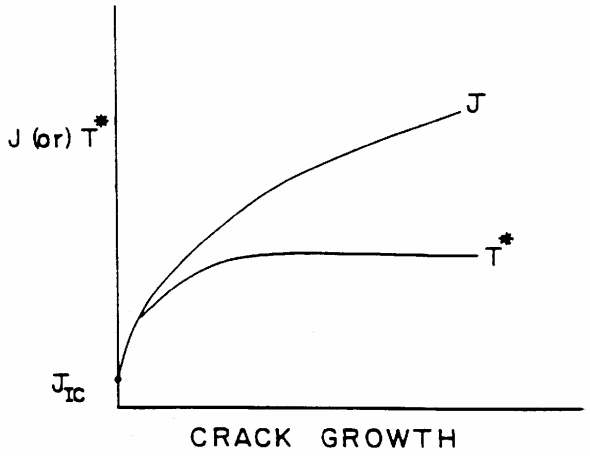

Figure 1.8: Divergence of J and T integrals with crack extension [65].*

Like the *J*-integral, the T^*_{ε} integral becomes path dependent in the presence of large plastic yielding, or unloading. Thus, to be used as a valid fracture criterion, T^*_{ε} must be evaluated along a fixed contour very close to the crack tip. The size of this contour has been found, in general, to be approximately equal to plate thickness for plane stress by Narshimhan and Rosakis [66] who observed the level of constraint in front of the crack tip.

Okada et al [67] investigated the difference between the "moving" contour, which moves along with the crack tip, and the "elongating" contour, which grows with the crack (figure 1.7). Using simple energy balances, Okada showed that these two contour types measured different physical quantities. The moving contour was shown to represent the energy release at the crack tip, while the elongating contour is interpreted as the energy dissipation near the crack tip plus the energy release rate at the tip per unit crack extension. The elongating contour accounts for unloading behind the crack tip, as well as deformation close to, and in front of it. Values of T^*_{ε} calculated using the moving contour dropped to zero soon after crack initiation as they represent the energy release

rate at the crack tip. Thus, it was concluded that the elongating contour should be used in calculation of T^*_ε because it represents energy dissipation in the extending, near-crack integral path, per unit crack extension.

There seem to be two major reasons for the success of the T^*_ε integral for stable crack extension as opposed to the *J*-integral. First, the T^*_ε integral is based on the incremental (flow) theory of plasticity instead of the deformation theory. This allows it to account for all loading history events, the most important of which is load/unload history. Second, it is calculated along a contour, which extends along with the growing crack. This allows for accounting of all processes occurring within the fracture process zone.

1.4.3 FINITE ELEMENT AND EXPERIMENTAL CALCULATION OF T^*_ε

The majority of the early work involving T^*_ε was performed using numerical analysis techniques [60, 61, 65]. T^*_ε resistance curves are typically calculated numerically, using the EDI method of Nikishkov and Atluri [63] in what is termed the "generation phase" by Kanninen and Popelar [8]. The resistance curve is then used to control the crack growth in a FE model by allowing the specimen to reach the critical value of T^*_ε and then modeling an increment of crack growth. This fracture parameter controlled crack growth is known as the "application phase" [8] of the analysis. The numerical results are then compared to actual load versus crack growth data.

In 1997, Wang et al [68] used a method termed as the Elastic-Plastic Finite Element Alternating Method (EPFEAM) by Nikishkov and Atluri [69], to predict elastic-plastic fracture in aircraft structures. This is essentially a superposition scheme, which iterates between analytical solutions for a cracked body, and an uncracked body. It involves solving for crack closure tractions under a linear elastic assumption, reversing the tractions, solving for the residual stress, and iterating until the process converges. This method was shown to accurately predict fracture behavior in aircraft structures.

Following the early numerical work, recent attempts have been made to develop procedures for calculating T^*_ε directly from experimental displacement data [67, 70]. Most of this work was aimed at overcoming the difficulties inherent in the use of incremental (flow) theory of plasticity with experimental data. Okada et al [70] simplified the integration procedure by neglecting the portions of the contour behind the crack tip. With reference to Figure (1.7), this means that the portions of the contour path labeled F'-G', and C'-B' are neglected by assuming that the stresses acting on a constant plane were nearly zero close to the traction-free crack and by realizing that along these portions, n_1 is zero. The portions labeled G'-H', and B'-A' are also considered to be small in terms of the work density as a result of their being far behind the original crack tip. This led to a calculation method involving a "cut-off" procedure involving the truncation of the integral contour from an empirically determined distance behind the crack tip. Since it is difficult to obtain the incremental history in an experiment, the deformation theory of plasticity was used to calculate stresses from experimentally determined strains. This is allowable as long as the cut-off integration contour is employed. In comparison with T^*_ε values calculated (FEM) using the incremental theory of plasticity, the T^*_ε values calculated using the cut-off integration contour method with deformation plasticity were shown to agree well.

Using the method developed by Okada et al [70], Omori et al [71, 72] have successfully measured T^*_ε experimentally in A606 HSLA steel [71], and 2024-T3 aluminum [72]. Using single edge notched (SEN) type specimens of 1 mm thickness, T^*_ε integral values were obtained numerically and experimentally for the A606 HSLA steel in [71]. It was found that T^*_ε values calculated from FEM and experimental displacements were in good agreement, and that values were contour dependent but tended to converge to a steady state value at a distance approximated by the thickness of the specimen. In [72], aluminum (SEN), compact tension (CT), and center notched (CN) type specimens were analyzed in a similar manner. Again, these preliminary test results showed good agreement between numerical and experimental values. It should be noted that, while

these studies showed promising results, the amount of experimental data collected was small.

Walker and MacKenzie [73] have investigated the use of the T^*_ε integral in creep relaxation cases. This study did not involve any crack extension, but served to illustrate the utility of using the T^*_ε integral for characterization in creep studies. Since the crack did not grow in this case, the contour of integration remained stationary. ΔT^* contributions were summed throughout the loading history to give the T^*_ε integral with an incremental plasticity assumption. The T^*_ε integral was shown to be calculable as long as the creep dominated zone was contained within the inner contour of integration. When the creep zone grew beyond the contour, the elastic and plastic strains required decoupling in order to allow accurate calculation.

Brust [74] performed an analysis of time dependent deformation under variable load conditions in 316 stainless steel. This study consisted of both numerical and experimental analyses. Here a variable load history was input to a servohydraulic load frame and load line displacement versus time was recorded. The finite element model was forced to follow the observed crack length versus time behavior. Based on this study, it was concluded that the T^*_ε integral approach is potentially useful in studies involving variable load histories.

1.5 RECENT WORK, TWO DIMENSIONAL T*

Over the past ten years, much work has been done to characterize the T^*_ε integral experimentally, for two-dimensional cases. This includes characterization in thin, plane stress samples [71, 72, 92, 100], somewhat thick (3.1 mm), plane stress/plane strain CT samples [91, 93], and plane stress, wide panel multiple site damage (MSD) samples [92]. The studies mentioned here incorporated experimental characterization of the T^*_ε integral with numerical evaluation. Comparisons between numerical results and experimental

values calculated using Okada's truncated contour agreed very well in all cases. In [92], a full 'generation' and 'application' phase analysis was carried out for thin (0.8 mm) 2024-T3 aluminum MSD wide panels. T^*_ε resistance curves (Figure 1.9) were generated and used to drive an FE model in its application phase. Load versus crack extension was compared between the FE and experimental results to validate the T^*_ε master curve and FE model. Figure 1.10 shows the load versus crack extension comparison from this study. Figures 1.11 and 1.12 show experimental and numerical comparisons for monotonic and low-cycle fatigue, 3.1 mm thick, 2024-T3 aluminum CT specimens from [91] and [93] respectively. These curves demonstrate the viability of the T^*_ε integral as a stable tearing characterizing parameter by demonstrating the achievement of a 'steady-state' value upon reaching a crack extension approximated by the thickness of the specimen.

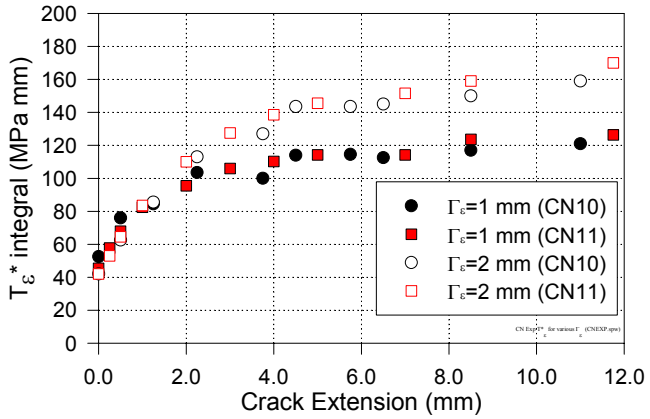

Figure 1.9: T^*_ε for center notched (CN), 2024-T3 aluminum alloy specimens [92].

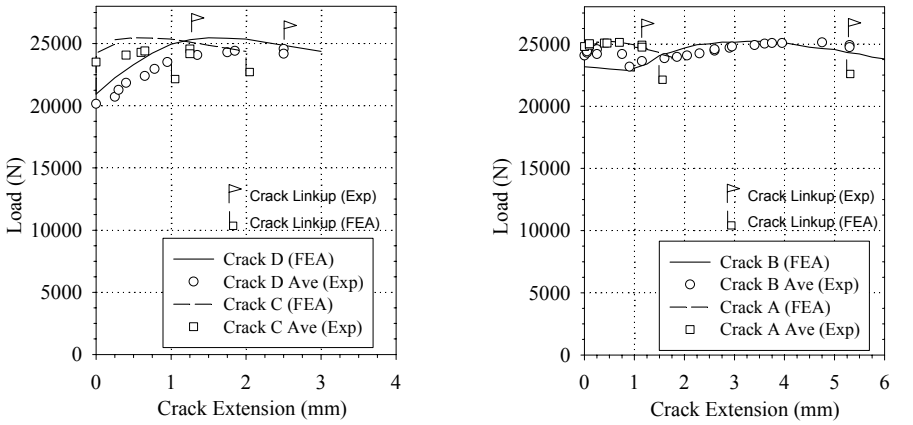

(a) Reaction load of first crack linkup

(b) Reaction load of second crack linkup

Figure 1.10: Crack growth simulation with T^*_ε criterion for MSD specimens [92].

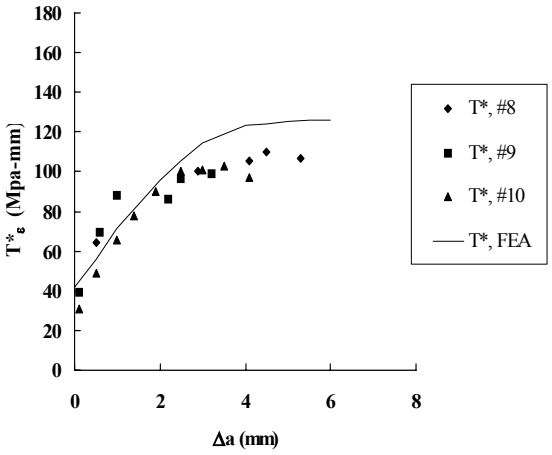

Figure 1.11: T^*_ε curves for 2024-T3 aluminum CT specimens under monotonic load [91].

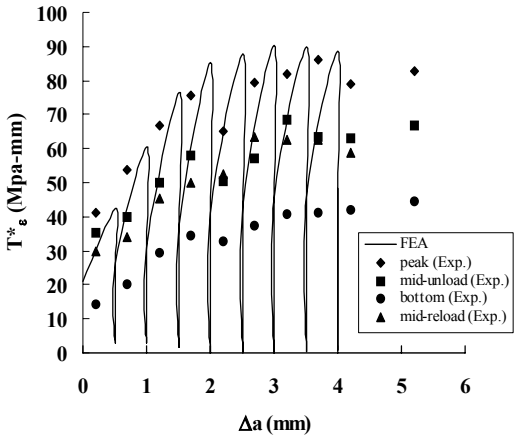

Figure 1.12: T^*_ε curves for 2024-T3 aluminum CT specimens under low cycle fatigue [93].

1.6 THREE DIMENSIONAL CONSIDERATIONS

1.6.1 3-D, J-INTEGRAL

A majority of practical fracture mechanics applications involve complex, three-dimensional geometries. As a result, analysis of fracture parameters along crack fronts of essentially three-dimensional flaws has been considered for many years. Authors such as Newman and Raju [75], and Shah and Kobayashi [76], among others, offered linear elastic solutions based on finite element analyses for semi-elliptical flaws in finite, three-dimensional bodies undergoing tensile and bending loading. Linear elastic, 3-D solutions are well documented in several texts such as references [5] and [8]. These analyses were intended to provide linear elastic solutions for flaws such as those surrounding bolts or rivets, or for part through cracks in pressure vessels.

More recently, analysis of fracture toughness characterization in three-dimensional, finite bodies has been extended to the elastic-plastic regime. Rice's *J*-integral provides a quantification of material toughness in 2-D, but application in fully 3-D situations is often abandoned in favor of characterization by *CTOD*. A possible reason for this, aside from the obvious complexities involved in experimentally obtaining a value of the 3-D surface integral, is uncertainty over the proper definition of a 3-D *J*-integral for point-wise characterization along a crack front. There are three numerical approaches that have been developed to compute the energy release rate along a crack front. Two involve methods of virtual crack extension [85], both directly and indirectly by utilizing the ability to virtually extend the crack in an arbitrary, point-wise fashion along the crack front and measuring the resulting change in energy. The distinction between direct and indirect methods involves the proximity of these displaced nodes to the actual crack tip with the former involving actual tip nodes and the latter involving a volume removed from the crack tip area. The third method involves generalization of the *J* contour integral to a three-dimensional surface integral [77] which has been done by authors, such as Amestoy et al [78], and Raynund and Palusamy [79]. The direct, and indirect virtual crack extension methods are applicable to both deformation theory, and incremental theory (*J*-integral and T^*_{ε} integral respectively) calculations and allow straightforward point-wise characterization of the energy release rate. As noted in [64], the generalization of the *J* contour integral to a 3-D surface integral merely gives an overall average value of *J*-integral and would be extremely difficult to evaluate on a point-wise basis.

Sakata et al [80] proposed an extension of the *J*-integral, denoted as the $\hat{J}$-integral. This parameter represents the energy release per unit of a crack-tip translation in a three dimensional, elastic-plastic material. It is not simply a generalization of the Rice's *J*-integral into 3-D. Considering the energy balance on a thin disk during a translation of the crack in the x_1 direction (self-similar crack growth), the $\hat{J}$-integral is given as;

$$\hat{J} = \int\int_A \sigma_{ij}\varepsilon_{ij,1}dA - \int_\Gamma T_i u_{i,1} d\Gamma - \int\int_A (\sigma_{i3}u_{i,1})_{,3} dA \qquad (1.32)$$

where Γ denotes any curve surrounding the crack tip, and A is the area surrounded by the curve and the crack surfaces. In this study, a finite element model was developed to calculate the $\hat{J}$-integral along the crack front for comparison to the ASTM accepted value, which is calculated with the Merkle-Corten formulation [44]. The FE calculated $\hat{J}$-integral was observed to be higher in the center of moderately thick specimens in accordance with what are commonly believed to be conditions of near plane strain. These mid-thickness values also compared well with the values of J_{IC} calculated in accordance with the ASTM standard E-813 [44], indicating the relevance of the ASTM requirement for specific specimen thickness. The path independence of this parameter was also observed by comparing pointwise values along the crack front for different contour sizes.

De Lorenzi [82] derived a general expression for calculation of the energy release rate from an arbitrary crack propagation in a general 3-D crack configuration using a continuum mechanics approach as;

$$G^* = \int_V \left\{ \left(\sigma_{ij} \frac{\partial u_i}{\partial x_k} - W\delta_{jk} \right) \frac{\partial \Delta x_k}{\partial x_j} - f_i \frac{\partial u_i}{\partial x_j} \Delta x_j \right\} dv \tag{1.33}$$

where δ_{jk} is Kronecker's delta, W is the strain energy density, and f_i are body forces. This formula is derived from the general formula for J contour integral by application of the divergence theorem to obtain a volume integral. It is a very general form of the crack tip integral, which is applicable to isotropic or anisotropic materials, as well as conditions of non self-similar crack propagation. Under certain simplifying assumptions, namely that the crack is forced to grow in a self-similar manner and that symmetry conditions are fulfilled (plane strain, or plane stress), this general form will reduce to the 3-D form of the J-integral.

Carpenter et al. [81] performed a review of the proposed path independent integrals intended for inclusion of plasticity effects. The compared parameters included those of

Sakata et al [80], and Amestoy et al. [78] and a newly proposed integral, $\widetilde{J}$, which allowed characterization under an assumption of an incremental theory of plasticity model. For 3-D, this integral is given as the sum of two contour integrals and three area integrals;

$$\widetilde{J} = J_{C1} + J_{C2} + J_{A1} + J_{A2} + J_{A3} \tag{1.34}$$

where;

$$\begin{aligned} J_{C1} &= \oint_{C'} \left(W^e n_1 - u_{i,1} T_i \right) d\Gamma \\ J_{C2} &= \oint_{C'} \left(W^p n_1 \right) d\Gamma \end{aligned}$$

$$\begin{aligned} J_{A1} &= -\int_{S^*} W^p_{,1} dS \\ J_{A2} &= \int_{S^*} \sigma_{ij} \varepsilon^p_{ij,1} dS \\ J_{A3} &= -\int_{S^*} \frac{\partial}{\partial x_3} \left(\sigma_{i3} u_{i,1} \right) dS \end{aligned} \tag{1.35}$$

where superscripts indicate elastic (e) and plastic (p) portions, *C'* is a far-field contour in

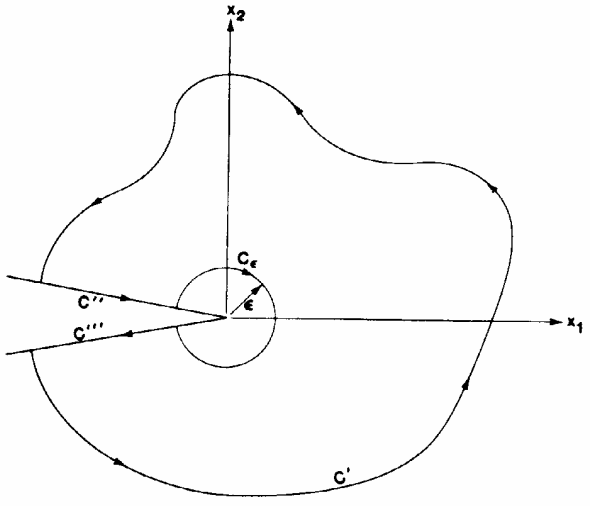

Figure 1.13: Contour of integration for $\widetilde{J}$ [81].

the counter-clockwise direction which does not include the crack faces, S^* is the total surface area defined by C', the two crack faces, and an inner contour, C_ε for the slice, $x_3=0$ (see Figure 1.13). It is easily seen that J_{C1} is Rice's 2-D J-integral. It is also shown that Sakata's $\hat{J}$-integral is simply the sum $J_{C1}+J_{A2}+J_{A3}$, and that Amestoy's integral is $J_{C1}+J_{A3}$, both for nonlinear elasticity. It is noted that the quantities J_{A1}, J_{A2} and J_{C2} are zero for deformation plasticity. This study qualified the various parameters with regard to their energy interpretation with respect to crack extension. The significance of both Amestoy's and Sakata's integrals are unknown for incremental plasticity models, but are interpreted as potential energy release rate per unit of crack extension under an assumption of non-linear elasticity. The $\tilde{J}$-integral is interpreted identically for a deformation theory assumption, but is interpreted as the rate of change of total energy, per unit crack extension for 3-D, incremental theory. In application to a 3-point bend sample, the $\tilde{J}$-integral was observed to be approximately 25% higher in the center than on the surface, similar to the observation by Sakata. While this approach showed considerable promise, it was concluded that the fine-mesh requirements for calculating the $\tilde{J}$-integral can overshadow the viability of using this parameter for 3-D calculations.

Dodds et al. [77] calculated the $\tilde{J}$-integral for a numerical model of a 3-point bend sample, and compared it against an average, experimental J-integral calculated by way of the crack mouth opening displacement (*CMOD*) method suggested by Sumpter and Turner [83]. Here, the experimental J-integral is calculated from the load-versus *CMOD* curve as;

$$J_{\exp} = \frac{K^2}{E} + \left[\frac{P_1 + P_2}{B(W-a)}\right]\frac{WV_P}{a + 0.4(W-a)} \qquad (1.36)$$

where P_1 and P_2 are the loads for establishing an effective limit load. In this study, it was observed that the numerically calculated $\tilde{J}$-integral, and experimental J are both linearly related to the *CTOD* as;

$$J = m\sigma_{flow}CTOD \qquad (1.37)$$

where m is a constraint parameter whose value lies between the computed center plane (higher constraint) value of *1.73*, and the surface value of *1.21*.

Li *et al.* [64], and Shih *et al.* [84] derived 2-D and 3-D domain integral formulation for the *J*-integral. Specifically, in [84], an area/volume domain integral expression for the energetic force in a thermally stressed body was derived. This expression is ideally suited to point-wise characterization of energy release rate along a 3-D crack front because it is naturally compatible with the FE formulation of the crack tip field equations. Point-wise values of *J*-integral are calculated using an analog to the virtual crack extension method employed by Parks [85], whereby the crack is extended successively at each node along the crack front to measure the local energy release per unit of local crack extension. The use of a domain integral is intended to circumvent the difficulties involved in calculating a near-tip value for *J*-integral. In the three-dimensional case, in order for the *J*-integral to be the characterizing parameter in the surrounding *HRR* fields, it must be assumed that a state of plane strain exists. It is argued [64] that as the crack tip is approached asymptotically, the out of plane strain, ε_{i3}, remains bounded while the in-plane strains become singular. Thus, a plane strain state is approximated and the point-wise values of energy release rate may be used in place of the *J*-integral for characterizing the stresses within the *HRR* field. In order for this assumption to be made, however, the inner domain boundary must be shrunk onto the crack tip to capture the near-tip material behavior.

Nikishkov and Atluri [86] presented a 3-D analog to their 2-D, *J*-integral calculation [63] by means of the EDI method. Here, an isoparametric formulation is utilized to calculate the *J* contour integral over a finite domain, remote from the crack tip. Values of *J*-integral are calculated at the center of each crack tip element and a non-straight crack front is accounted for through a point-by-point coordinate transformation. Point-wise *J*-integral is thus calculated through the thickness, including the effects of a curved or

tunneled crack. The author notes that this approach (EDI) presents the opportunity to relatively easily automate the calculation of *J*-integral by means of Matlab, or Fortran programs. The 2-D EDI method has been successfully used for calculation of T^*_ε by many authors [67, 71, 72, 91-93]. After a translation to a 3-D formulation, it should allow calculation of the 3-D T^*_ε integral with the same success.

More recent studies of application of 3-D *J*-integral include those of Dodds and Read [87], Kolednik, et al [88], and Ohgi and Hatanaka [89]. The studies performed in [87] and [89] concern the assessment of 3-D energy release rate for surface cracked structures both experimentally and numerically. Kolednik et al [88] only perform the numerical calculation.

In [87], a surface cracked plate was instrumented with several strain gages along a longitudinal symmetry plane (Figure 1.14) that corresponds to the point of maximum depth of the surface flaw. This allowed experimental evaluation of the contour portion of Carpenter et al's [81] $\tilde{J}$-integral. Finite element results indicated negligible contributions from the area integrals on a symmetry plane, so the evaluation along a longitudinally symmetric contour was seen as a good estimate of the fracture driving force. In comparisons between finite element results and experimental results, exceptional agreement was found between the two for cases of small scale yielding (SSY), net ligament yielding (NLY), and net section yielding (NSY) for measured strains (ε_g) of up to 1.6 times the material yield strain (ε_y) (Figure 1.15). The area integral contribution was found to be approximately 10% of the contour integral contribution. This study represents one of the only attempts at departing from 'mean' *J*-integral value calculations based on *CMOD*, and involves calculating 3-D *J*-integral from experimental strain data obtained on the specimen surface.

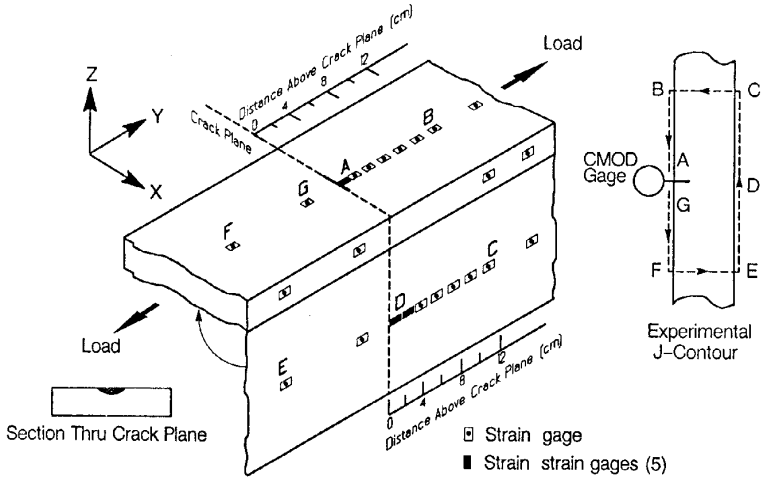

Figure 1.14: Instrumentation for experimental evaluation of 3-D J-integral [87].

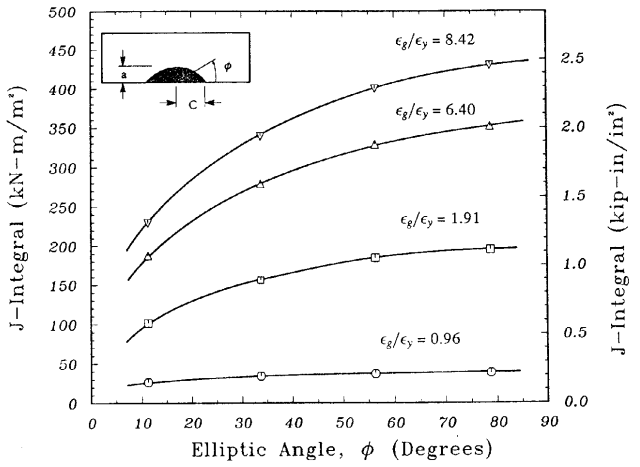

Figure 1.15: Variation of J-integral along crack front for different strain levels [87].

Another approach to calculating *J*-integral was offered by Narasimhan and Rosakis, and Zhender and Rosakis [66, 90]. Here, the method of caustics was used to calculate mean value of 3-D *J*-integral in a plane stress analysis of a 3-point bend specimen. The size of the caustic was calibrated to a *J*-integral curve to allow characterization of *J* based strictly

on the size of the caustic zone. Experimental results were compared to numerically determined results, which were obtained using a 3-D generalization of the *J*-integral (calculated on a 3-D surface contour surrounding the crack tip). This procedure was developed for use in dynamic *J*-integral characterization and is specimen type and material dependent. However, a correlation between *J*-integral and caustic size was found to be obtainable either experimentally, or numerically.

In summary, there seem to be three main methods for calculation of 3-D *J*-integral as discussed in this section. These are methods of virtual crack extension, domain integral methods, and generalized contour integral methods. There seem to be, however, no methods currently available for *pointwise* characterization of *experimental*, 3-D energy change rate. The displacements would need to be measured in slices located within the interior of the sample to provide the required data for such a calculation. There are currently no techniques known which allow for this in opaque materials. For this reason, researchers have typically employed methods such as the *CTOD* measurement technique to calculate an 'average' value of 3-D *J*-integral across the crack front. Alternatively, correlations are drawn between surface phenomena such as caustic zone size, and *J*-integral [66, 90]. All of these experimental approximation methods rely in some form on a numerical analysis to aid in the calculation. It is seen as sufficient to perform extensive numerical analyses of these 3-D integrals and subsequently compare load versus crack extension, or load versus displacement data between numerical and experimental tests. Numerical studies typically employ a virtual crack extension method for calculation of 3-D, point-wise values of the *J*-integral. The work of Dodds and Read [87] represents the most promising of the experimental approaches for 3-D calculation of the *J*-integral. Nikishkov and Atluri's EDI approach [86] provides the basis for simplified calculation of any of the contour integrals via a modification to the virtual crack extension method.

1.6.2 3-D CTOA

In the recent past, researchers primarily at NASA have undertaken the task of qualifying *CTOA* as a stable tearing characterization parameter for thin, ductile aluminum alloys. This includes the work of Dawicke et al. [1] and Gullerud et al. [20] on modeling of tunneling behavior in 2024-T3 specimens. In [1], through a series of FE analyses, it was found that during the initial, transient stage of crack propagation, the *CTOA* is on the order of a few degrees smaller than its steady state value in the center of the specimen and is a few degrees higher on the surface. When steady state (stable tearing) crack growth is reached, the two values become nearly equal and coincide with the typical steady state value. This study used a unique finite element model that incorporated crack tunneling during the initial stable tearing phase which was measured experimentally by fatigue marking the extent of tunneling after subjecting the specimen to various load levels and crack extensions. These crack front shapes were digitized from photographic images and fit with polynomial curves to describe the crack front shape as a function of through-thickness position. The elastic-plastic portion of the FE analysis relied on the incremental theory of plasticity, and was composed of several layers of elements to model the curved crack front. Figure 1.16 shows a typical FE mesh for this study.

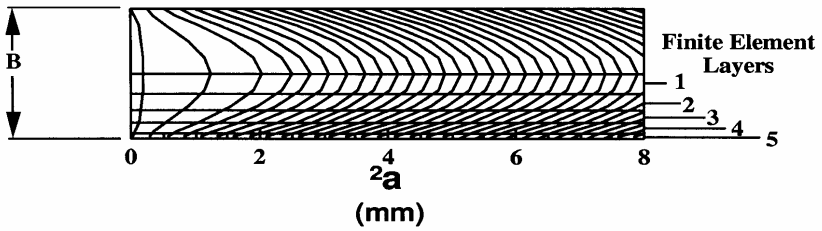

Figure 1.16: Crack front profiles in FE mesh for CTOA [1].

Gullerud et al. [20] use steady state *CTOA* as a crack tip node release parameter for 3-D FE analyses. That is, nodes are released to allow crack extension when all values of *CTOA* are equivalent across the crack front. Following this, the load versus displacement

trends were compared between FE analyses and experimental data. CT specimens of W= 50 and 100 mm were validated in this study, as well as constrained (with buckling guides) 75, 300, and 600 mm wide MT specimens. Errors of between 7 and 9 percent were observed in the CT specimen study, but better agreement was exhibited in the MT specimens.

CHAPTER 2: RESEARCH SCOPE AND OBJECTIVES

2.1 SCOPE

This research is intended to be a study on a potential stable crack growth characterizing parameter for use with 3-D crack fronts. Based on the previous discussion, it is reasonable to approach this subject by focusing on the T^*_{ε} integral since it is the only energetic parameter available which seems to allow reproducible quantification of the energy to fracture in a stable tearing case. Since several numerical and experimental studies [65, 91-93] have recently been applied to two dimensional, plane stress specimens, it also seems reasonable to expand this study into three dimensional characterization for a plane strain state of stress where there is less information readily available with regard to the state of interior material behavior. The previous chapter was dedicated to illustrating some of the more successful attempts at applying stable crack characterization to two-dimensional specimens, and to three-dimensional geometries in the case of 3-D *J*-integral, and three-dimensional FEA analysis of CTOA by Dawicke et al [1]. These studies provide a basis for the current work, which will encompass the characterization of room temperature stable tearing resistance for basic three-dimensional geometries in aluminum 2024-T3 samples.

As suggested by Kanninen and Popelar [8], a scheme for developing a new elastic plastic fracture toughness characterizing parameter would involve a generation-application phase process. In essence, data corresponding to crack initiation and stable crack growth is gathered. This data collection will involve numerous specimen types, and specimens of each type to establish consistency. The output from this so-called "generation phase" will then be used in an "application phase" to predict the load and crack growth behavior in a candidate material. The application phase will be numerical in nature (finite element modeling). This generation, application phase approach is the foundation of the current

study which is intended to determine the feasibility of calculating the T^*_ε integral in the generation phase.

2.2 RESEARCH OBJECTIVE

The objective of this research is to numerically and experimentally characterize the T^*_ε integral under stable tearing conditions in a thick aluminum 2024-T3 aluminum sample. The numerical characterization will be on a point-wise basis, through the thickness, along a tunneling crack front. Experimental values are only obtainable on the surface of the specimen and will therefore be used to compare against average, through-thickness, numerically obtained values.

To truly model the triaxial state of stress at the crack tip, a three-dimensional analysis is needed. This approach has been avoided in the past, primarily due to the cumbersome nature of performing a 3-D analysis and because an approximation may be obtained with a 2-D analysis by utilizing several assumptions. A 3-D analysis is proposed to provide a thorough understanding of crack tip behavior. The experimental analysis here will provide a benchmark with which to compare results from a numerical model, which will be developed in its generation phase using a hybrid experimental numerical approach [70-72, 93]. When the model is fully developed within the context of the generation phase, it is hoped that it may then be applied in an application phase in future studies to estimate the stable tearing toughness of aluminum structures under normal operating conditions with pre-existing flaws.

CHAPTER 3: METHODS OF APPROACH

3.1 SPECIMEN CONFIGURATION

To permit a valid, 3-D analysis, the thickness of the specimen to be tested should be in the transitional stage between a state of plane stress, and a state of plane strain. In addition, since the objective of this study is to build a fracture resistance curve through a stable crack extension on the order of the specimen thickness, a fairly thick specimen must be used. In plane stress specimens, the T^*_ε integral has been observed [71, 72, 91-94] to reach a steady state value at a crack extension approximately equal to the thickness of the sample. Thicker, plane strain specimens may reach steady state at a different crack extension.

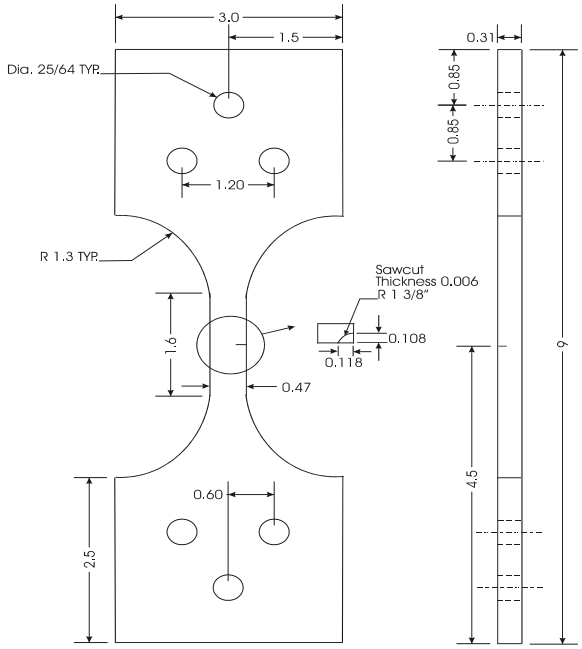

Figure 3.1: 3-D, semi-elliptical flaw aluminum 2024-T351 specimen.

Figure 3.1 shows the sample used in an initial attempt at observing T^*_ε behavior in thick, plane strain samples. Unfortunately, the stiffness of the Instron loading frame that was used for these tests was not sufficient to allow extensive stable tearing in this relatively thick, tensile type specimen. Failure loads for this specimen configuration were of the order of 30 to 35 KN, which is a significant portion of the 45 KN capacity of the load frame available for testing. The highly compliant load frame tends to store elastic energy at these load levels, which is eventually released through the specimen flaw, resulting in unstable crack propagation.

To allow a sufficient amount of stable crack propagation in a 3-D flaw specimen while avoiding the problem of larger than desirable machine compliance, a very low compliance specimen must be utilized. The two most obvious of these specimens are the 3-point bend specimen and the wedge loaded double cantilever beam (DCB) specimen. From historical and practical standpoints, the 3-point bend sample is the most relevant candidate geometry. Several of the 3-D *J*-integral studies that have been carried out [84, 90] have utilized the 3-point bend specimen. In addition, if the need arises, the 3-point bend specimen will allow replication of a moiré grating on both sides of the specimen for additional data recording. The expected, significant crack tunneling in a thick, 3-point bend specimen will allow simulation of a 3-D flaw in the same manner as the studies of Dawicke [1] and Gullerud et al [20]. The amount of tunneling will be a function of specimen thickness, so a fairly thick specimen must be used. Figure 3.2 is a graphical representation of these two specimen types.

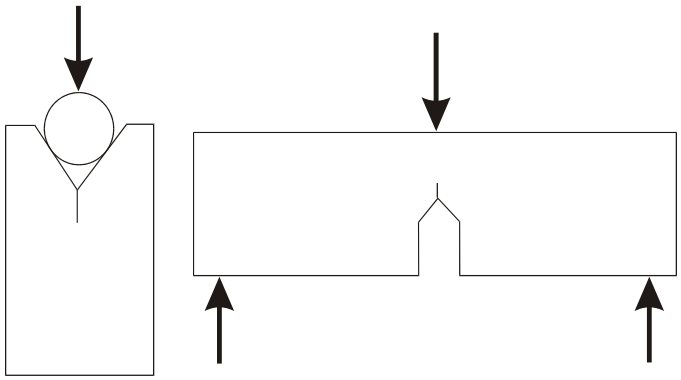

Figure 3.2: Wedge loaded DCB and 3-Point Bend [SENB] specimen geometries.

The other possible specimen is the surface cracked tensile sheet similar to that used by Dodds and Read in their experimental study of the 3-D contour *J*-integral [87]. Unfortunately, similar to the 3-D elliptical flaw sample discussed previously, this sample will likely approach the stiffness limits of the load frame. However, a small enough specimen could provide usable moiré interferometry data.

For this study, the three point bend [ASTM SE(B)] type geometry is chosen in accordance with the reasoning above. It is assumed that a stable crack propagation length of approximately five millimeters will be sufficient for T^*_ε characterization in this study. Therefore, a specimen width, W = 25.4 mm with an initial notch size, a = 10.75 mm is chosen to give a value of a_0/W=0.42. This specimen roughly complies with the ASTM Standard (E 813) for *J*-integral testing, where a_0/W should be approximately 0.5, including the fatigue pre-crack. This standard dictates that the support span (S) be approximately four times the width (W) so the specimen is chosen to be 115 mm. Figure 3.3 shows the specimen used for this study.

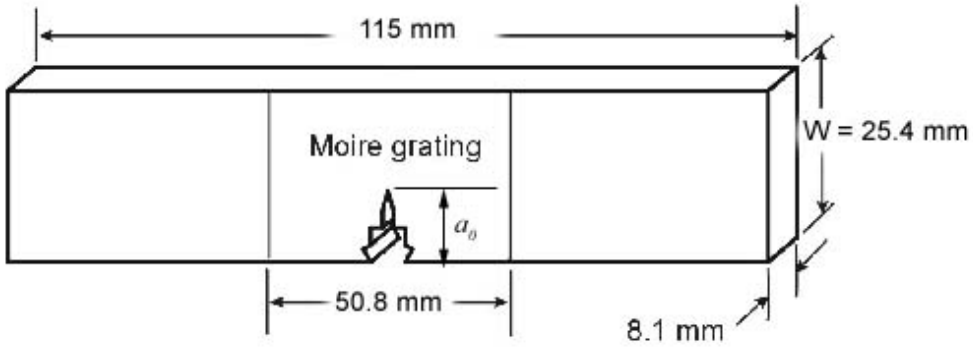

Figure 3.3: Three Point Bend [SENB] specimen.

The material chosen for this research is 2024-T351 aluminum alloy. This alloy is typically used in airframe structures and thus represents an important class of materials for which fracture properties must be characterized. In addition, it has been used in several prior studies [91-94] for characterization of the T^*_ε integral and will allow comparison for validation of the proposed research. 2024-T351 aluminum is sufficiently ductile to generate a sizable elastic-plastic crack tip region. For the 3-D T^*_ε integral analysis, an 8 mm thick plate stock will be used and the specimens are machined in the L-T orientation so that the plane of the crack lies parallel to the rolling direction. Table 2 lists the published major characteristics of this alloy. Table 3 is a test matrix for the experimental work.

Table 2: Properties of 2024-T3 aluminum alloy [103].

σ_u (MPa)	σ_y (MPa)	E (GPa)	G (GPa)	ν	T_m (^{0}C)
485	345	72.4	28	0.33	502

Table 3: Test matrix for T^*_ε evaluation.

Specimen	**Specimen Geometry**	**Peak Load (KN)**	**End Load (KN)**
JHJ01, JHJ02, JHJ03	Dogbone (ASTM tensile) 8.1 mm thick	N/A	N/A
T6-3PB	3 Point Bend, 8.1 mm thick (a_0/W=0.45, Δa=0.5 mm)	4.16	3.79
T4-3PB	3 Point Bend, 8.1 mm thick (a_0/W=0.45, Δa=1.75 mm)	4.17	2.85
T3-3PB	3 Point Bend, 8.1 mm thick (a_0/W=0.45, Δa=3.0 mm)	4.10	2.15
T2-3PB (not used)	3 Point Bend, 8.1 mm thick (a_0/W=0.55, Δa=3.0 mm)	3.70	1.63
T1-3PB (not used)	3 Point Bend, 8.1 mm thick (a_0/W=0.53, Δa=4.0 mm)	3.93	1.70
T5-3PB	3 Point Bend, 8.1 mm thick (a_0/W=0.45, Δa=5.5 mm)	4.20	0.97

Since the numerical analysis portion of this research will rely heavily on the plastic portion of the stress-strain curve, the material properties listed here are only used as a reference. Uniaxial tension tests were performed in a direction perpendicular to the rolling direction on three dog-bone specimens machined from the same plate stock as the three point bend specimens used in the study. Figure 3.4 shows the data obtained from this testing, including relevant parameters of strain hardening exponent (n), and the so-called “plastic” modulus (a), which are used in the Ramberg-Osgood curve fit. This material data is prescribed in both the experimental and numerical analyses.

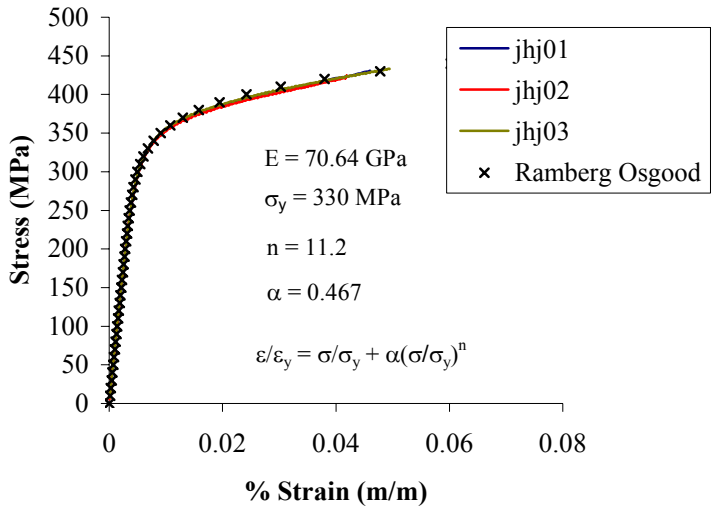

Figure 3.4: Measured tensile properties for 2024-T351 used in this study

3.2 EXPERIMENTAL ANALYSIS

3.2.1 DATA COLLECTION

A high-accuracy displacement measurement method must be utilized to calculate full field strain with resolution desired for experiments of this type. These surface displacement measurements must be of the full-field type. That is, a relatively high-resolution map of displacements in both *x* and *y* directions must be available at each stage of crack growth. These types of measurements tend to lend themselves toward optical techniques of one sort or another. The method most commonly used by researchers who have employed Okada's experimental T^*_{ε} calculation procedure [70], is a technique known as moiré interferometry [71, 72].

Moiré interferometry is described in detail by Post in [98]. In essence, it is an optical technique involving interference of two collimated beams of light at the surface of a specimen. The two interfering beams create a regular array of lines in space, which interact with the reflected light from a diffraction grating replicated on some surface. As the physical grating deforms with the surface, a fringe pattern is formed due to interference between the diffracted light field and the original light field. Each fringe that is produced represents a measure of in-plane displacement at each point as a function of the grating frequency. The displacements are given as:

$$u_i = \frac{1}{f} N_i \qquad \text{for } i=1, 2 \tag{3.1}$$

In equation (3.1), the subscript i represents either of the Cartesian directions, f is twice the specimen grating frequency, and N is the whole fringe number. From this formula, it is easily seen that the resolution of displacement measurements is a direct function of the specimen grating frequency. This must be carefully taken into account when considering the grating for use in testing.

When used with a grating consisting of a grid pattern parallel to both the x and y directions (cross grating) and four orthogonal collimated beams, the moiré method has the capability of measuring both displacement fields. The sensitivity of the measurements is easily adjusted within certain limits. For measurements of displacement in metals, a very high frequency grating is needed. These gratings are typically created using photographic techniques described in detail by Ifju and Post [99].

Another common method for measuring in-plane displacements called digital image correlation (DIC) was employed by Newman et al [14] for obtaining CTOA values. It involves coating the specimen surface with a speckle pattern and comparing images of the deformed surface with images of the undeformed surface. While DIC has produced very good results, it is usually used in applications where large deformations are

expected. Therefore, for this research, the high resolution attainable with moiré interferometry is desirable. However, DIC methods may need to be utilized for creep fracture studies.

The method described by Wang et al [100] is applicable when measuring relatively large deformations. This method utilizes a low spatial frequency steep grating of about 40 lines/mm on a highly polished surface to achieve very high contrast fringes. It combines the advantages of the geometric and traditional moiré interferometry methods to allow measurement of large deformations. Here, two collimated beams are directed onto the surface of the specimen at a very shallow angle of approximately 6 degrees. A moiré pattern is visible to the naked eye and can be photographed without the need to capture the 1st order diffraction, which is the typical way to extract moiré data. Figure 3.5 shows the method used to create these gratings.

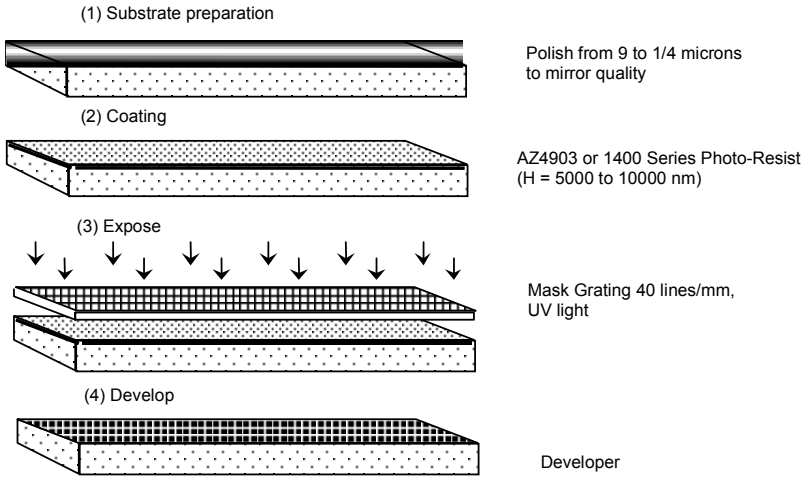

Figure 3.5: Photo-resist grating replication procedure [101].

3.2.2 SPECIMEN TESTING APPROACH

For the 3-D T^*_ε integral study, specimens were cut from plate stock aluminum and machined to the specified geometry. The specimens were then fatigue pre-cracked to produce a sharp, natural crack on the order of 1.5 mm. This fatigue pre-cracking

followed the recommendations in ASTM standard E-813 for *J*-integral testing. In essence, specimens are subjected to a 15 Hz sinusoidal waveform loading with a load ratio, R=0.1, and not exceeding 60% of K_{IC}, the material's accepted linear elastic fracture toughness ($K_{IC} = 33Mpa\sqrt{m}$ for 2024-T3 aluminum). Each specimen endured approximately 10,000 cycles to produce the 1.5 mm fatigue pre-crack.

Following fatigue pre-cracking, the front side of the specimens were polished to a mirror surface finish of 1 μm through a series of several polishing stages, beginning with 200 grit, wet-dry sandpaper. This was done to prepare the specimen surface for application of a photo-resist type moiré grating. Following the procedure graphically depicted in Figure 3.5, the moiré grating was applied via a photo-resist spin coating method. Here, photo-resist was dripped on a specimen that was being spun at high speed in a modified centrifuge. The grating was applied by exposing the photo-resist to high intensity light through a 40 line/mm mask, and then developing it in a developer solution. The back side of each specimen was also marked at intervals of 0.25 mm (Figure 3.6) to record levels of crack extension on the surface.

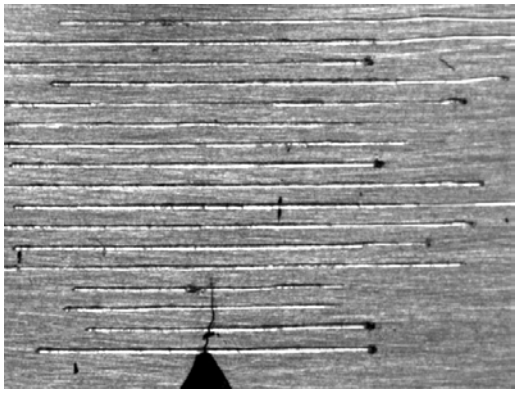

Figure 3.6: Back side of 3 Point Bend specimen showing crack level markings at 0.25 mm increments and pre-fatigue crack.

Following the aforementioned preparation, the specimen configurations listed in Table 3 were subjected to a monotonic load in a screw driven, displacement controlled Instron, 45

KN capacity load frame. A moiré interferometry bench, which has been previously constructed, [91] was used to capture the displacement fields in both *u* (parallel to crack), and *v* (perpendicular to crack) directions during specimen testing. The specimens were monotonically loaded at a rate of 0.254 mm/min until stable crack growth initiated. Here the test was stopped and the first displacement fields were captured via a CCD camera, connected to a frame grabber in a Windows NT computer. The load rate was then reduced to 0.127 mm/min to maintain stable crack propagation and the ensuing monotonic loading was stopped at crack extension intervals of 0.25 mm to again capture the *u*, and *v* displacement fields. Photographs of the experimental setup are shown in Appendix C.

Since the 3-D flaw analysis will rely on the tunneling present in the interior of the specimen, the experimental approach involved marking the crack front at various crack extensions by post-fatigue marking. Six different specimens were tested in this experimental work and each was loaded to a different crack extension length to provide a view of the tunneling behavior as the crack extends. Post-fatigue cycling was used to mark the new crack front in a similar manner compared with pre-fatigue cycling. However, since the extent of tunneling was unknown prior to fatigue marking, an estimated average crack length had to be used for calculation of the K_{IC} values. This tunneling analysis is similar to the approach used by Dawicke [1], and Gullerud et al [20] in their 3-D *CTOA* analyses. The post-fatigue crack front profiles were digitized into a computer from photographic images and curve fit to allow it to be mapped in the finite element model. Figure 3.7 shows a typical specimen fracture surface and its corresponding, digitized crack front.

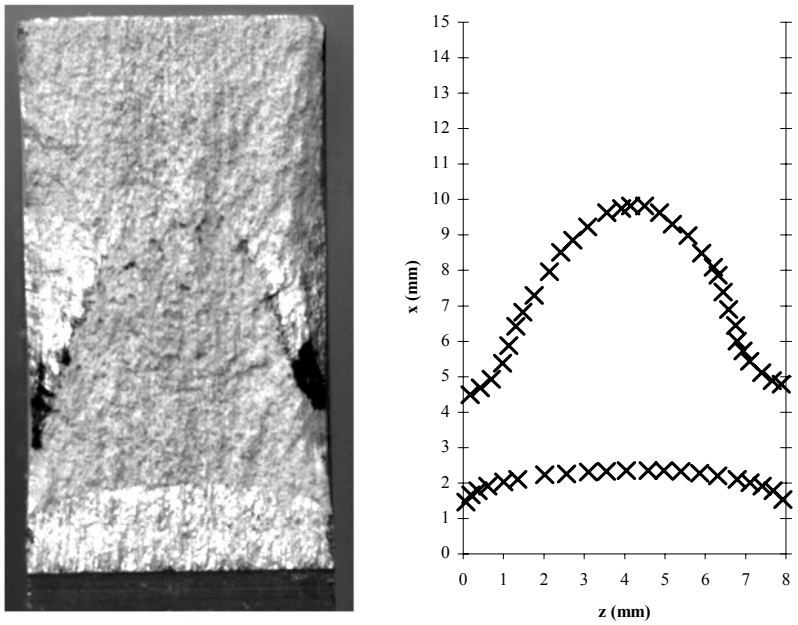

Figure 3.7: Typical pre, and post-fatigue crack profiles.

3.2.3 CALCULATION OF EXPERIMENTAL (SURFACE) T^*_ε

Currently there are no known methods available for calculating T^*_ε in a point-wise fashion along a tunneling crack front from experimental data, which is limited to measurements on the specimen surface. If an assumption of plane strain is made for the location of the integration contour, these experimentally obtained surface values should be comparable to the average of the numerically obtained, point-wise, through-thickness values calculated along this same contour. Once the size of the integration contour is set at the point of transition in plane states, it should be used for all levels of crack extension for both experimental, and numerical calculations because the calculation becomes essentially a 2-D comparison. Values of experimental T^*_ε are calculated by performing a truncated contour integration at this distance from the crack. The calculation utilizes measured surface displacements and the material constitutive relationship to obtain values of T^*_ε at each level of crack extension.

A program was written in Matlab® 5.1 to allow calculation of displacements at chosen node points on the surface of the specimen (Appendix B). The program first imports the previously saved data file. A grid of x-y coordinates with resolution defined by the user is then assigned to the data set. A "nearest point" interpolation routine calculates the approximate fringe number at each of the grid points by interpolating between whole fringe numbers from the original data set. In this manner, each of the grid points is assigned a fractional fringe number. The fringe numbers are then multiplied by the half pitch of the specimen grating to obtain a displacement at each point. This displacement data is output in a three-column text file containing x-y coordinates of the grid in the first two columns, and displacements in the third column. As a final step, a contour plot of the displacement is created so that the user can determine if the data is acceptable. Figure (3.8) shows contour plots from this program of data corresponding to the images in figure (3.9).

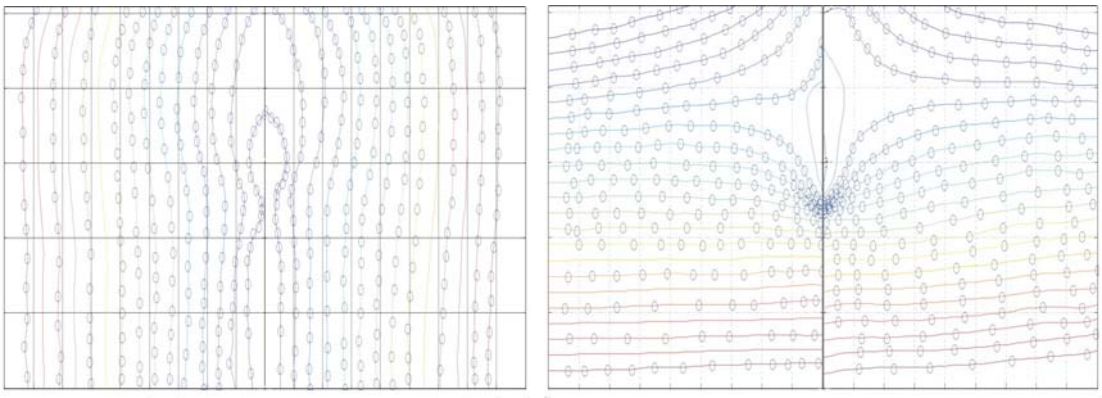

3u4 3v4

Figure 3.8: u and v-field displacement contours from digitized moiré, Δa=0.5 mm.

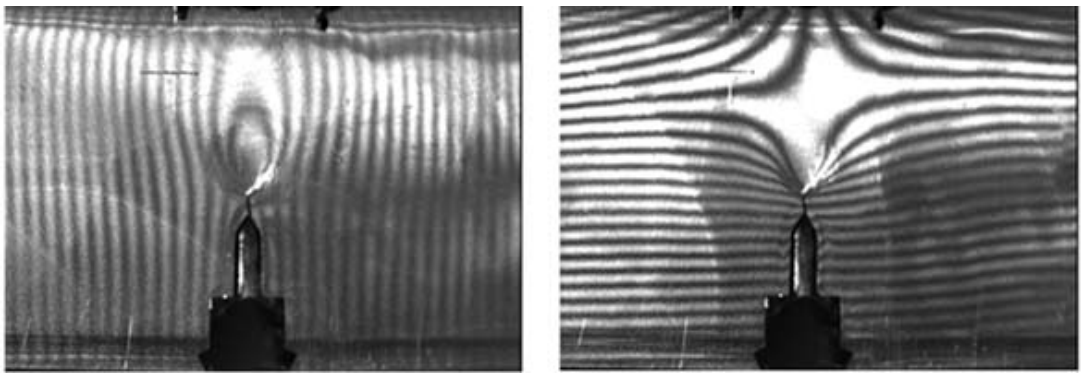

3u4 3v4

Figure 3.9: Typical moiré fringe patterns from experimental work, Δa = 0.5 mm.

For this work, a grid resolution of 0.25 millimeters was chosen. This allowed relatively accurate correspondence of the crack tip to a node, and optimized the accuracy of the interpolation scheme. Displacements were calculated over a fixed interval, which spanned from 2 millimeters behind the crack tip to 7 millimeters in front of, and above the crack tip (total window size of 7 x 9 mm). The displacement data from the left half of the specimen was "mirrored" onto the right half, and a point-wise average value was taken for each of the node points. Any rotation in the fringe pattern was corrected for by averaging the left and right data sets.

The displacement data calculated using the aforementioned Matlab® program was used as input data for calculating experimental values of T^*_{ε}. Two input files were created for each data set. The first input file is simply a four-column text file containing node number, *u*-displacement, *v*-displacement, and *w*-displacement in the first through fourth columns respectively. For these data sets, *w*-displacement (out of plane) was set to zero for every point. The second input file was an ABAQUS® mesh file containing element connectivity, and node-element assignments.

A FORTRAN program to calculate T^*_ε was written at Georgia Institute of Technology in 1996 by C. Pyo and H. Okada. The program was then modified by Y. Omori to calculate T^*_ε based on the experimentally obtained displacement data and material properties. This program was based on the work by Okada et al. in [70]. For each calculation of T^*_ε, an initial crack tip is specified, along with an integration contour size, and EDI region size. Displacement data is then used by the program to calculate strains from which stresses are calculated using the equivalent stress-strain relation. Finally, T^*_ε is calculated using the stresses and strains with Okada's truncated EDI method, and a deformation theory of plasticity as suggested in [70].

3.2.4 CALCULATION OF EXPERIMENTAL 3-D T^*_ε

It would be most beneficial to have the ability to calculate the locally varying T^*_ε integral in a point-wise fashion along a 3-D crack front. However, the absence of a technique for obtaining displacement values within the interior of the specimen will inevitably require a mathematical modeling of the interior state. Several, untested possibilities exist for estimation of a 'mean' 3-D energy parameter. These include a method similar to that utilized by Dodds and Read [87], in which only the contour portion of the integral was obtained experimentally, and estimates of the remaining area integral are provided by FE analyses. Here, the T^*_ε integral would be calculated along a truncated contour, analogous to the way 2-D *J*-integral and T^*_ε integral are related. It is tempting to use a crack tip geometry interpretation for the estimation of a 'mean' energy release rate term, but no direct correlations have been made between T^*_ε and crack tip geometry parameters such as *CTOD* as they have between *J*-integral and *CTOD*. For now, it is assumed that by analogy to the relationship between the 2-D *J*-integral and 3-D *J*-integrals, the 3-D T^*_ε integral may be calculated along a truncated contour, albeit extended an additional dimension. Since measurements cannot be made in the interior of the specimen, this would conceivably be done on two surfaces of the specimen to allow an estimate of average T^*_ε through the thickness which may then be compared with the local, point-wise

values obtained numerically. However, since the 3-point bend specimen is symmetric, calculation on both sides would be repetitive. Therefore, with the absence of a method for through-thickness, experimental contour integrations, a surface value of the experimentally determined T^*_ε must suffice for the time being. As stated previously, the surface value of T^*_ε will be compared with the numerically obtained, average through-thickness values if the contour of integration is set at the point of transition in plane states.

3.3 NUMERICAL MODELING

3.3.1 THE T^*_ε INTEGRAL FOR 3-D GEOMETRIES

The principles of virtual crack extension have been applied successfully by many of the authors discussed in Chapter 1. These methods rely on comparison of strain energy present in two different cracked configurations. Since the value of the T^*_ε integral lies mainly within its use with the incremental theory of plasticity, these methods will be applicable only if it is assumed they are valid for incremental plasticity which has been suggested by Sakata et al [80]. The method employed by Nikishkov and Atluri [86] for numerical analysis of the *J*-integral is likely more applicable for use here as it allows characterization under the incremental theory of plasticity at a location removed from near crack tip events. For this study, an extending contour and the incremental theory of plasticity is used to calculate the T^*_ε integral for the 3-D numerical model. The model is built to accommodate the tunneling behavior of a real crack (see figure 1.12). Thus, the resolution of the mesh in the *z* direction (parallel to the crack front) must be sufficiently refined to model the acute crack front curvature seen in actual specimens. This resolution is empirically determined using experimental measurements as a basis. Stresses and strains are recorded at each stage of crack extension along the elements within each layer that encompass the crack front for calculating the local T^*_ε integral value at several points along the crack front. Figure 3.10 is a graphical representation of the contour of

integration for a representative layer. Note that ε is a small quantity such that the contour is close enough to capture the crack tip behavior while avoiding numerical difficulties associated with extreme plasticity in the near-tip process zone or the influence of external boundary conditions.

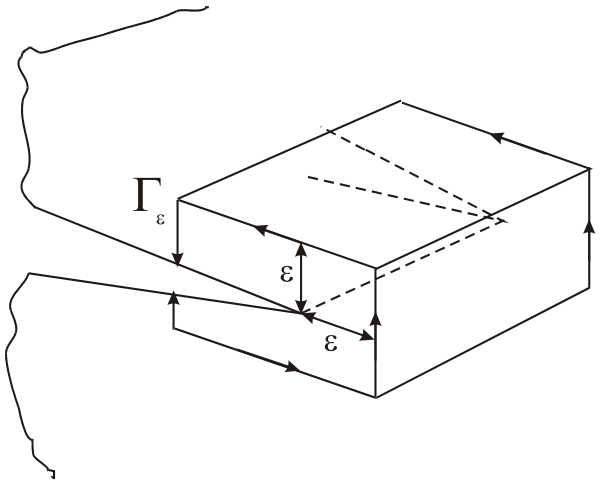

Figure 3.10: 3-D T$^*_\varepsilon$ *contour of integration.*

3.3.2 NUMERICAL MODEL OF 3-POINT BEND SPECIMEN

Since it is inefficient to model the entire specimen, one quarter of the 3-point bend specimen was modeled due to symmetry, and this quarter-model is further truncated at a prescribed distance from the plane of the crack. In the first step in the hybrid experimental-numerical approach, a finite element analysis utilizing a relatively course mesh was carried out on a full quarter model of the 3-point bend specimen. Since interior conditions along the 3-D crack front cannot be measured and/or prescribed, this initial analysis allowed the determination of the distance from the crack plane where the states of stress and strain are uniform through the thickness of the specimen. Displacements are then measured experimentally at this distance from the crack plane, and prescribed as boundary conditions to the FE model.

The 8 mm thick, 3-point bend specimen (Figure 3.3) is modeled in the commercial Finite Element Analysis (FEA) code, ABAQUS using 8 node, isoparametric, brick elements with incompatible modes for control of shear locking. As previously discussed, symmetry allows one quarter of the specimen to be modeled, and the model is further truncated at a specific distance from the crack plane for computational efficiency. This distance was determined by building an initial full quarter model of the specimen with a relatively course mesh of 0.5 mm elements in the vicinity of the crack tip and transitioning to 1.0, and 2.0 mm elements further away. The coarse model (Figure 3.11) contained only four elements through the half thickness of the specimen.

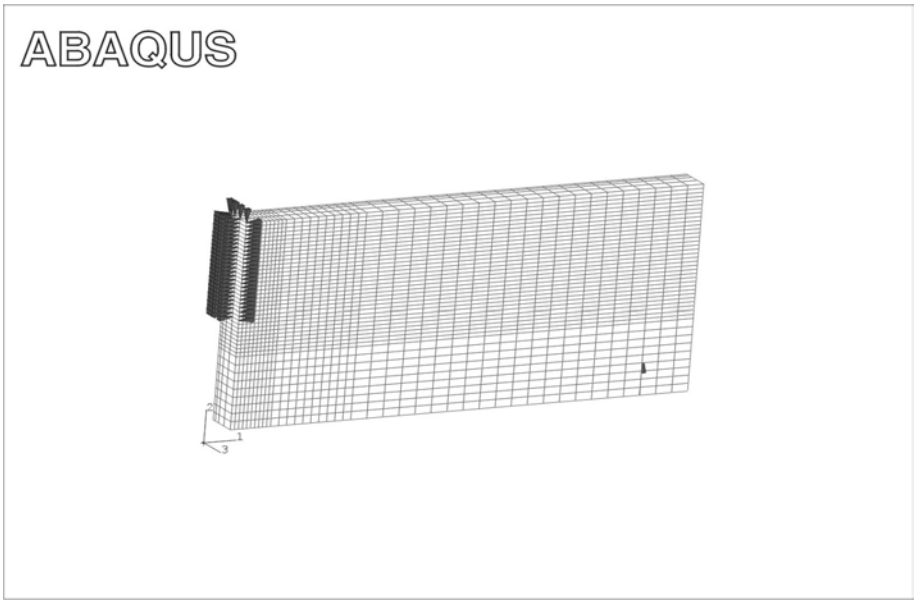

Figure 3.11: Initial, course model for determination of truncation boundary.

The coarse model was loaded to a level equivalent with the load at which crack extension was expected to have begun which will be close to the maximum load the specimen will support. From experimental observations, this value was taken to be approximately 3.6 KN for crack initiation. The von Mises stress (Figure 3.12) was obtained at the centroid of each of the elements through the thickness and at several different distances from the

crack face. A truncation distance for prescribing experimentally obtained displacements in the FE model was determined as the distance from the crack face where the von Mises stress was approximately constant through the thickness. Figure 3.13 is a set of typical plots of von Mises stresses through the thickness at specified distances from the crack plane, and at several points in the x-direction (height). For this analysis, the truncation distance was determined to be at *y=15 mm*.

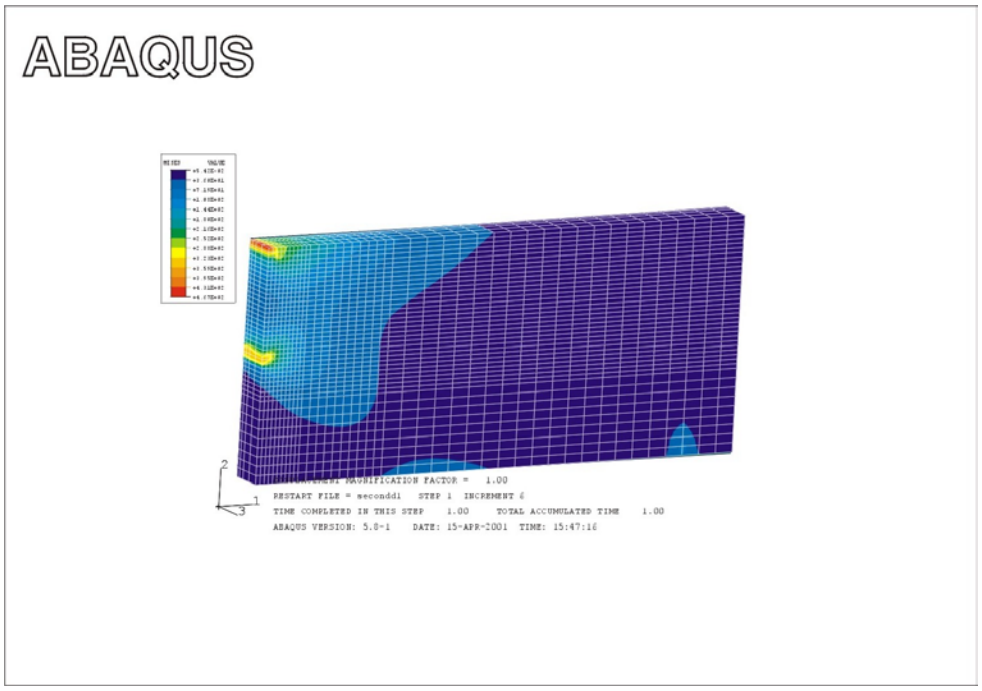

Figure 3.12: Distribution of von Mises stress in course, initial model with P=3.6 KN and a=12.5 mm.

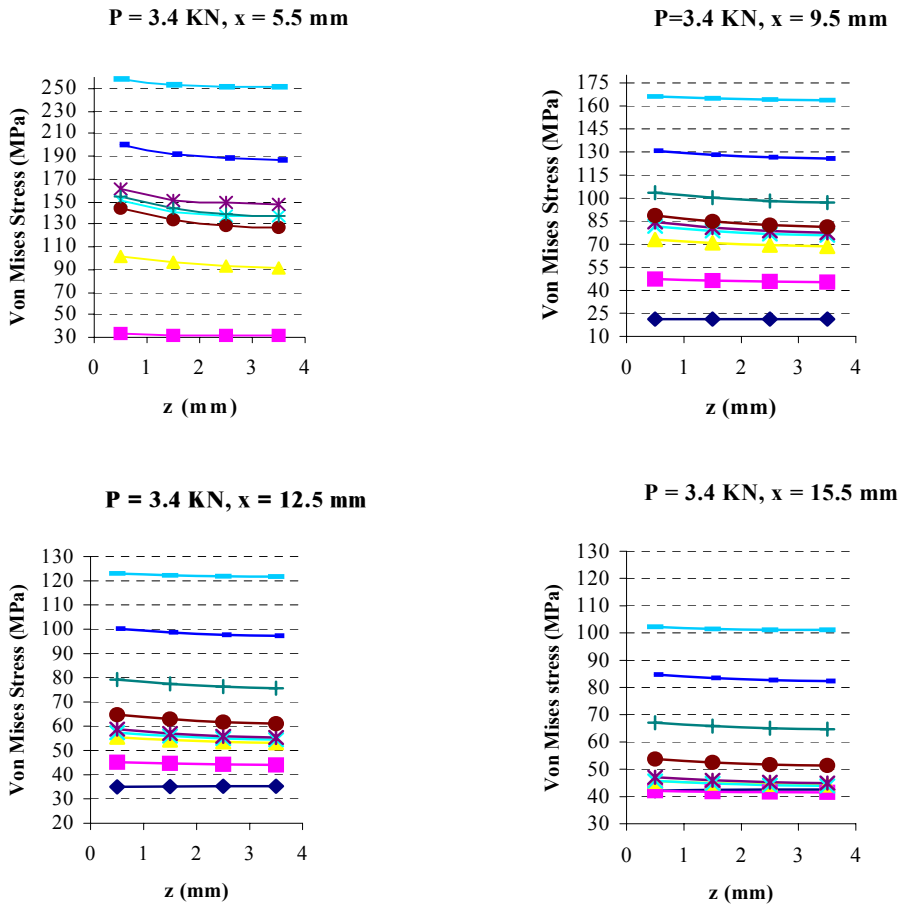

Figure 3.13: Von Mises stresses through the thickness for varying distances from the crack plane, Δa = 0.00 mm.

The application of boundary conditions at a truncation point in the case of bending is a complex issue. The *v*-displacements (normal to the plane of the crack) are easy enough to apply as long as they vary linearly from top to bottom. However, special care must be taken with application of *u*-displacement boundary conditions at the y=15 mm truncation point since it is very easy to introduce improper loads with these boundary conditions. It is therefore sufficient, and necessary to apply the *u*-displacement boundary condition at only one point on the 15 mm truncation boundary since the *v*-displacement ensures a

bending condition and the *u*-displacement is approximately constant in the vertical direction. At least one prescribed *u*-displacement is required to enforce the shear condition in the 3-point bend specimen. To ensure that the *u*-displacements were prescribed to reflect reality, several different scenarios were explored in a simple 2-D model of one quarter of the specimen with actual bending employed (Figure 3.14). Figure 3.15 shows the different methods of boundary condition application explored. Shear stresses were extracted from a set of elements 2.5 mm behind the truncation plane for comparison. This extraction point is chosen so that stresses are not influenced by application of boundary conditions on the truncation plane. Figure 3.16 is a plot of these shear stresses and shows that case (c) from Figure 3.15 offers the best comparison in shear condition to the full model. Therefore, the final 3-D model incorporates this scheme for application of displacement boundary conditions.

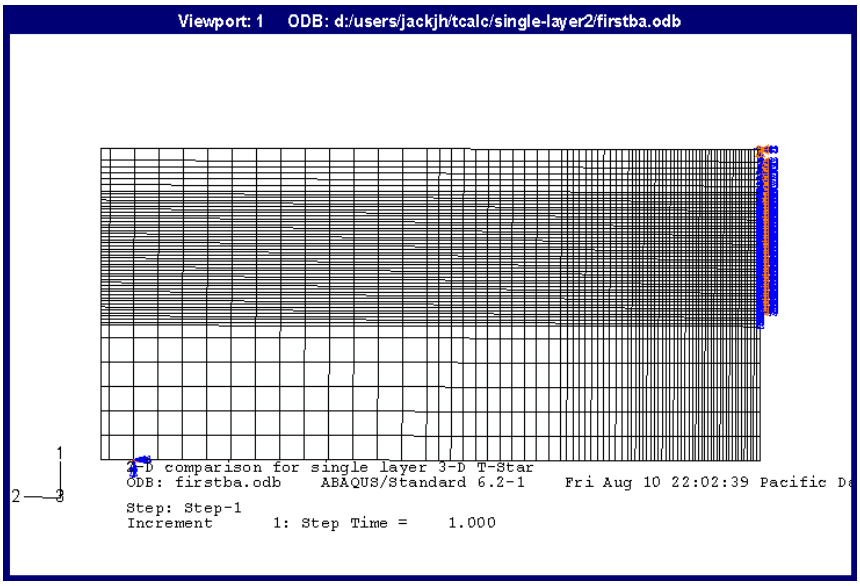

Figure 3.14: 2-D model for verification of boundary conditions.

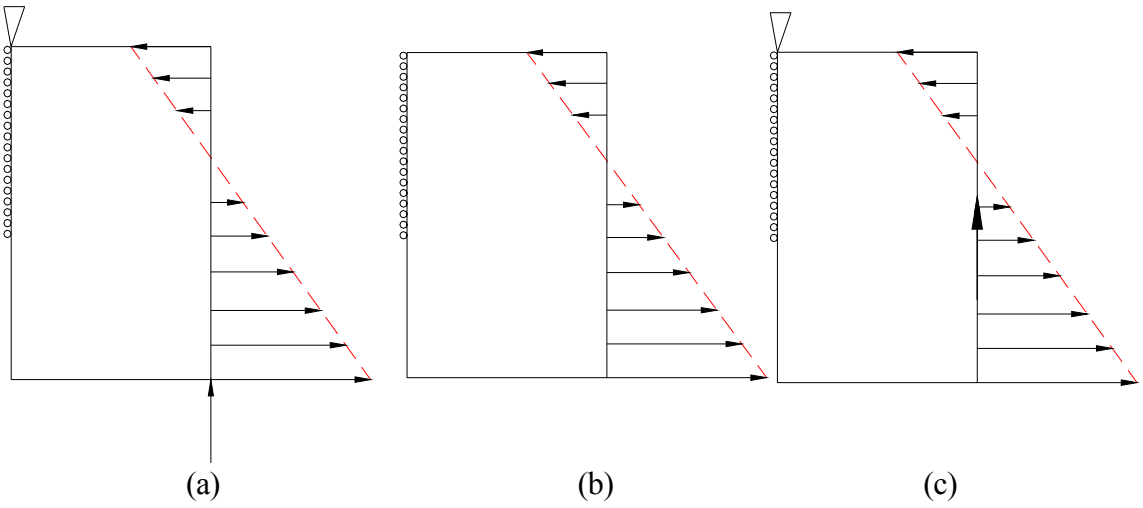

Figure 3.15: Application of boundary conditions for simulation of bending.

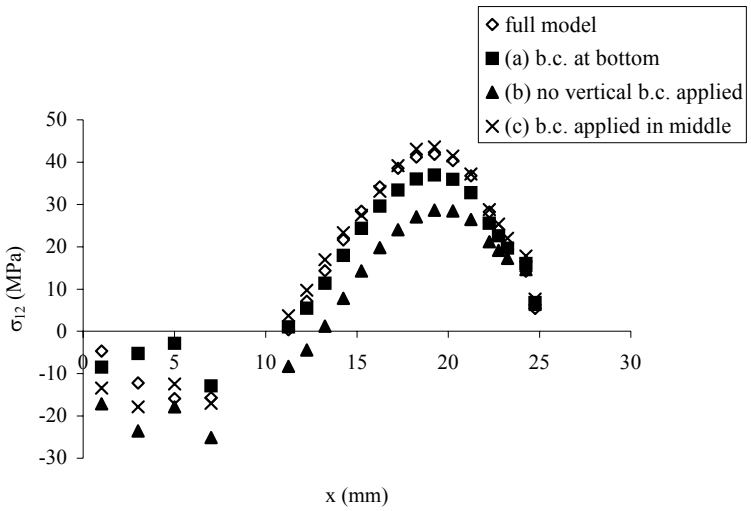

Figure 3.16: Shear stress distribution through specimen width near boundary for $\Delta a = 0.00$ mm.

The final model used in this analysis is shown in Figure 3.17. The extent of tunneling seen in the experimental analysis required a sufficient resolution of element layers

through the specimen thickness (Figure 3.8). To accommodate the extreme slope of the tunneled crack front, thin (0.25 mm) layers were utilized in the areas of the steep crack front gradient with a transition to thicker, 0.5 mm element layers near the center of the specimen where the crack front gradient is not as large. The final model (Figures 3.17, 3.19) consisted of ten, 0.25 mm thick layers near the outer surface followed by three, 0.5 mm thick layers to total the specimen half-thickness of 4.0 mm for a total of 13 element layers. This arrangement of layering also helps to accommodate the natural surface singularity that is expected near the free surface. Element sizes were 0.25 mm in the *x*, and *y* directions near the crack tip area and transitioning to 0.5 mm and 1.0 mm further away. Figure 3.17 also shows the model *y*-direction truncation distance of 15 mm, with experimentally obtained displacement boundary conditions prescribed.

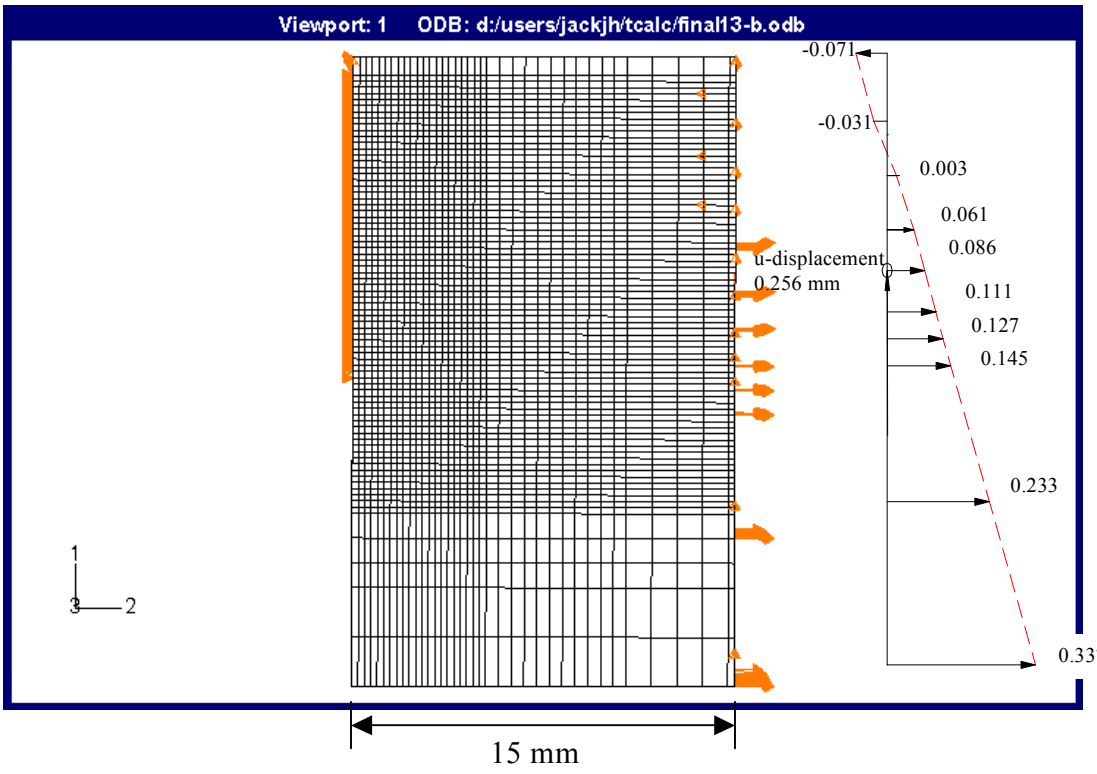

Figure 3.17: Side view of final, 13 layer model with boundary conditions at Δa = 0.75 mm.

Figure 3.18 shows the crack tunneling profiles for one side (symmetry) of the specimen, with the polynomial curve fits for each crack extension. These tunneling profiles were prescribed as boundary conditions defining the crack face in the final model as seen in Figure 3.19 where the remaining ligament nodes have been prescribed in accordance with the third crack extension level in Figure 3.18.

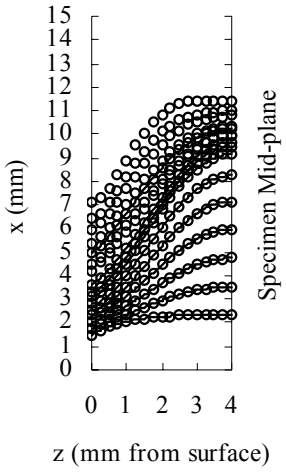

Figure 3.18: Curve fit, symmetry crack tip boundaries.

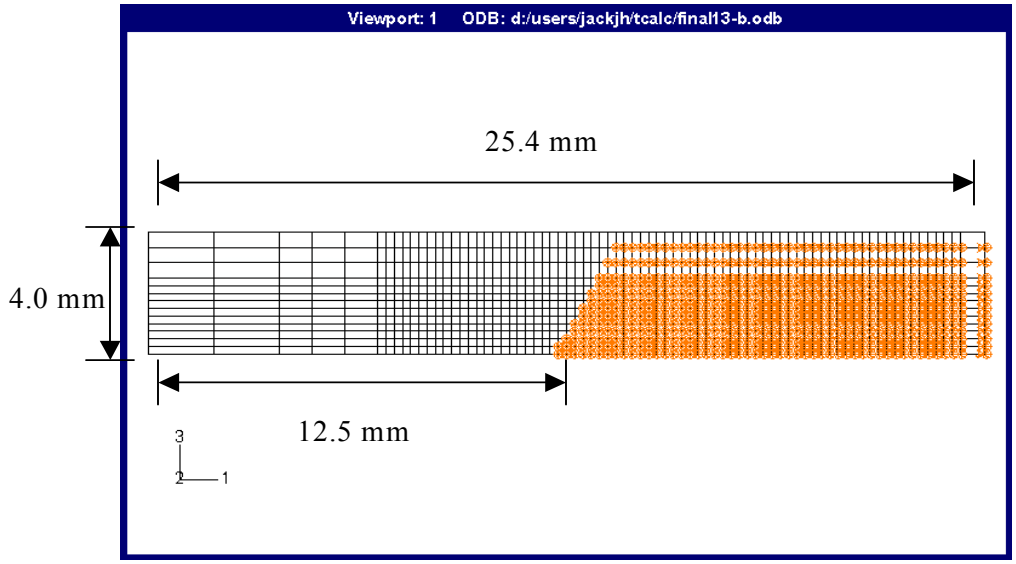

Figure 3.19: Typical crack face profile in final, 13 layer model.

3.3.3 POST PROCESSING OF NUMERICAL ANALYSIS

No commercially available finite element analysis packages currently incorporate the incremental formulation for calculating *J*-integral, or any other contour integral for a 3-D curved crack front. Post processing software has been successfully written in the Fortran programming language by at least two groups, Okada et al. [70] and Ghadiali and Brust [95], both of which are based on Nikishkov and Atluri's paper [69]. Unfortunately, these programs were designed primarily for two-dimensional analysis, with the exception of Ghadiali and Brust's program [95], which had been written to handle three-dimensional analyses, but has been used only up to the point of crack initiation. Therefore, a major portion of this research involved the development of post processing software for calculation of the T^*_{ε} integral in three dimensions and including extensive crack front tunneling. The equivalent domain integral method (*EDI*) suggested by Nikishkov and Atluri [86] provided a means for calculating the T^*_{ε} integral and was utilized here for formulation of the post-processing software. A detailed explanation of the mathematics

outlined in [86] is provided here since it is the basis for the post-processing work. Appendix A contains the T^*_ε calculation program that is written, based on this mathematical approach.

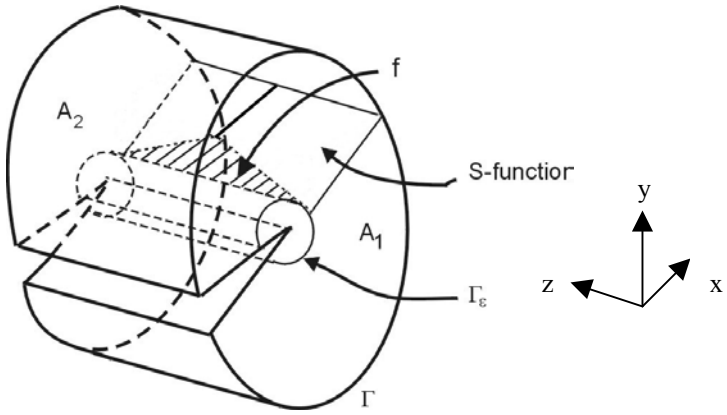

Figure 3.20: 3-D EDI formulation.

The 2-D *EDI* formulation for T^*_ε is generalized to a 3-D formulation by considering a volume analog to the 2-D area between the inner Γ_ε contour, and the far-field Γ contour. Figure 3.20 is a representation of the *EDI* region and the *s*-function for 3-D calculation. Here, the bounding contours are generalized to tubes encircling the crack tip. The *s*-function, which is an arbitrary function of *x*, and *y* in two dimensions now becomes an arbitrary function of *x*, *y*, and *z*. To remove this dependency on the out of plane coordinate, an *s*-function could be chosen such that it is always equal to 1 on the inner contour and 0 on the outer contour, regardless of position through the thickness. However, the surface area portions (A_1, and A_2) on the ends of the annular *EDI* region must then be included in the integration.

After application of the divergence theorem the T^*_ε for this *EDI* formulation and *s*-function and a crack undergoing self-similar propagation is;

$$T_{1\varepsilon}^{*} = -\iiint_{\Gamma_\varepsilon} \left\{ \frac{\partial}{\partial x_1}(Ws) - \frac{\partial}{\partial x_j}\left(\sigma_{ij} \frac{\partial u_i}{\partial x_1} s \right) \right\} dV + \iint_A \left(W n_1 - \sigma_{ij} \frac{\partial u_i}{\partial x_1} n_j \right) s dA \qquad (3.2)$$

where the area term represents the surface areas at the end of the annular region. For convenience, and after application of the chain rule of calculus, the integral may be separated into terms as;

$$T_{1\varepsilon}^{*}(s) = -\iiint_{\Gamma_\varepsilon} \left\{ W \frac{\partial s}{\partial x_1} - \sigma_{ij} \frac{\partial u_i}{\partial x_1} \frac{\partial s}{\partial x_j} \right\} dV \qquad (3.3)$$

$$T_{1\varepsilon}^{*}(W) = -\iiint_{\Gamma_\varepsilon} \left\{ \frac{\partial W}{\partial x_1} - \frac{\partial \sigma_{ij}}{\partial x_j} \frac{\partial u_i}{\partial x_1} - \sigma_{ij} \frac{\partial}{\partial x_j} \frac{\partial u_i}{\partial x_1} \right\} s dV \qquad (3.4)$$

$$T_{1\varepsilon}^{*}(A) = -\iint_A \sigma_{i3} \frac{\partial u_i}{\partial x_1} n_3 s dA \qquad (3.5)$$

$$T_{1\varepsilon}^{*} = T_{1\varepsilon}^{*}(s) + T_{1\varepsilon}^{*}(W) + T_{1\varepsilon}^{*}(A) \qquad (3.6)$$

Here, the area term ($T^{*}_{1\varepsilon}(A)$) has been simplified by noting that if the ends are assumed to be perpendicular to the volume, and the normals, $n_1=n_2=0$, $n_3=1$ on A_1 and $n_3=-1$ on A_2. For equilibrium, and in the absence of body forces, the middle term in Eq. 3.4 is zero so $T^{*}(W)$ becomes:

$$T_{1\varepsilon}^{*}(W) = -\iiint_{\Gamma_\varepsilon} \left\{ \frac{\partial W}{\partial x_1} - \sigma_{ij} \frac{\partial}{\partial x_j} \frac{\partial u_i}{\partial x_1} \right\} s dV \qquad (3.7)$$

The integration in Eq. 3.3 is carried out by utilizing 2x2x2 gaussian quadrature for a numerical estimation. Values of nodal displacement are easily obtained from ABAQUS via a Fortran post-processing subroutine, and the *s*-function is assigned based on each particular node within the EDI region. Stress work density, and stress are also extracted from ABAQUS, but are then averaged over each element in the integration since these

variables are not involved in a direct integration, and precise local values are unnecessary. With an isoparametric mapping, Eq. 3.3 for each element becomes;

$$T_1^*(s) = -\int_{-1}^{1}\int_{-1}^{1}\int_{-1}^{1}\left\{W\frac{\partial N^k}{\partial x_1}s^k - \sigma_{ij}\frac{\partial N^m}{\partial x_1}\frac{\partial N^k}{\partial x_j}u_i^m s^k\right\}\det(J)\,d\xi\,d\eta\,d\zeta \tag{3.8}$$

where J is the Jacobian matrix, and $N^k(\xi,\eta,\zeta)$ are the isoparametric shape functions. With 2x2x2 gaussian quadrature, Eq. 3.8 is now calculated with a simple summation as;

$$T_1^*(s) = -\sum_{1}^{n}\sum_{\xi=1}^{2}\sum_{\eta=1}^{2}\sum_{\zeta=1}^{2}\left(W\frac{\partial N^k}{\partial x_1}s^k - \sigma_{ij}\frac{\partial N^m}{\partial x_1}\frac{\partial N^k}{\partial x_j}u_i^m s^k\right)w^G w^G w^G \det(J) \tag{3.9}$$

where the calculation is performed over n elements in the EDI region, and w^G are the gaussian quadrature weights ($w^G = 1$ for 2x2x2 integration).

Values of stress, strain and work density are only available at gaussian points after a numerical analysis. The mathematical development underlying the coding structure of the post-processing program is such that values of all parameters are required at node points. Specifically, the complication with Eq. 3.7 arises from the fact that in this portion of the calculation, in contrast with the calculation of Eq. 3.3, local gradients of these values are required. Therefore, an extrapolation of gaussian point values to nodal values must be performed, followed by a one point integration at the center of each element, as shown in [86]. A method for locally smoothing stresses (or strains) obtained from isoparametric elements is outlined by Hinton, et al [96], and provides a means for obtaining nodal values by 'averaging' out the gaussian values. A trilinear variation of stresses or strains is assumed to occur in a three-dimensional element as

$$\tilde{\sigma}(\xi,\eta,\zeta)=\left[1,\xi,\eta,\zeta,\xi\eta,\xi\zeta,\eta\zeta,\xi\eta\zeta\right]\begin{Bmatrix}a_1\\a_2\\a_3\\a_4\\a_5\\a_6\\a_7\\a_8\end{Bmatrix} \tag{3.10}$$

$$\tilde{\sigma}(\xi,\eta,\zeta)=[\mathrm{p}]\{a\}$$

where $\tilde{\sigma}(\xi,\eta,\zeta)$ are the variables anywhere within the element, and ξ,η,ζ are the isoparametric mapping coordinates such that at the gaussian quadrature points,

$$[\mathrm{p}]=\begin{bmatrix}
1 & -\frac{1}{\sqrt{3}} & -\frac{1}{\sqrt{3}} & -\frac{1}{\sqrt{3}} & \frac{1}{3} & \frac{1}{3} & \frac{1}{3} & -\frac{1}{3\sqrt{3}}\\
1 & \frac{1}{\sqrt{3}} & -\frac{1}{\sqrt{3}} & -\frac{1}{\sqrt{3}} & -\frac{1}{3} & -\frac{1}{3} & \frac{1}{3} & \frac{1}{3\sqrt{3}}\\
1 & \frac{1}{\sqrt{3}} & \frac{1}{\sqrt{3}} & -\frac{1}{\sqrt{3}} & \frac{1}{3} & -\frac{1}{3} & -\frac{1}{3} & -\frac{1}{3\sqrt{3}}\\
1 & -\frac{1}{\sqrt{3}} & \frac{1}{\sqrt{3}} & -\frac{1}{\sqrt{3}} & -\frac{1}{3} & \frac{1}{3} & -\frac{1}{3} & \frac{1}{3\sqrt{3}}\\
1 & -\frac{1}{\sqrt{3}} & -\frac{1}{\sqrt{3}} & \frac{1}{\sqrt{3}} & \frac{1}{3} & -\frac{1}{3} & -\frac{1}{3} & \frac{1}{3\sqrt{3}}\\
1 & \frac{1}{\sqrt{3}} & -\frac{1}{\sqrt{3}} & \frac{1}{\sqrt{3}} & -\frac{1}{3} & \frac{1}{3} & -\frac{1}{3} & -\frac{1}{3\sqrt{3}}\\
1 & \frac{1}{\sqrt{3}} & \frac{1}{\sqrt{3}} & \frac{1}{\sqrt{3}} & \frac{1}{3} & \frac{1}{3} & \frac{1}{3} & \frac{1}{3\sqrt{3}}\\
1 & -\frac{1}{\sqrt{3}} & \frac{1}{\sqrt{3}} & \frac{1}{\sqrt{3}} & -\frac{1}{3} & -\frac{1}{3} & \frac{1}{3} & -\frac{1}{3\sqrt{3}}
\end{bmatrix} \tag{3.11}$$

At the node points, a similar relationship holds, i.e.

$$\{\sigma\} = [\mathrm{P}]\{a\}$$
$$\text{so that,} \tag{3.12}$$
$$\{a\} = [\mathrm{P}]^{-1}\{\sigma\}$$

where,

$$[\mathrm{P}] = \begin{bmatrix} 1 & -1 & -1 & -1 & 1 & 1 & 1 & 1 \\ 1 & 1 & -1 & -1 & -1 & -1 & 1 & 1 \\ 1 & 1 & 1 & -1 & 1 & -1 & -1 & -1 \\ 1 & -1 & 1 & -1 & -1 & 1 & -1 & 1 \\ 1 & -1 & -1 & 1 & 1 & -1 & -1 & 1 \\ 1 & 1 & -1 & 1 & -1 & 1 & -1 & -1 \\ 1 & 1 & 1 & 1 & 1 & 1 & 1 & 1 \\ 1 & -1 & 1 & 1 & -1 & -1 & 1 & -1 \end{bmatrix} \tag{3.13}$$

Now, the nodal values of stresses, extrapolated from the gaussian values are expressed as follows;

$$\{\tilde{\sigma}\} = [\mathrm{p}][\mathrm{P}]^{-1}\{\sigma\} \tag{3.14}$$

So that nodal values of stress and strain may easily be obtained from the reported gaussian point values. These extrapolated values are then inserted into Eq. 3.7 and the integration is performed using gaussian quadrature as in Eq. 3.9.

The third portion of the numerical integration would involve the calculation of the area terms at the ends of the *EDI* volume (Eq. 3.5) if this *s*-function formulation were desired. This calculation would require a 2x2 gaussian quadrature of the end areas, A_1 and A_2 in Figure 3.21, and would make use of the simplifications noted earlier.

CHAPTER 4: RESULTS AND DISCUSSION

4.1 EXPERIMENTAL RESULTS

4.1.1 STABLE CRACK PROPAGATION ANALYSIS

A total of six 3-point bend specimens (Table 3) were ramp loaded to obtain different amounts of stable crack propagation, varying between 0.5 and 5.5 mm. Following the monotonic loading, each specimen was subjected to post-fatigue crack propagation to mark the extent of tunneling at each level. This post fatigue cracking was a very delicate operation whereby the specimens were cycled at a load ratio of R=0.1 to a maximum of sixty percent of the final load that each withstood under monotonic loading. Since the crack extension behavior is somewhat difficult to control, only four of these tests yielded usable results. Images of these four tunneling profiles are shown in Figure 4.1.

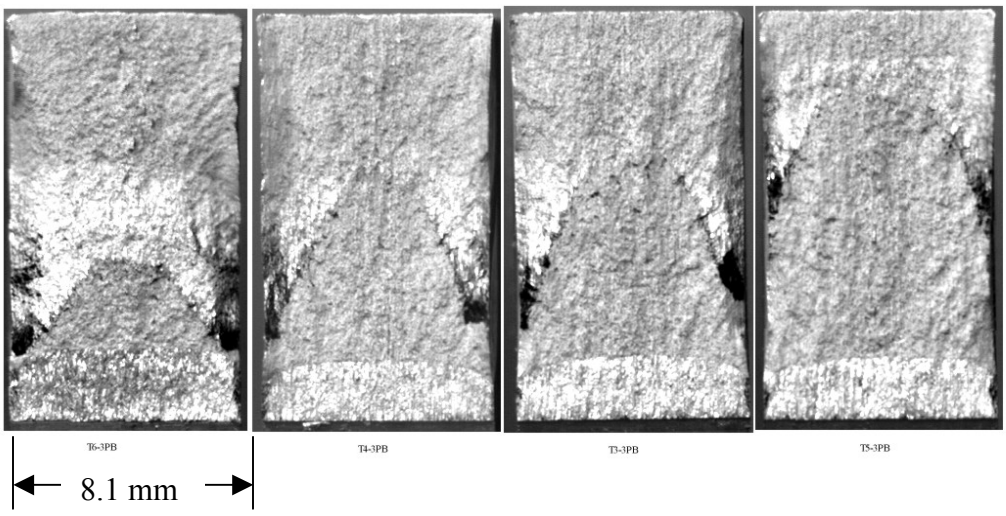

Figure 4.1: Progression of tunneling crack between 0.5 mm and 5.5 mm.

Each of these images was calibrated to known dimensions, and the pre-crack and tunneling crack front profiles were digitized using Sigma Scan software. The digitized crack fronts were then fit to polynomials of varying orders from 4^{th} order to 6^{th} order depending on their level of complexity. The polynomial curve fit served to fill in sparse data at regular (0.25 mm) increments through the thickness (z) direction and to provide a means for calculating local crack front tangents via differentiation for use with the numerical analysis. Since the amount of stable crack propagation is difficult to control in an experimental environment, tunneling profiles at very sparse points were obtained. To address this sparseness of data without performing what could amount to hundreds of tests, the specimens were intentionally loaded to obtain these discrete crack extension levels to show the progression of tunneling. Following the collection of these discrete data points, a linear interpolation scheme was written using Matlab to guess at what intermediate tunneling profiles would look like and to increase the data resolution by two times. This interpolation is repeated for the profiles between experimentally obtained crack fronts at Δa=3.5 mm (T3-3PB) and Δa=5.5 mm (T5-3PB) so that this data resolution is actually increased twice to roughly three times the initial number of data points. Figure 4.2 shows the interpolated crack fronts obtained after the initial interpolation, Figure 4.3 shows the interpolated crack fronts after the second interpolation, and Figure 4.4 is a comparison of the raw, digitized data to the polynomial fit data.

Although a fairly insignificant specimen shear lip was expected, and observed in this thick specimen configuration, it is worth noting its value. For this specimen configuration, a shear lip of approximately 0.5 mm per side was measured. This amounts to total a shear lip of 1.0 mm, or 13% of the specimen thickness.

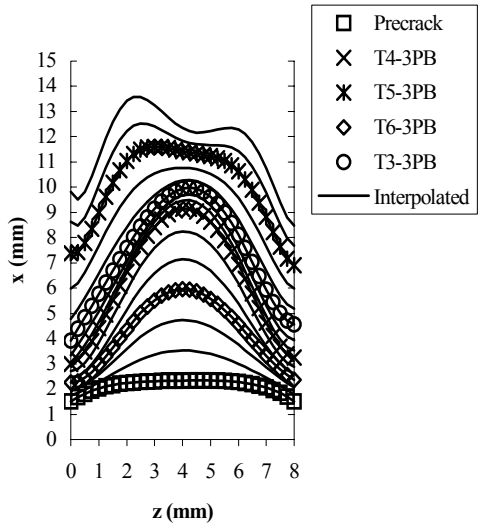

Figure 4.2: Interpolated crack front tunneling profiles.

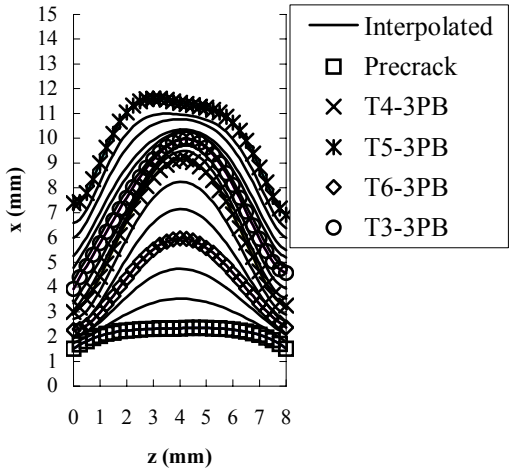

Figure 4.3: Crack fronts after second interpolation.

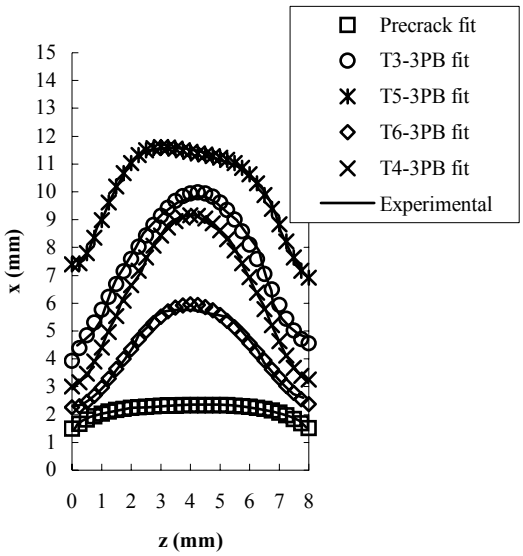

Figure 4.4: Polynomial curve fits compared to raw data.

After approximately 2.0 mm of surface crack extension, the crack is observed to propagate in a relatively self-similar manner. After several levels of crack extension however, the near mid-plane crack front flattens as it approaches the externally applied mid-span load. This will affect the tunneling as well as the numerical analysis of these crack fronts.

4.1.2 EXPERIMENTAL T^*_ε RESULTS

Results from the experimental work include moiré fringe patterns for each crack extension step as measured at the surface of the specimen. The moiré fringe patterns provide a full-field map of displacements that can be used to calculate the localized strain, and then the stress via Hencky's total stress-strain relationship, which is given as [104];

$$\varepsilon_{ij}^{p} = \frac{3}{2}\frac{S_{ij}}{\sigma_e}\varepsilon^{p} \tag{4.1}$$

where ε_{ij}^{p} is the current state of plastic strain, σ_e is the equivalent stress (or yield stress in this case), ε^{p} is the yield strain, and S_{ij} is the stress deviator tensor. T^*_{ε} is calculated by utilizing Okada's [70] approach with a truncated contour as described in Chapter 1. The deformation theory of plasticity is also used here since the truncated contour encompasses the area in front of the crack tip, which has not yet undergone extensive unloading. This allows the calculation of T^*_{ε}, without the inclusion of strain history, for each crack extension step in the experimental analysis.

Figure 4.5 shows the T^*_{ε} calculated for test "T5-3PB" in which the surface crack was extended to 5.5 millimeters. Here, T^*_{ε} was calculated on three different contour sizes of ε = 1.0, 2.0 mm and 3.0 mm. Figure 4.6 shows calculated T^*_{ε} for two other test cases, "T3-3PB", and "T4-3PB" where the crack was extended to shorter lengths. The results for "T5-3PB" are of particular interest because here the crack was extended to the longest possible length in this specimen configuration. This data set will be used for comparison with the numerical analysis results. The T^*_{ε} curve in Figure 4.5 shows a peak values of approximately 157 MPa-mm (for ε = 2.0 mm) and 125 Mpa-mm (for ε = 1.0 mm), which compares well, quantitatively, with the experimentally obtained results of Ma [92] (Figure 1.9) who obtained experimental T^*_{ε} in plane stress, center notched (CN) samples of 2024-T3 aluminum alloy. It is noted that the results for the Γ_{ε} contour size of ε = 1.0 mm are somewhat of an estimation because the displacement field cannot actually be viewed this close to the crack tip due to the gross deformation and consequent dimpling effect at the crack tip. The displacement field this close to the crack tip is based on an extrapolation of the moiré fringes to the crack face, resulting from the curvature of each fringe as it enters the high deformation zone. As a result, the T^*_{ε} calculated on this contour can show significant noise due to the approximated strain gradients in this area.

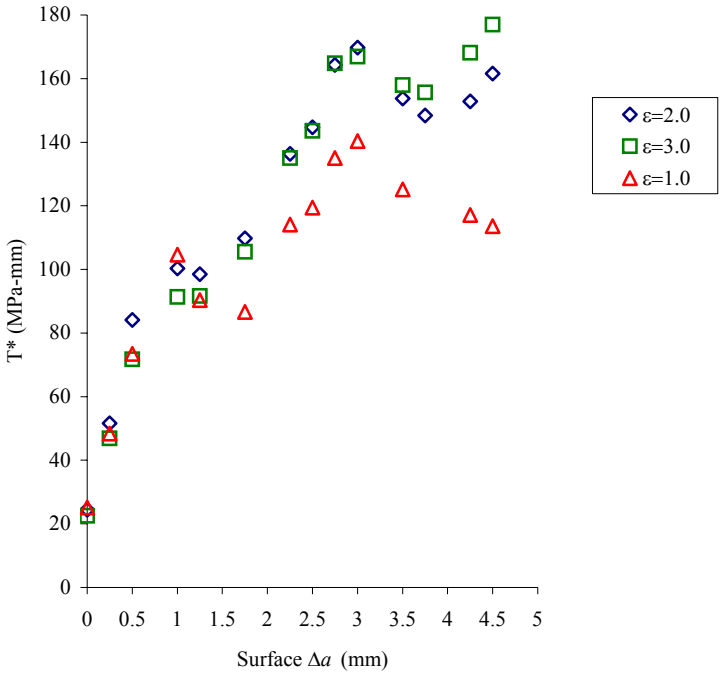

Figure 4.5: Experimental T^*_ε for different contours, T5-3PB

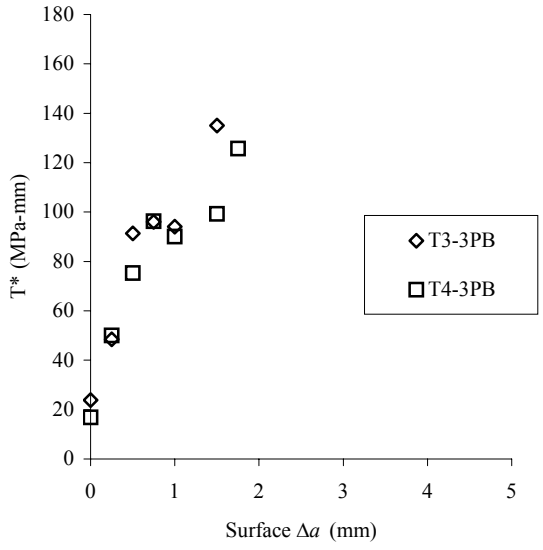

Figure 4.6: Experimental T^*_ε for two other experiments, ε=3.0 mm.

4.1.3 EXPERIMENTAL CTOA RESULTS

The *CTOA* was calculated on the surface of the three specimens T3-3PB, T4-3PB, and T5-3PB. The *CTOA* calculation consisted of extracting the *v*-displacement at approximately 1.0 mm behind the current crack tip, obtaining the inverse tangent, and multiplying by 2.0 (symmetry). Figure 4.7 is a plot of the resulting *CTOA* plots for these three experiments.

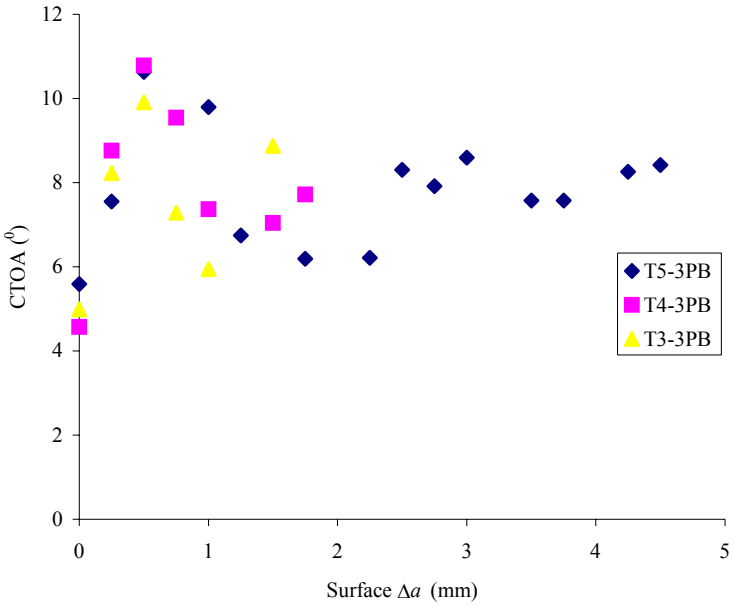

Figure 4.7: Surface CTOA from experimental measurements.

4.2 NUMERICAL ANALYSIS PRELIMINARIES

4.2.1 DETERMINATION OF Γ_ε CONTOUR SIZE

To avoid numerical difficulties and to ensure a valid comparison between experimental T^*_ε values obtained at the surface of the specimen, and the numerically obtained through-thickness values, a similar size contour must be used for both analyses. This contour

should be such that an assumption of near 2-D behavior can be made if this comparison is to be drawn. An examination of the out-of-plane strains (ε_{33}) directly in front of the crack tip shows that after a short amount of crack extension, the level of out-of-plane strain becomes constant at a specific distance ahead of the crack tip. Figures 4.8 and 4.9 show the extent of out-of-plane strain (with respect to the *x-y* plane) through the thickness of the numerical model at different distances, *r*, from the crack tip for crack extensions of $\Delta a = 0.0$ *mm*, and $\Delta a = 0.75$ *mm*, respectively. This attainment of a constant value of ε_{33} is indicative of a transition to a plane strain state at a distance from the crack tip corresponding to this value of *r*. Since there is now a level of constancy through the thickness, this distance can be used as the inner, Γ_ε contour size, ε. For a short amount of crack extension (0.75 mm), it is seen that this transition begins to occur at a distance of approximately 2 mm and that out of plane strain becomes essentially constant and very close to zero between 2 and 3 mm from the crack tip. Figure 4.9 shows strain behavior after several crack extension steps. Here, it is seen that the distance for plane strain transition increases to between 3 and 4 mm from the crack tip. The paper by Narisimhan and Rosakis [66] discussed a correlation between specimen thickness and distance to this plane state transition for plane stress specimens. It was found that the distance to the transition point was roughly equivalent to half the specimen thickness in correlation with what is seen here in Figures 4.8 and 4.9 for the near surface, plane stress portions.

The extent of tunneling seen in this analysis leads to numerical difficulties with regard to explicitly prescribing the aforementioned transition point as the exact location of the inner, Γ_ε integration contour. A preliminary inspection of the behavior of the T^*_ε integral through the thickness of the specimen after a few crack extensions revealed sensitivity of the analysis to the location of the integration contour. After a short amount of crack propagation, the expected path dependency of the T^*_ε integral becomes very evident. For contour sizes of 1.0, 2.0 mm, and 3.0 mm, the behavior of the local crack tip integral can change by 10-20%. There is also a slight dependence of T^*_ε integral on the size of the *EDI* region. Since the T^*_ε calculation should be independent of *EDI* size, this

dependence is indicative of numerical errors due to loss of stress and strain data as the crack tip is approached and extreme plasticity is present or, possibly boundary effects if a large enough contour is used. It is also indicative of a loss of resolution since the *s*-function is assigned at node points, based on their location within the EDI boundaries. Fewer node points through the width of the EDI region will obviously adversely affect the accuracy of the calculation. As an example, if the extreme cases of either only one element through the EDI region width or, say four elements through the EDI region width are considered, it is easy to see that the former case will utilize *s*-function values of 1 and 0, whereas the latter would have *s*-functions of 1, 0.75, 0.5, 0.25, and 0 as the EDI region is traversed. Thus, very small, or very large contour sizes should be avoided due to the numerical inaccuracies and a reasonable number of elements through the EDI region should be assigned.

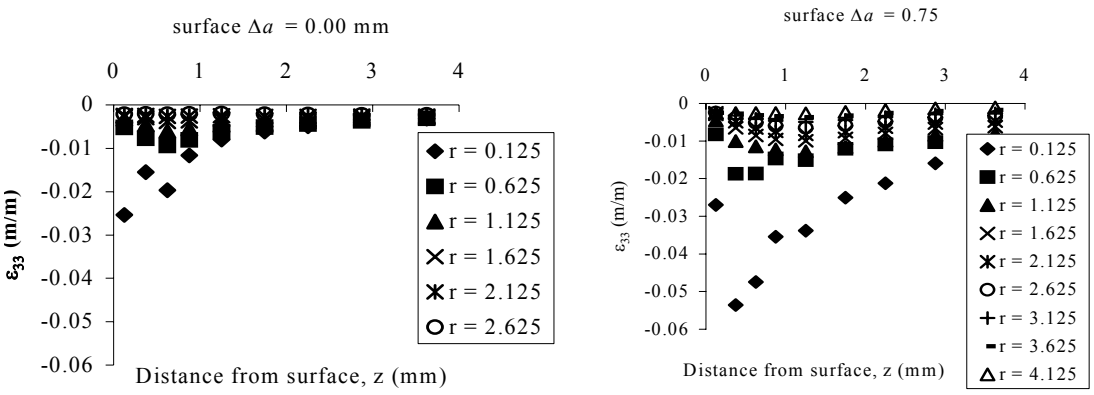

Figure 4.8: Out of plane strain levels in the x-y plane shortly after crack initiation.

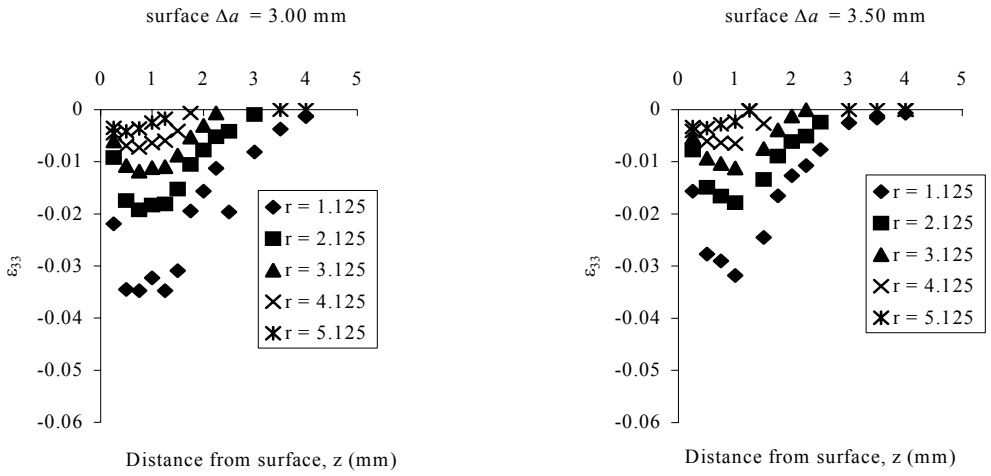

Figure 4.9: Out of plane strain levels in the x-y plane after several crack extensions.

Since the crack is modeled with extreme tunneling, the contour will also have to adapt with the changing crack front. The contour grows with the extending crack front, that is, the portion behind the original crack tip remains fixed throughout the analysis. This means the contour will actually be larger for layers near the mid-plane than those at the surface. Figure 4.10 shows how this is accommodated in this analysis. Here, the blue highlighted elements represent the EDI region, and the red circles indicate nodes in the remaining ligament.

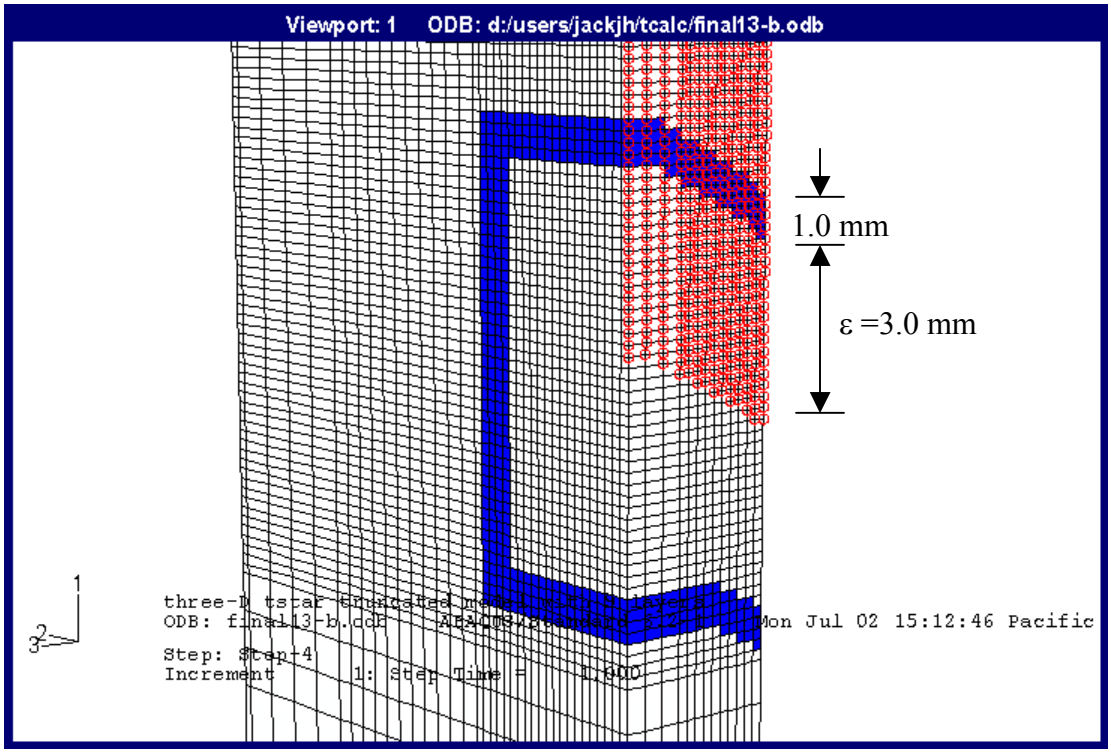

Figure 4.10: EDI definition for T^*_ε calculation with extending, tunneling contour.

4.1.2 CHOICE OF S-FUNCTION

The EDI formulation is a variation of the VCE method wherein an arbitrary function is applied in place of the virtual displacements. This arbitrary function, referred to as the *s*-function by Nikishkov and Atluri [86], takes on a new level of complexity for 3-D situations. For 2-D, it has been applied as a simple ramp function that is equal to 1 on the near field, Γ_ε contour, and 0 on a far field contour. Several types of 3-D *s*-functions are reviewed in [86], of which only a few are eligible for use in this research. Since the numerical model used in this study employs linear elements, and a fairly course resolution through the thickness, candidate *s*-functions will include a triangular *s*-function, and a linear *s*-function (Figure 4.11). Upon initial inspection, it would seem that the linear *s*-function would be appealing from a programming standpoint. However,

the areas on the two ends of the current layer of calculation must be included in this case. The triangular *s*-function, on the other hand, allows a major simplification since the value of the *s*-function in this case is equal to zero at the end of the EDI region. The difficulty with the triangular *s*-function then becomes the lack of resolution through the thickness due to the fact that it must be calculated over at least two element layers for 8 node, linear elements. This difficulty is easily overcome by employing a calculation scheme as depicted in Figure 4.12, where two iterations of calculation are performed, each offset by one node with respect to the other. The final result is a capability for calculating the contour integral at each layer interface with the exception of the surface node layer, and the mid-plane node layer. This does not prove to be a major problem as the resolution of the model allows calculation very close to these two points.

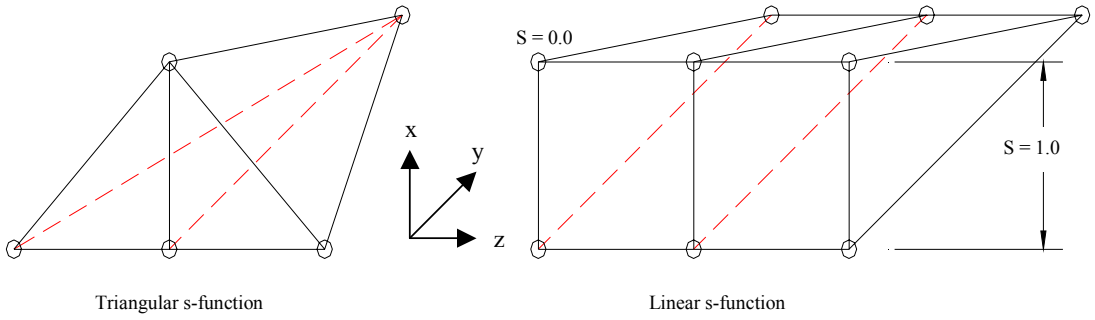

Figure 4.11: S-functions for EDI calculation.

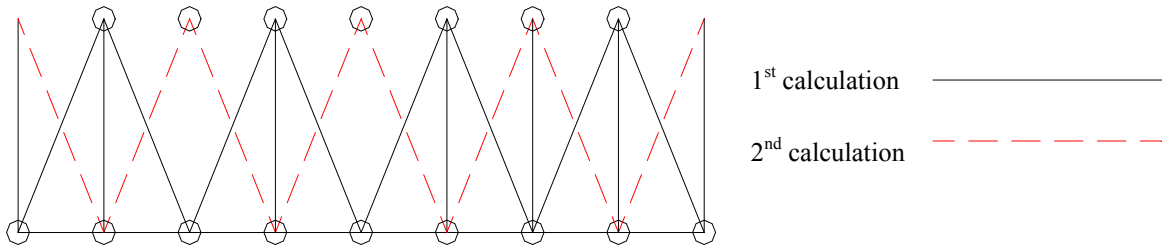

Figure 4.12: Integration scheme for high calculation resolution.

4.2.3 CRACK FRONT COORDINATE TRANSFORMATION

To accommodate the tunneling crack front, which is continually turning with respect to the thickness, the global variables are normally transformed with respect to the crack front coordinate system to "straighten" the crack front. This becomes more and more of an issue as the inner contour of integration is collapsed onto the crack tip. The coordinate transformation simply involves calculating local tangents to the crack front and transforming stresses, strains, work densities, displacements, and coordinates to the crack front coordinate system. These transformations from global to local coordinates are applied in the x-z plane (plane of the crack) and are simply:

$$\begin{aligned} x_i &= a_{ij} x_i^G \\ s_{ij} &= a_{ip} a_{jq} s_{pq}^G \end{aligned} \tag{4.2}$$

for vectors, and tensors respectively. However, as the inner contour of integration is moved further away from the crack tip, the transformation of global variables to the crack front coordinate system becomes less reasonable. Instead, a rotation of the entire EDI region with respect to the global coordinate system is likely required in addition to the transformation of global variables. This is an extremely complex operation that would require a very refined, radial mesh surrounding the current crack tip. The mesh would also need to adapt intelligently as the crack tip moves. Figure 4.13 is a representation of the effect of transforming the variables within the EDI region and of transforming the EDI variables in addition to a rotation of the entire EDI region with respect to the crack front. Since this is not feasible for the current numerical model, T^*_{ε} is estimated without any transformation of the EDI quantities. Regardless of contour size, the integration is performed over elements sufficiently far from the crack front to allow this approximation, especially after several steps of crack extension where the contour has extended far behind the current crack tip. Results from a short analysis with transformed parameters are shown in the numerical results section of this chapter to illustrate the difficulty in calculating this way.

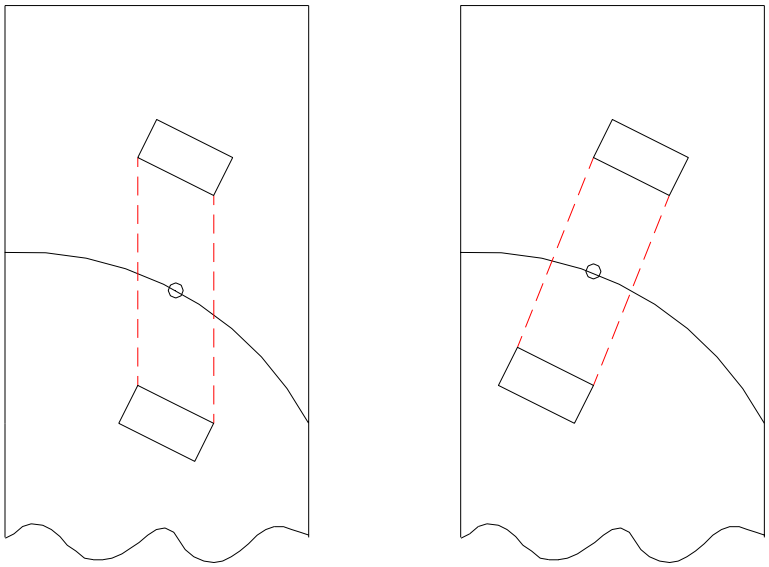

Figure 4.13: Transformation of EDI variables (A) and transformation of EDI variables with rotation (B).

4.3 NUMERICAL RESULTS FOR TUNNELING CRACK

4.3.1 POINT-WISE T^*_ε FOR TUNNELED CRACK

T^*_ε was calculated for each of seventeen, 0.25mm and 0.50 mm crack extension steps, with the extent of experimentally observed tunneling reflected in the crack face boundary conditions at each step. Using a post-processing program written in Matlab (Appendix A), point-wise values were obtained at each layer interface through the thickness of the quarter model to build a plot of behavior for the extending, tunneling crack. Since the integration program utilized the triangular *s*-function, values were unobtainable on the extreme surface, and center plane. The remaining values provide adequate resolution, so this is not a major problem.

Figure 4.14 is shown here merely to illustrate the effect of transforming global variables to the crack front coordinate system. Here, the derivative of the polynomial curve fit at each particular level of crack extension was used as a local slope for determining the degree of transformation. Since the slope may change by 5-10% from one layer to the next, even though the 'mean' slope is identical, very noisy results are produced. As stated before, the global variables for the main analysis are not transformed because of the numerical noise involved.

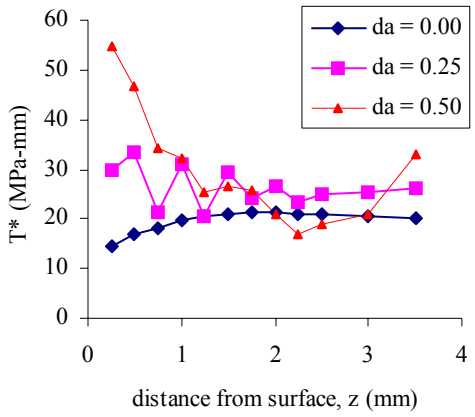

Figure 4.14: Sensitivity of T^*_ε calculation to coordinate transformation, $\varepsilon = 2.0$ mm.

Figures 4.15, 4.16, and 4.17 are plots of numerically obtained, pointwise T^*_ε calculated with inner, Γ_ε contours of $\varepsilon = 3.0$, 2.0, and 1.0 mm respectively for the full extent of crack extension observed in experiment "T5-3PB". Here all values are reported at the corresponding surface crack extension, rather than the local crack extensions. Based on the previous discussion (Section 4.2.1), an inner (Γ_ε) contour size of $\varepsilon = 3.0$ mm and outer (Γ) contour size of 4.0 mm should be used for comparison with experimental values which are based on a plane stress assumption and would be dictated by the observations in [66]. However values for a 2.0 mm contour and a 1.0 mm contour are included here

for completeness and comparison to the previous plane stress analyses of Ma [92]. Regardless of its size, the Γ_ε contour grows with crack extension, but usually remains ε mm from the crack tip in the positive x and y directions (Figure 4.10). Through-thickness (z) trends are shown here for each of the levels of crack extension.

Figures 4.18, 4.19 and 4.20 contain plots of T^*_ε for the extending crack at different points through the thickness (z-direction) and contour sizes of ε = 3.0, 2.0 and 1.0 mm. For these plots, local values of crack extension have been used since these plots would represent local resistance curves. The T^*_ε values increase much more slowly near the mid-plane than on the surface, due to the lack of formation of a significant region of deformation. Since the T^*_ε would be interpreted as a crack driving force in an application phase analysis, it would make sense that there is far less energy required (crack driving force) to extend the crack front near the mid-plane.

Figure 4.20 shows the numerically obtained T^*_ε calculated on a Γ_ε contour of ε = 1.0 mm for local crack extensions. The extreme scatter in these results is due to the extremely close proximity to the crack tip and the active wake zone.

At a surface crack extension of approximately 1.75 mm, the center has tunneled to a crack extension of approximately 8.0 mm and with an inner Γ_ε contour of ε = 3.0 mm begins to suffer from boundary effects from the top load point. If a Γ_ε contour size of ε = 2.0 mm is used, this boundary effect problem becomes evident slightly later at a surface crack extension of 2.25 mm. The boundary effect is an unfortunate side effect from the geometry of this model. The only way to overcome this effect is to begin reducing the size of the integration contour as this point is approached. While this will violate the consistency of the analysis since T^*_ε is a path dependent integral, it will still provide a picture of what is happening at this point. Beginning with the Δa=1.50 mm curve in Figure 4.15, the frontal portion of the Γ_ε contour for layers close to the mid-point is moved closer to the crack tip by anywhere from 0.25 mm to 2.0 mm in the extreme

tunneling cases (Δa = 4.00, and Δa = 5.00 mm). Since this is only a truncation of the frontal portion of the contour, it is thought to have only a small effect on the calculation. Figure 4.21 is an example of an extreme case of frontal truncation where the inner layers have also had a reduction in EDI region width to 0.5 mm.

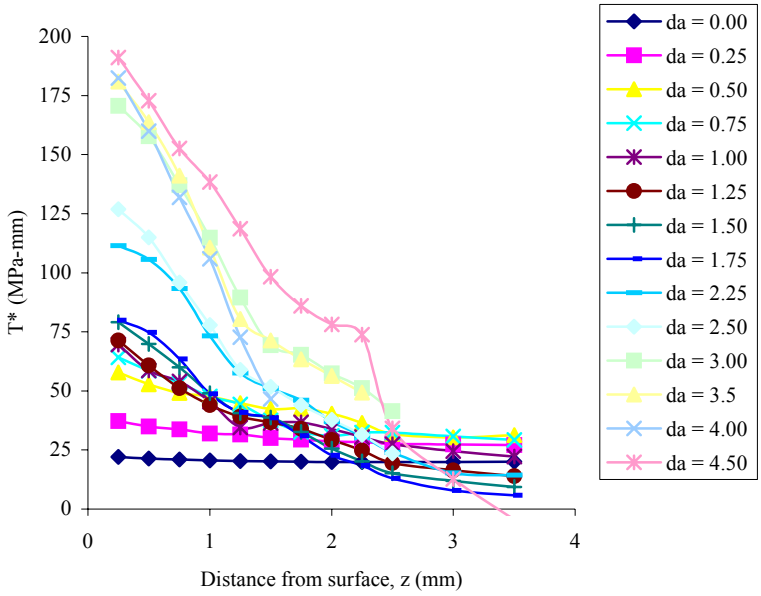

Figure 4.15: FEA T^*_ε variation along tunneled crack front at different levels of surface crack extension, ε = 3.0 mm.

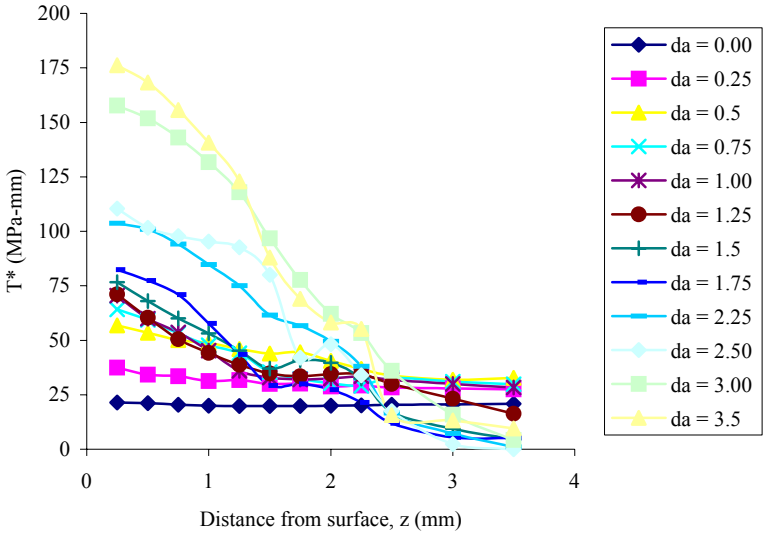

Figure 4.16: FEA T^*_{ε} variation along tunneled crack front at different levels of surface crack extension, ε = 2.0 mm.

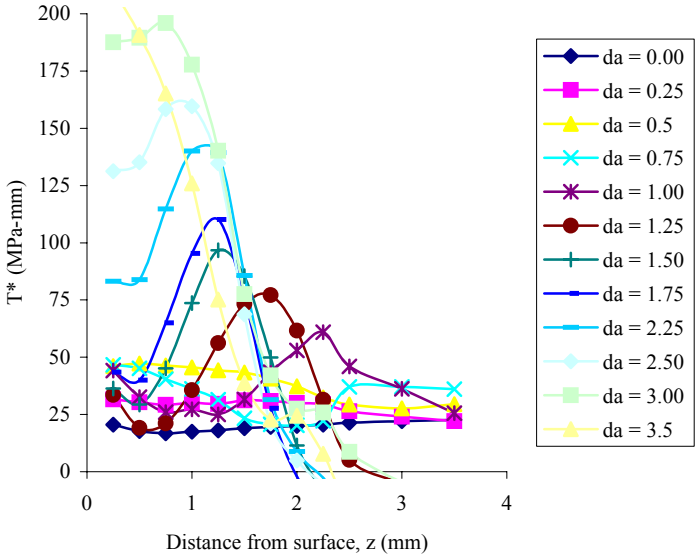

Figure 4.17: FEA T^*_{ε} variation along tunneled crack front at different levels of surface crack extension, ε = 1.0 mm.

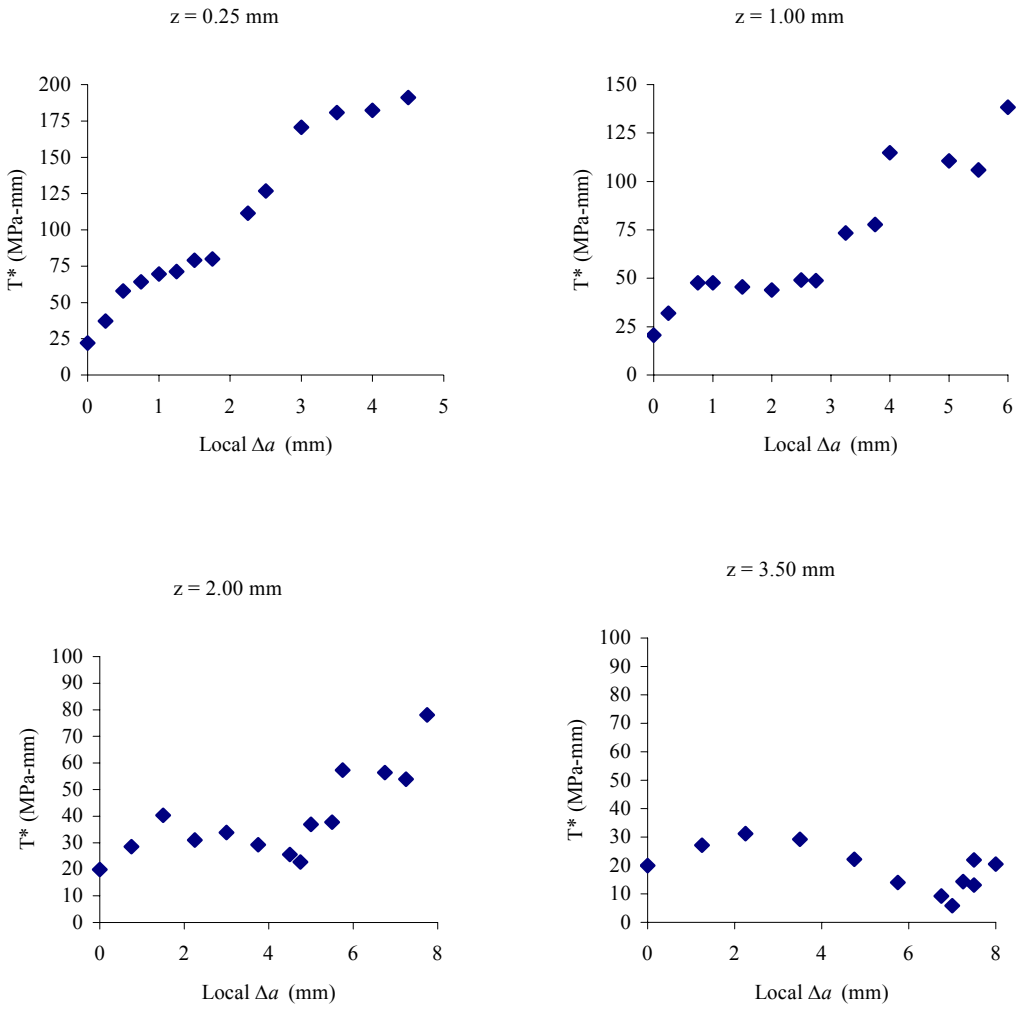

Figure 4.18: T^*_{ε} for different positions along tunneled crack front for local crack extension values, ε = 3.0 mm.

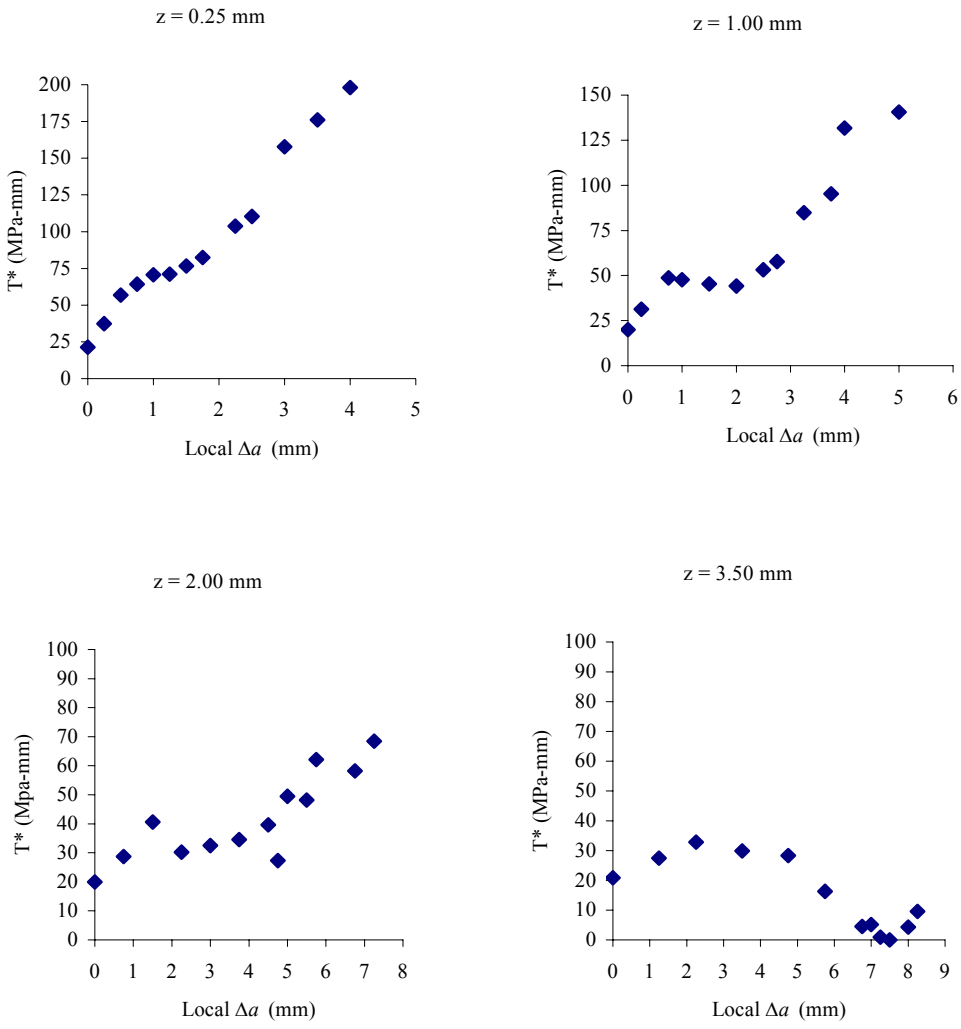

Figure 4.19: T^*_{ε} for different positions along tunneled crack front for local crack extension values, ε = 2.0 mm.

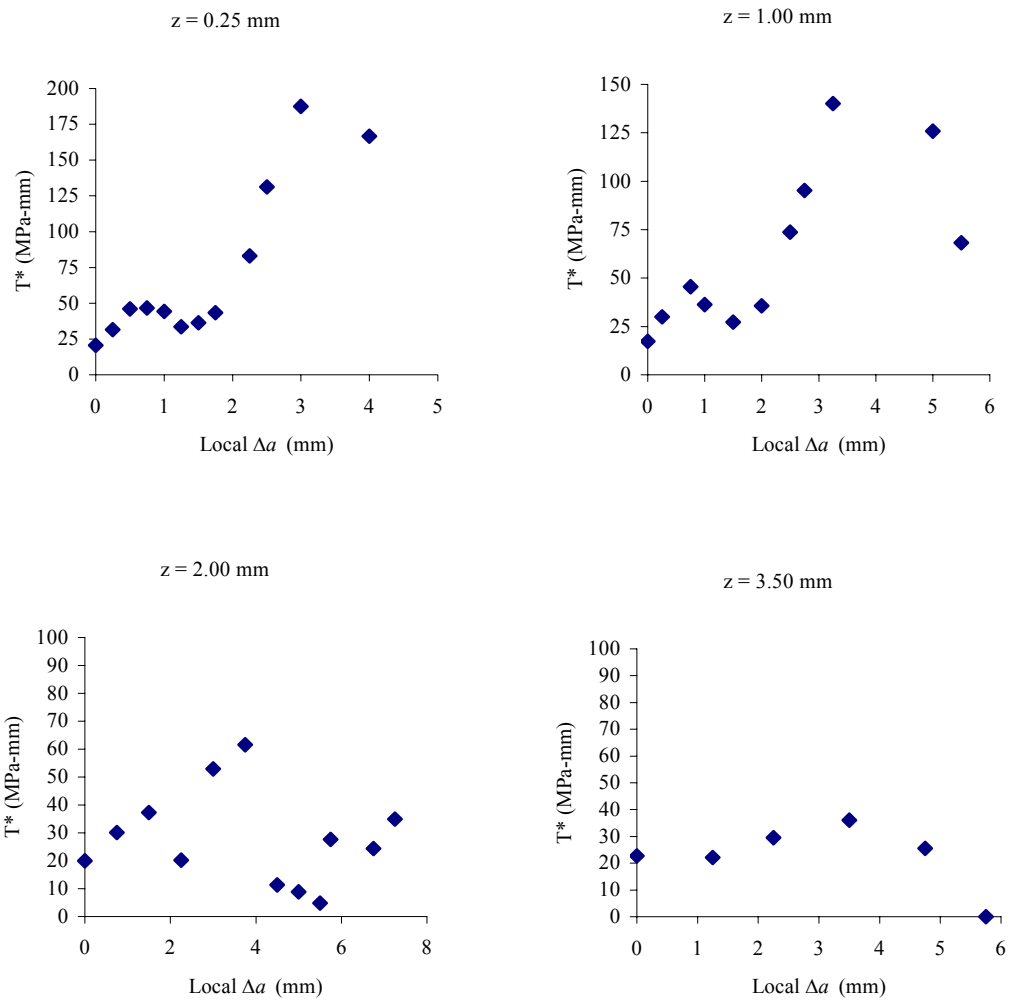

Figure 4.20: T^*_{ε} for different positions along tunneled crack front for local crack extension values, ε = 1.0 mm.

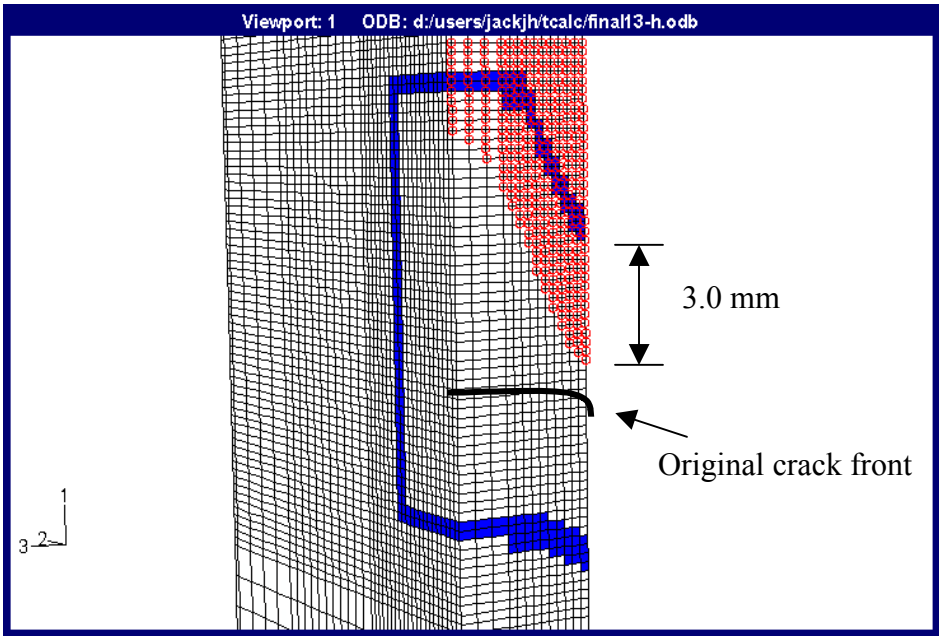

Figure 4.21: Truncation of frontal portion of EDI region after extensive tunneling.

For comparison, T^*_ε was also calculated for the same situations but using Okada's truncated contour approach. This is the same approach that was used to calculate surface values from moiré displacements in the experimental analysis. Nodal displacements were extracted from the FE analysis output at each crack extension step and are easily placed on a local element layer grid of x, and y coordinates for input to the aforementioned Fortran program. Figures 4.22 through 4.24 show point-wise T^*_ε calculated using the deformation theory of plasticity and a truncated contour with FEA produced nodal displacements and based on surface crack extension levels. Figures 4.25 and 4.26 show local T^*_ε resistance curves from this analysis for Γ_ε contour sizes of $\varepsilon = 2.0$ mm and 1.0 mm, respectively.

Figures 4.24, and 4.26 are plots of T^*_ε calculated on an ε = 1.0 mm contour. As previously observed, the data shows a fairly significant amount of scatter due to the close proximity to the crack tip. It is noted that, even at this location, the results show much

less scatter than those calculated using the incremental theory of plasticity and the full, elongating contour.

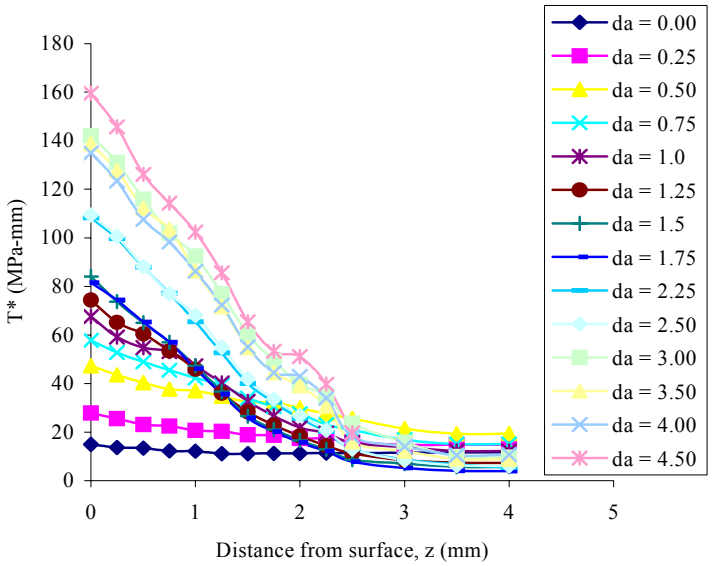

Figure 4.22: FEA T calculated from nodal displacements at different levels of surface crack extension, $\varepsilon = 3.0$ mm.*

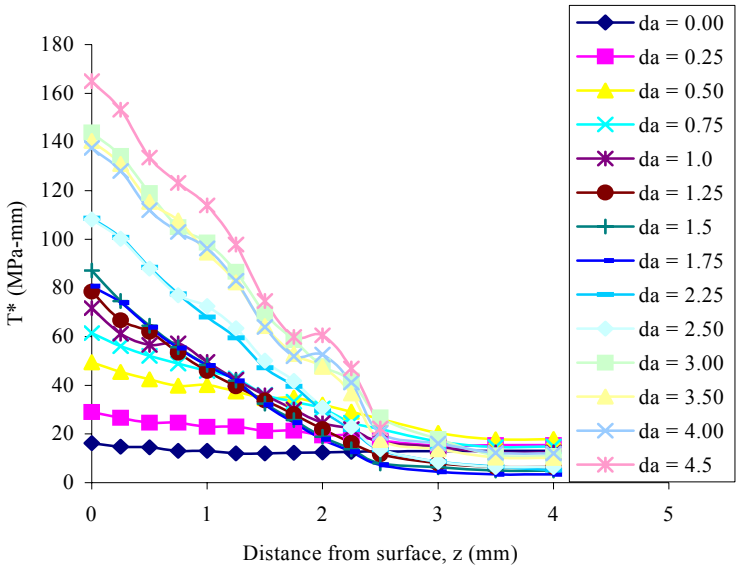

Figure 4.23: FEA T calculated from nodal displacements at different levels of surface crack extension, ε = 2.0 mm.*

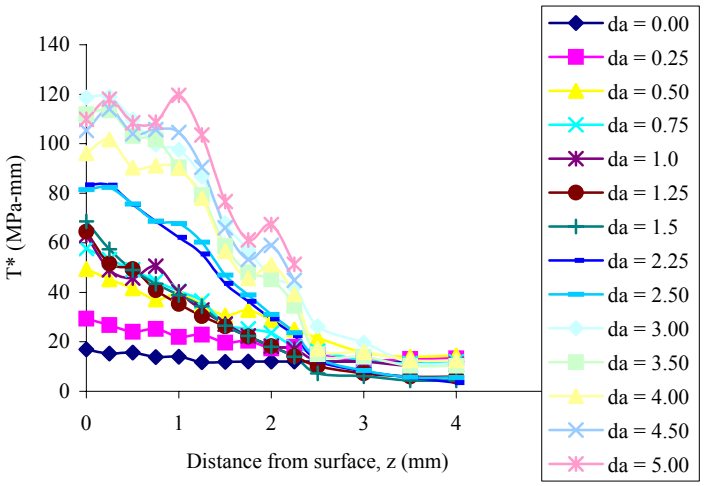

Figure 4.24: FEA T^*_{ε} calculated from nodal displacements at different levels of surface crack extension, ε = 1.0 mm.

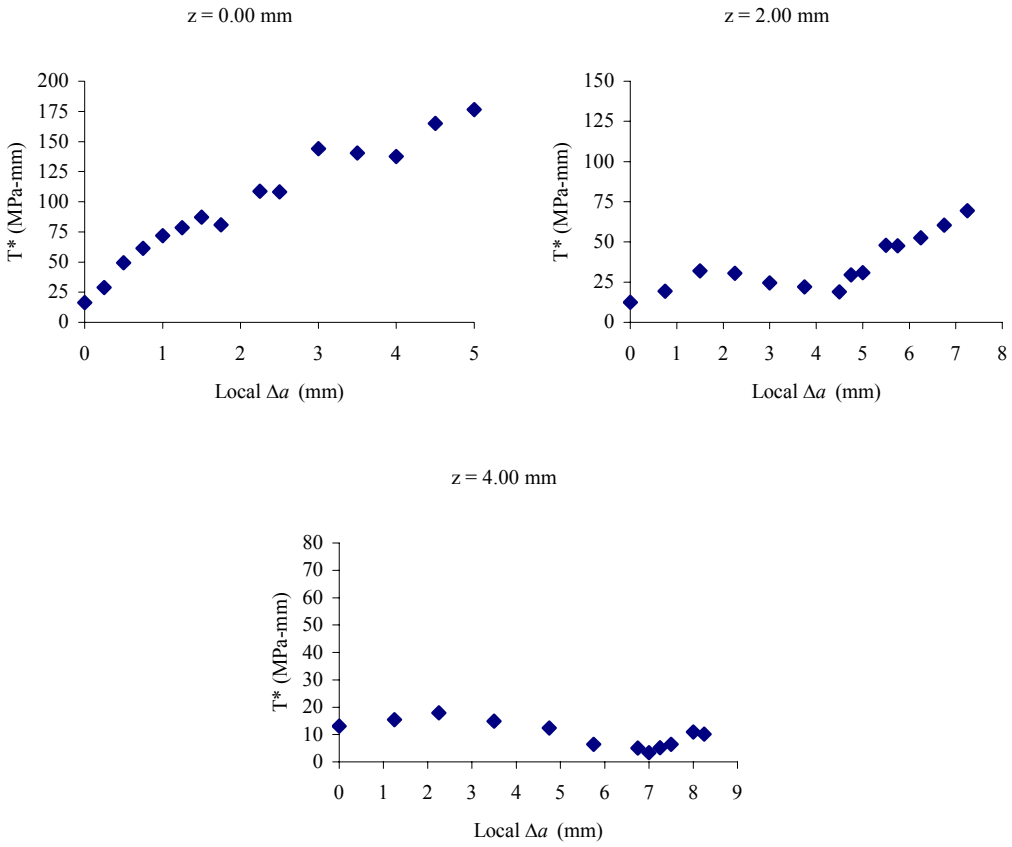

Figure 4.25: FEA T calculated from nodal displacements for local crack extensions, ε = 2.0 mm.*

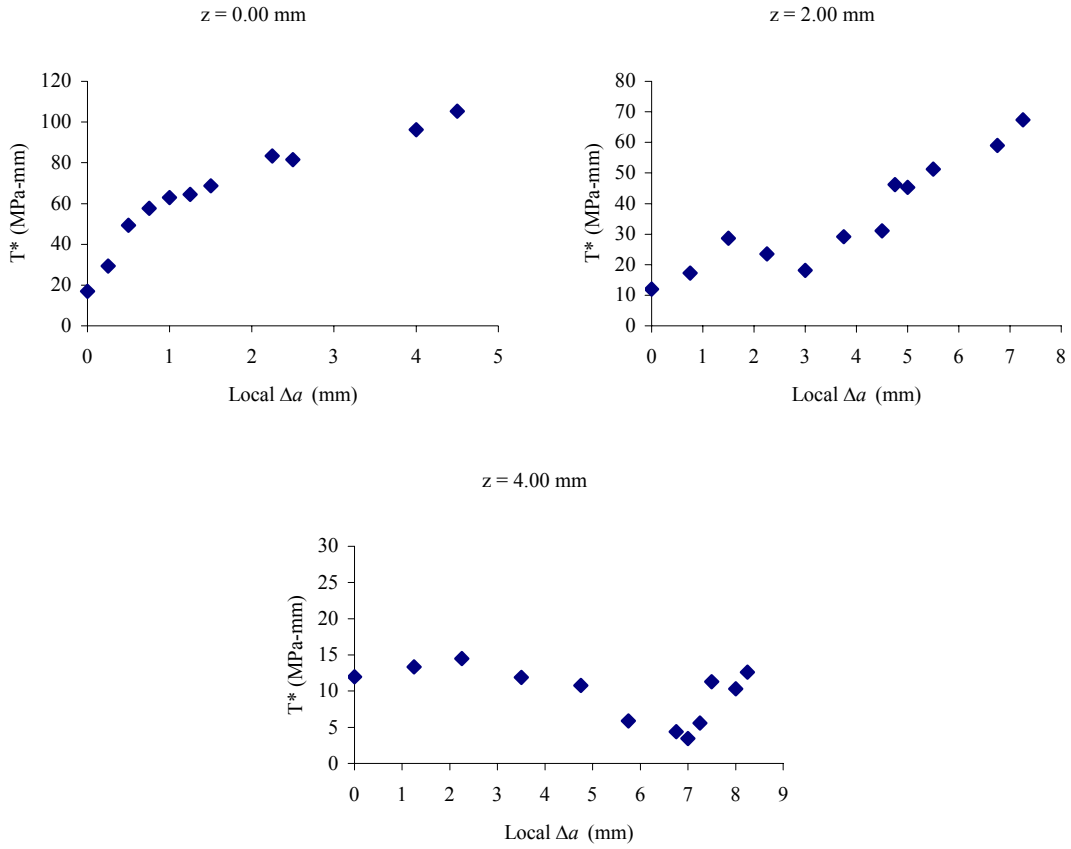

Figure 4.26: FEA T calculated from nodal displacements for local crack extensions, ε = 1.0 mm.*

Figure 4.27 shows the *CTOA* calculated at three locations through the thickness at approximately 1.0 mm behind the crack tip for the surface, the quarter point (midpoint of numerical model), and the specimen mid-point. The surface *CTOA* trend shows the typical sharp increase at the beginning of crack growth, followed by a decline to a fairly steady state value of approximately 7-8 degrees. The quarter point and mid-point trends exhibit an interesting slow rise as the crack extends. This behavior is due to the rapid crack propagation in the center (tunneling) near the beginning of the test, which will produce a small amount of crack tip blunting and hence low *CTOA*. As the tunneling slows, the *CTOA* on the inner layers should increase as seen here due to increasing

amounts of plastic deformation and crack tip blunting. It is observed that the *CTOA* roughly follows the same trend as the near-field T^*_ε calculated on an $\varepsilon = 1.0$ mm contour. Both the *CTOA* and the near-field T^*_ε show a decreasing trend followed by a fairly sharp increase at local crack extensions longer than approximately 6.0 mm.

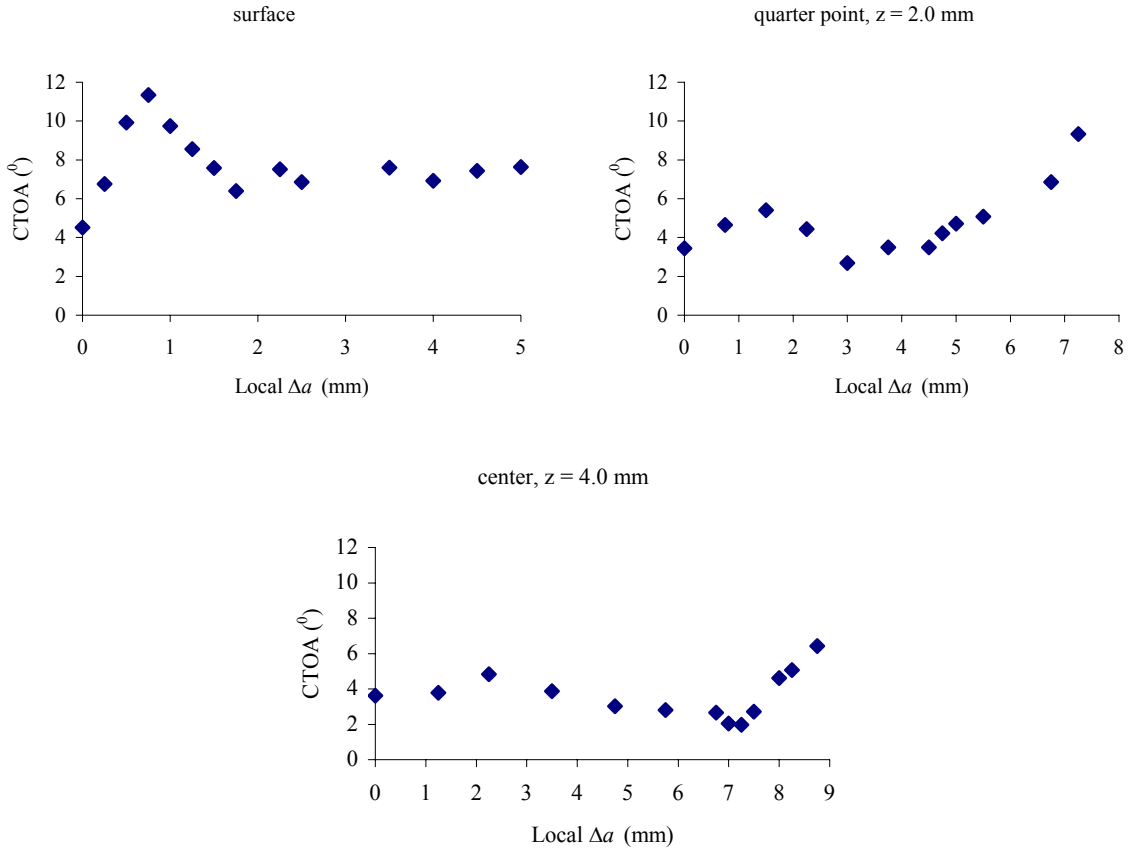

Figure 4.27: CTOA for different through-thickness locations on tunneled crack front.

It should be noted that one of the drawbacks to *CTOA* is its extreme mesh sensitivity. Although this is not extremely evident in Figure 4.27, some of the *CTOA* values are suspect, namely those near the beginning of the analysis. As the crack extension reaches 1.0 mm, the original crack tip blunting causes a bump in *CTOA* value. This blunting

influence decreases as the mid-plane is approached since development of large deformation occurs more slowly here.

4.3.2 POINT-WISE J-INTEGRAL (INCREMENTAL) FOR TUNNELED CRACK

The *J*-integral differs from the T^*_ε integral in two ways. First, the *J*-integral is based on a deformation theory of plasticity and by definition cannot account for unloading, or extensive plasticity. In fact, the *J*-integral is calculated with only the elastic portion of the stress-strain work (strain energy density), whereas the T^*_ε integral is calculated using the summation of elastic strain energy plus the plastic dissipation, which increases incrementally as the crack extends. The second primary difference is that the near field *J*-integral is calculated on a moving contour and, as noted by Okada, et al. [70], is a measure of only the energy release rate at the crack tip. The near field *J*-integral exhibits a peak followed by a drop to nearly zero, which is expected under the aforementioned circumstances.

Figure 4.28 shows the variation of *J*-integral through the thickness, calculated on a moving contour and under an assumption of incremental plasticity. Limitations in the ABAQUS FEA package do not allow *J*-integral to be calculated for the particular geometry used in the present FE model. For ABAQUS *J*-integral, the crack front must be defined on a smooth, continuous crack front. Hence, for this analysis, *J*-integral is calculated with incremental formulation using the same post processing formulation as used for the T^*_ε calculation and with a moving contour.

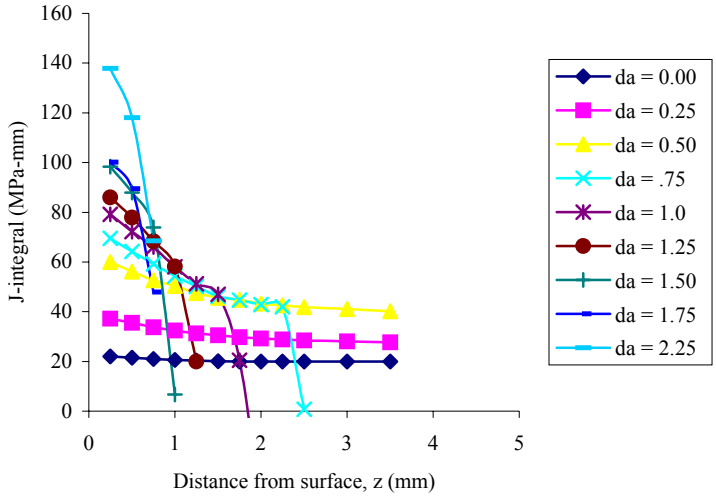

Figure 4.28: Point-wise, incremental J-integral for tunneled crack, $\varepsilon = 3.0$ mm.

Figure 4.28 only includes the through-thickness trends for crack extensions up to a surface crack extension, $\Delta a = 2.25$ mm since the data points beyond this become very erratic and would only serve to remove clarity from the plot. It is obvious from Figure 4.28 that the *J*-integral drops to zero at points closer and closer to the surface as the crack extends. This is because, as the crack extends, the elastic unloading zone in the wake of the crack tip is passed through much sooner on the interior layers. It is interesting to note that one can almost "track" the progression of the layers through the wake zone by observing the point at which each distinct crack extension curve drops off.

Figure 4.29 shows plots of incremental *J*-integral from the two extreme cases of near surface, and near mid-plane to illustrate the point discussed here.

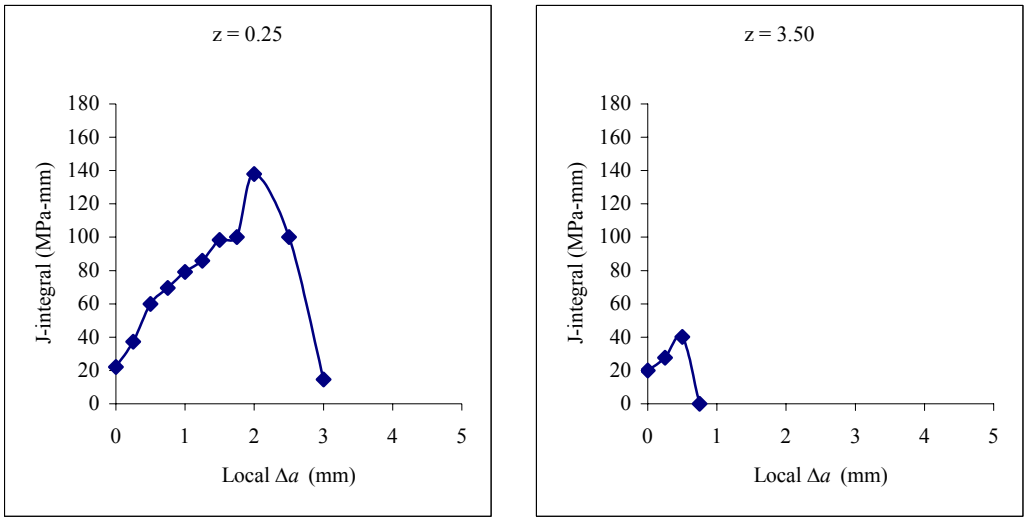

Figure 4.29: Incremental J-integral near surface and near mid-plane, ε = 3.0 mm.

4.3.3 COMPARISON OF 3-D T^*_ε AND J-INTEGRAL

It is difficult to draw a direct comparison between the T^*_ε and *J*-integral for the extreme tunneled case. Up to the point of crack initiation, and slightly beyond, T^*_ε and incremental *J*-integral should be almost identical due to the negligible differences between the moving contour and extending contour at these points. However, as the moving contour passes into the wake zone behind the current crack tip, the incremental *J*-integral is invalidated. Figure 4.30 contains plots of T^*_ε and incremental *J*-integral from the two extreme points overlaid with each other.

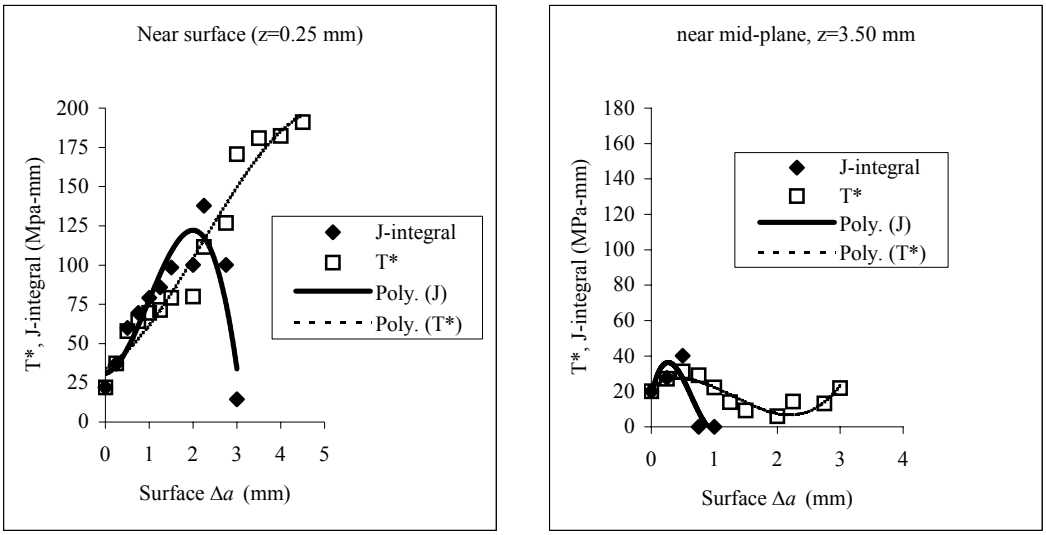

Figure 4.30: Comparison of T^*_ε and incremental J-integral, ε = 3.0 mm.

4.4 COMPARISON OF NUMERICAL AND EXPERIMENTAL RESULTS

Since the numerical results are obtained in a point-wise fashion along a tunneled crack front, it is difficult to directly compare them to experimental values obtained at the surface. The primary reason for this is the simple fact that an average value of T^*_ε through the thickness at each step in the FE analysis would not take into account the fact that center values are obtained at a point of crack extension that could be up to 4 mm longer than the amount of crack extension at the surface. However, experimental values could still be compared to numerically obtained values near the surface. Since the behavior in the extreme outer layer is a reflection of a surface singularity effect, which is difficult to quantify, the second layer in from the outside surface should be used. Figures 4.31, 4.32 and 4.33 are overlay plots of surface T^*_ε from moiré displacements in test "T5-3PB" with numerically obtained T^*_ε from the element interface located 0.25 mm from the surface. The general trend of numerically obtained T^*_ε is lower than the experimental, surface values primarily because of the fact that it is not obtained on the extreme surface.

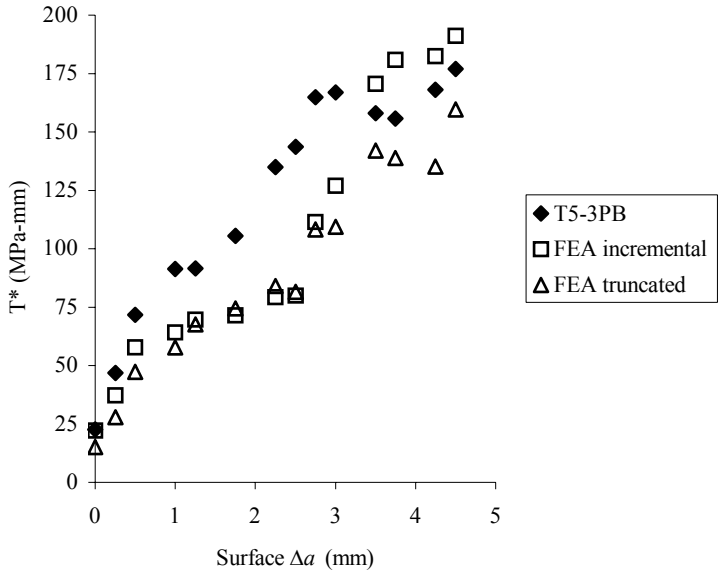

Figure 4.31: Comparison of experimental and numerical surface T^*_{ε}, ε = 3.0 mm.

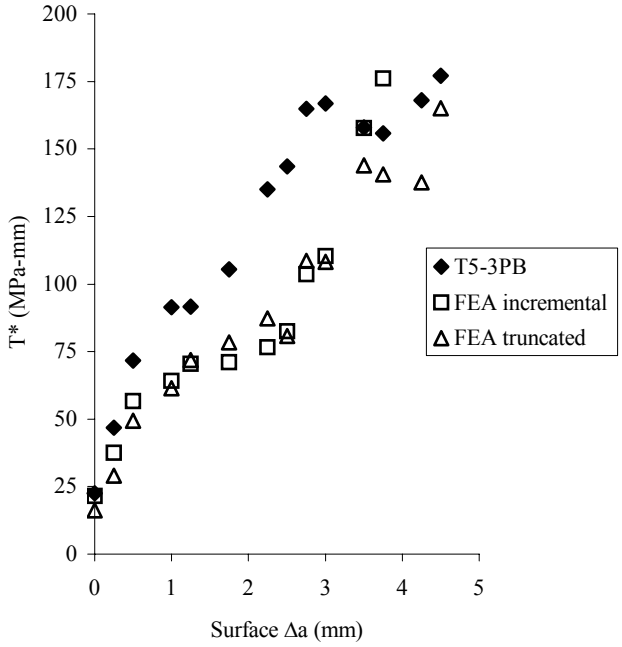

Figure 4.32: Comparison of experimental and numerical surface T^*_{ε}, ε = 2.0 mm.

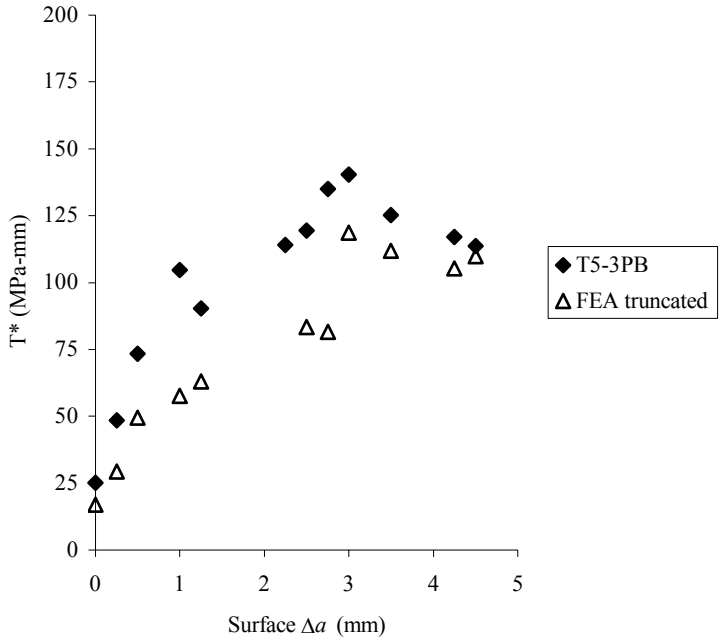

Figure 4.33: Comparison of experimental and numerical surface T^*_{ε}, ε = 1.0 mm.

It is tempting to apply some sort of correlation between surface values of T^*_{ε} and perhaps some average of T^*_{ε} through the thickness for the tunneled crack. Unfortunately, the surface values seem to be relatively detached from the behavior through the thickness. It is seen from the plots of numerically obtained T^*_{ε}, that the state of energy is very different on the interior of the specimen for cases of extreme tunneling. The only physically meaningful correlation would be between the experimental T^*_{ε} values and the near surface, numerically obtained values.

4.5 DISCUSSIONS

4.5.1 THE TRUNCATED INTEGRATION CONTOUR APPROACH

Originally, Okada [70] devised the T^*_{ε} calculation with a truncated contour approach to allow calculation of T^*_{ε} from experimentally obtained displacements where there is no

material loading history available. However, this should not imply that this method should not be used in cases where this history is available. It is evident from the data presented that it would be reasonable to use a truncated contour and hence, the deformation theory of plasticity to calculate T^*_ε for both experimental and numerical analyses. Even though the T^*_ε values using this method were approximately 5-10% on the non-conservative side in comparison to experimental results, the practicality of the approach is very appealing from the standpoint of a field technician. In comparison to using the incremental theory with an extending contour of integration, this method is unquestionably, far easier to apply. All that is needed is a current displacement field surrounding the current crack front point of interest. Output from a FE analysis is naturally compatible with this requirement as nodal displacements are easily extracted during a post-processing application.

Since nodal displacements are used, and the contour is truncated at the crack tip, Okada's method will have a smearing effect on localized events in an FE analysis. It can be argued that to be completely valid, one must apply the incremental theory of plasticity formulation with an extending integration contour to include the effect of such localized events. However, given the comparison between the results in the previous sections in this chapter and considering the difficulty encountered in using a full incremental theory approach and the intricacies of defining an extending contour in complex cases, this approach seems more feasible. This is especially true if the analysis were being performed in reverse, i.e., the application phase where the toughness curve is being used as a criterion for fracture in the FE analysis.

There is excellent correlation between the surface T^*_ε calculated via Okada's truncated contour with nodal displacements approach and the surface T^*_ε calculated via the incremental theory with a full contour. This is indicative of a very small contribution from the portions of the integration contour that trail the crack tip and the fact that, with a truncated contour only the portions which are still undergoing loading are considered,

allowing valid use of the deformation theory of plasticity in this case. The numerical difficulties seen in the calculation of incremental *J*-integral are likely a direct result of closing the integration contour through this wake zone which is not done for the extending contour T^*_ε calculation, or the truncated contour T^*_ε calculation.

4.5.2 COMPARISON OF SURFACE T^*_ε TO PLANE STRESS T^*_ε

A validation of this research comes with a comparison to plane stress T^*_ε from Ma [92] where T^*_ε was calculated for thin (0.8 mm) 2024-T3 aluminum, center notched specimens. Since the extreme surface of the 3-D case is thought to be near a plane stress state based on the existence of an approximately 13% shear lip observed on the fracture surface, T^*_ε values from this location should compare quantitatively with those of a plane stress analysis as long as similar sized Γ_ε contours are used. The numerical and experimental T^*_ε for ε=1.0 mm, in Figures 4.25 and 4.5, compare well in a quantitative sense with those in [92] which were obtained in a plane stress analysis. As seen in Figures 4.24 and 4.5, the results for a Γ_ε contour of ε = 2.0 mm also agree well with those in [92] for the same reasons. It must be assumed that the T^*_ε calculation through the thickness will also be correct since the surface values are acceptable. Since the T^*_ε integral has never been calculated in a state of high triaxiality such as the present, 3-D tunneled crack case, validation must come in the form of comparison to other known values. Figure 4.34 is an overlay plot of T^*_ε calculated at the surface numerically and experimentally for Γ_ε contour sizes of ε = 1.0 mm and 2.0 mm with plane stress T^*_ε from Ma [92] for the same contour sizes.

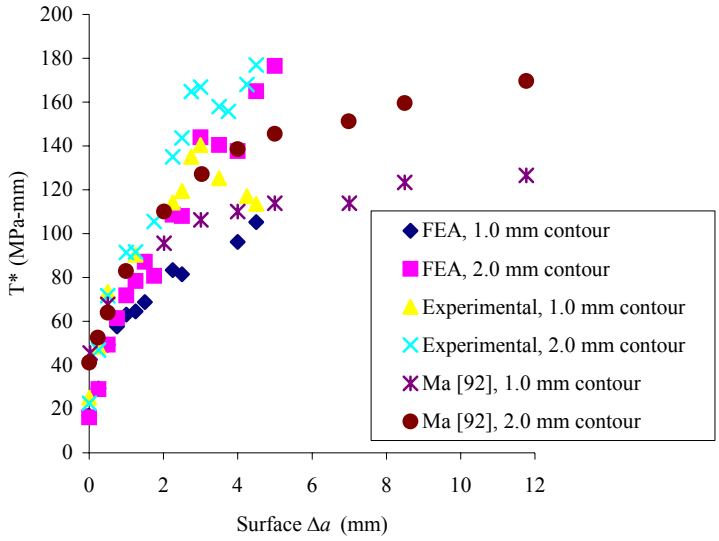

Figure 4.34: Comparison of surface T^*_ε to plane stress T^*_ε from Ma [92].

4.5.3 PLANE STRESS (SURFACE) AND PLANE STRAIN (MID-PLANE)

The numerically obtained T^*_ε shows a decreasing trend as the mid-plane is approached which is contrary to energy release rate behavior up to the point of crack initiation seen in previous studies involving *J*-integral. However, the extreme tunneling should not directly imply a trend of rising crack driving force toward the center. It is instead a result of lower resistance near the mid-plane, which is reflected in the lower T^*_ε values at this crack front location. The specimen being modeled is relatively thick and will exhibit fairly thin region of plane stress near the surface and transition to a plane strain state as the mid-plane is approached. This trend is seen directly in the plots of ε_{33} shown in section 4.1.1 of this chapter (Figures 4.8, and 4.9). In light of this, T^*_ε should instead be compared to a more local, physical parameter such as *CTOA*. This comparison is best made with the T^*_ε calculated on an ε = 1.0 mm contour size since *CTOA* is local to the crack tip. As the mid-plane of the specimen is approached and for extensive tunneling, the T^*_ε extending contour integral begins to exhibit characteristics similar to those of a

T^*_ε integral calculated with a moving contour as seen by Okada et. al. [70]. It is likely that the reason for this is the decreasing contribution from those portions of the contour in the wake of the extending crack. That is, each step in this case is more similar to a case of T^*_ε calculated on a truncated contour as the strain history never builds as in the case of a controlled, stably growing crack. Regardless, some comparison must be drawn between mid-plane and surface T^*_ε in order to allow use of experimentally obtained values for prediction of crack extension throughout the thickness of a specimen.

At crack initiation, and within the first few steps of crack growth, the surface and mid-plane values are quantitatively similar. However, as the crack extends, the surface T^*_ε rapidly increases while the mid-plane value stays fairly steady, with a slight trend toward rising. After approximately 5-6 mm of crack growth, the two reach a steady state with respect to each other and a comparison can be made between the plane stress (surface) values and plane strain (mid-plane) values.

For the linear elastic case, a comparison of J_C and J_{IC} for very thin specimens (plane stress) and thick specimens (near plane strain) respectively is made for 2024-T3 aluminum alloy as (K values from [105]);

$$\left(\frac{K_{IC}}{K_C^{t=0.8mm}}\right)^2 \frac{1}{\left(1-\nu^2\right)} = \left(\frac{33\ \text{MPa}\sqrt{m}}{115\ \text{MPa}\sqrt{m}}\right)^2 \frac{1}{\left(1-.34^2\right)} = 0.09 \tag{4.3}$$

which shows plane strain J_{IC} to be roughly 9% of plane stress J_C. Since J-integral is incapable of characterizing the crack tip behavior after crack extension, this comparison cannot realistically be made for the case of extended crack extension and extreme tunneling. However, this comparison can be used to make an analogy to the behavior of a steady state T^*_ε toughness behavior since this would represent the "critical" value of T^*_ε. An inspection of the plots of T^*_ε for all contour sizes, and especially the very near-tip $\varepsilon = 1.0$ mm contour reveals a relationship between plane stress (surface) T^*_ε and plane strain (mid-plane) T^*_ε. While the 3-point bend specimen configuration did not allow

sufficient crack extension to achieve the complete steady state T^*_ε value, it comes close enough to begin to show signs of achieving a steady state value which should occur at a crack extension roughly equivalent to half the specimen thickness. At the final point of crack extension (5.0 mm on the surface), the ratio between surface T^*_ε and mid-plane T^*_ε is roughly 10 %, regardless of contour size, or method of calculation. The much lower plane strain T^*_ε is a direct reflection of the much lower resistance to crack extension in the plane strain region in comparison to the surface, plane stress region. The very close agreement with the ratio of linear elastic fracture toughnesses is an encouraging development since this would indicate the possibility for using plane stress (surface) T^*_ε values to predict the fracture resistance on the interior of a thick specimen. Figure 4.35 highlights this comparison for the near-tip plane stress and plane strain T^*_ε resistance curves.

It is evident in Figures 4.22, 4.23, and 4.24 that the T^*_ε values calculated using the truncated contour with deformation theory are far less susceptible to numerical noise and tend to be a slightly lower than those calculated with incremental theory and a full, extending contour. This discrepancy is due to the fact that the deformation theory calculation on a truncated contour is based solely on the displacement field and therefore cannot account for the explicit strain history. However, it is obvious that the T^*_ε calculated this way is similar, quantitatively with both the experimentally obtained values and the numerical values obtained using incremental plasticity and an extending contour of integration.

If the analysis is restricted to a contour very near the crack tip (localized crack tip driving force), Okada's truncated contour and deformation theory analysis procedure can be used most effectively. In addition, a comparison can be drawn between the T^*_ε behavior on this very near-tip contour and *CTOA*, which is itself a very local crack tip parameter. Since *CTOA* seems to be able to accurately predict crack extension (see Dawicke, Newman ,et al. [1], [13], [14], [16]), a comparison between *CTOA* and near-tip T^*_ε

provides a measure of validation. Figure 4.35 is a combined plot from Figure 4.26 of surface and mid-plane T^*_ε calculated on an ε = 1.0 mm contour, representing the difference between a plane stress resistance curve, and a plane strain resistance curve. Figure 4.36 shows the *CTOA* plotted in the same manner.

The ratio of surface *CTOA* to mid-plane *CTOA* is roughly 40-50%, which is much higher than the ratio between surface and mid-plane T^*_ε. Since there is no known quantitative comparison between the two parameters, this observation is inconclusive. However, it is sufficient to note that the two compare in a qualitative manner. It is well known that *CTOA* is incapable of fracture resistance characterization in the initial stages of crack growth where the "hump" in the surface curve is generally attributed to tunneling. Beyond this initial transient, the two parameters compare well qualitatively.

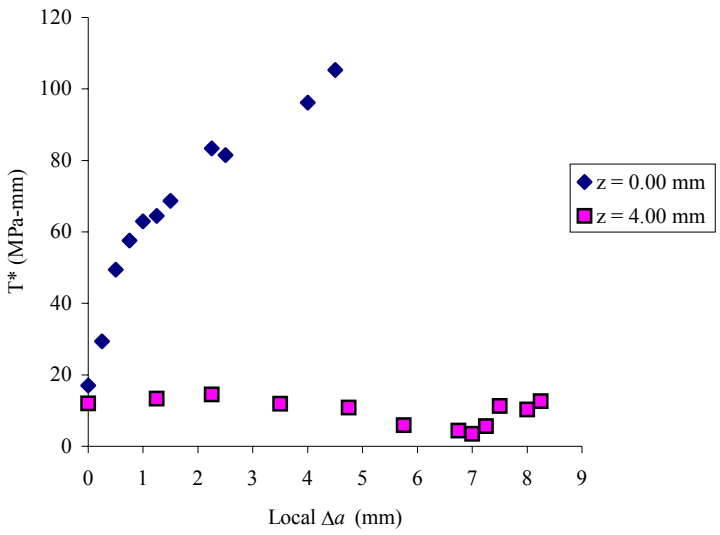

Figure 4.35: Plane stress and plane strain, near-tip T^*_ε, ε = 1.0 mm.

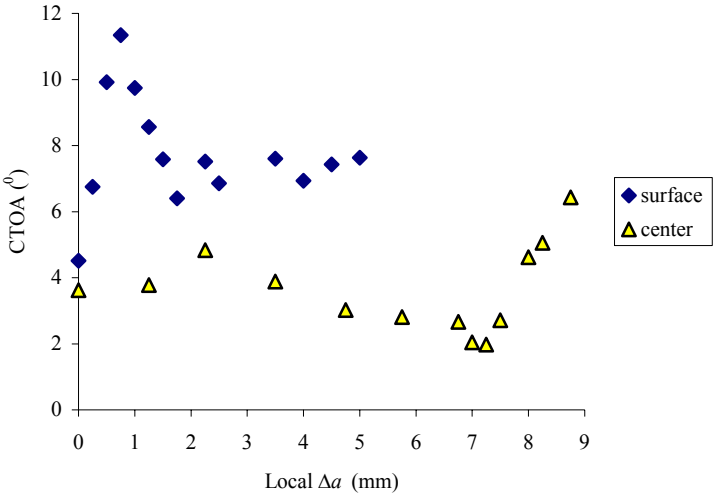

Figure 4.36: Plane stress and plane strain CTOA.

It is noted that the plane strain (mid-plane) T^*_ε and *CTOA* resistance curves exhibit a drop followed by a sharp rise at a local crack extension of approximately 7.0 mm. This is a function of the numerical model and the way the crack tip interacts with the external loading. At this crack extension level, the slowed tunneling combined with an interaction with the boundary condition induced stress field produces a blunting effect at the mid-plane crack tip. This is very evident in the *CTOA* resistance curve, and local T^*_ε (ε = 1.0 mm) curve where crack tip behavior has a strong influence.

4.5.4 RELATIONSHIP BETWEEN PLANE STATE AND INTEGRATION CONTOUR

In past analyses and for this analysis as well, one integration contour size has been used to observe T^*_ε behavior for any particular data set. That is, if a contour size of 2.0 mm is chosen, all values are calculated using this contour size, regardless of position along the crack front. In order to explicitly follow the strategy laid out here for assigning an integration contour, the integration contour size would need to change according to position along the tunneled crack front or, more appropriately, as a function of the constraint present at each particular through-thickness position. If a transition point to

plane strain is defined as the location of the integration contour, then the ε_{33} plots (Figures 4.8 and 4.9) would dictate a changing integration contour size along the tunneled crack front. An examination of the T^*_ε data presented for this analysis also tends to support this theory, albeit in a weak way. T^*_ε near the surface is also slightly closer to the plane stress values of Ma [92] for larger contour sizes. A correlation cannot be drawn for mid-plane values of T^*_ε, but it could be assumed that the same will likely be true of plane strain T^*_ε.

4.5.5 IDEALIZED CASE: STRAIGHT CRACK FRONT T^*_ε AND J-INTEGRAL

Since a new post-processing program was written for calculation of T^*_ε in this study, an idealized numerical analysis was performed to get a baseline comparison between T^*_ε and *J*-integral in simplified conditions since the two can be considered approximately equal prior to, and just beyond crack initiation. As further validation, the general trend of T^*_ε should be one of an increase-peak-flattening. In this portion of the analysis, a model was built which incorporated a straight crack front for several steps of crack extension. The geometrical characteristics of the general model are identical to the "real" numerical model except that fewer layers are utilized since there is no tunneling that would require high resolution through the thickness. Also, the displacement boundary conditions applied to this model have been estimated based loosely on the displacement conditions prescribed in the "real" model (obtained from experimental analysis) and the stepwise progression is compressed to get a comparison between average crack extensions in the tunneled case, and the straight crack extension level.

For this simple, idealized analysis a Γ_ε contour of $\varepsilon = 2.0$ mm is chosen to expediate the numerical processing since larger contours can result in hundreds more EDI elements included in the calculation. The width of the EDI region is set at 1.0 mm to provide adequate resolution. Also, only 2.0 mm of crack extension is analyzed here since the analysis served its purpose at this amount of crack extension.

Figure 4.37 shows the T^*_ε trend for the idealized case up to a crack extension of 2.0 mm. In this plot, trends for different locations along the crack front (z) are shown. The "hump" seen in these curves for the near surface T^*_ε at a crack extension of 1.25 mm is likely due to an artificially fast formation of a plastic zone at the surface and then a transition of this plasticity toward the center as the crack extends. The higher values of T^*_ε near the mid-plane are expected since tunneling would be expected in a real crack extension case due to the increasing crack tip energy requiring dissipation (T^*_ε). Figure 4.38 is a plot of *J*-integral from the same analysis. As expected, the *J*-integral is quantitatively similar to T^*_ε, especially near the quarter thickness point (1.00 mm). It also exhibits the expected peak-decrease behavior while T^*_ε exhibits its classic peak-flattening behavior.

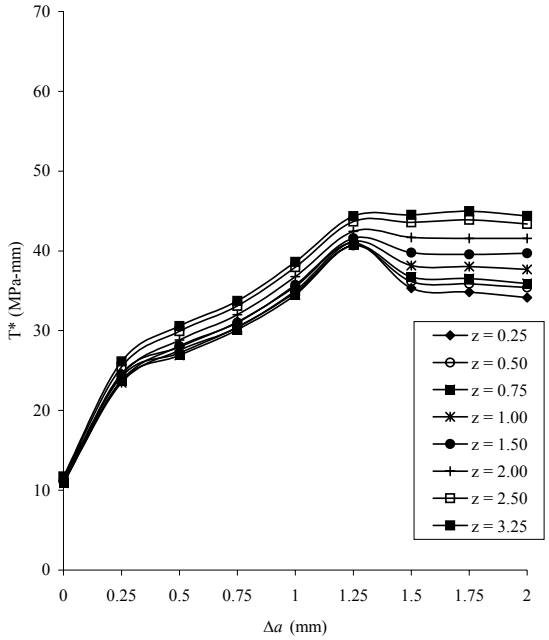

Figure 4.37: T^*_ε for idealized, straight crack front, ε = 2.0 mm.

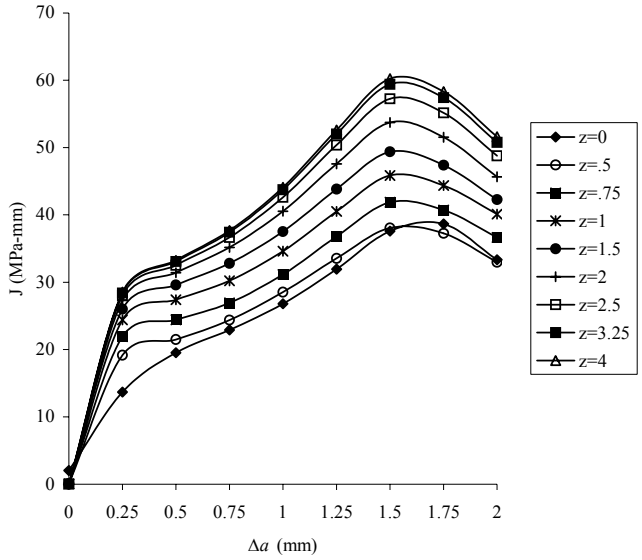

Figure 4.38: J-integral for idealized, straight crack front, ε = 2.0 mm.

Figures 4.39, and 4.40 show trends of T^*_ε and *J*-integral extracted from the plots in Figures 4.37 and 4.38. These figures highlight the differences in *J*-integral and T^*_ε for this idealized case. The mid-plane trends are very similar at small crack extensions but show divergence in behavior as the crack extends. Far-field *J*-integral would continue rising, but near field *J*-integral will peak and then drop. These expected trends are evident in Figures 4.39, and 4.40.

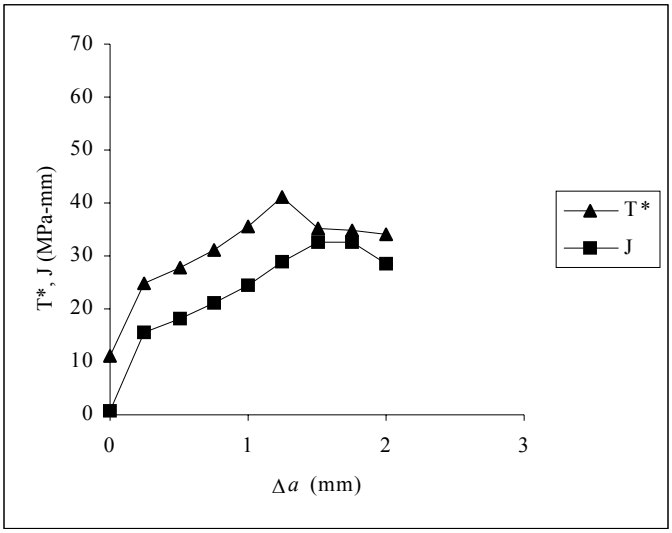

Figure 4.39: T^*_{ε} and J-integral near specimen surface (z=0.25 mm), ε=2.0 mm.

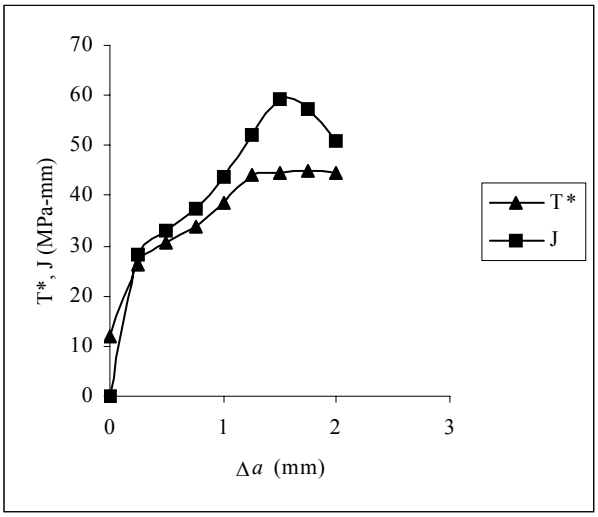

Figure 4.40: T^*_{ε} and J-integral for mid-plane (z=3.25 mm), ε =2.0 mm.

4.5.6 IMPLICATIONS ON THE STRAIGHT CRACK ASSUMPTION

It is obvious that there is a significant, qualitative difference between the T^*_ε calculated in the idealized, straight crack case and the real, tunneled crack front case. In comparison to the straight crack case, the tunneled crack front T^*_ε (and hence, *J*-integral) drops significantly as the mid-plane of the relatively thick specimen is approached, and with a short amount of crack extension. The single specimen technique for *J*-integral estimation in ASTM E 813 relies on an assumption of a straight crack front, with an average, estimated crack front calculated via a compliance measurement. Hence, through-thickness behavior similar to the idealized case discussed in the previous section would be expected. The existence of the discrepancy between the idealized, straight crack front case and the tunneling case casts some doubt on the validity of the single specimen technique for *J*-integral estimation. Since the mid-plane values vary so significantly between the two cases, the single specimen technique for *J* estimation will likely produce non-conservative results.

4.5.7 GENERATION PHASE-APPLICATION PHASE VALIDATION

An objective in this research was to build T^*_ε resistance curves in their generation phase through a combined experimental and numerical approach so that they could eventually be utilized in the application phase. The localized T^*_ε resistance curves were obtained for several points along the crack front for this 2024-T351 aluminum alloy in the 3-point bend specimen configuration. In the previous sections, these localized resistance curves were reported for the surface (plane stress), quarter-plane (transition), and mid-plane (plane strain) regions. These curves may now be applied as a fracture criterion in an application phase numerical analysis to predict the tunneling behavior in a similar specimen geometry. The successful prediction of crack front tunneling along with a match with far field parameters such as Crack Mouth Opening Displacement (CMOD) would validate the local T^*_ε resistance curves.

CHAPTER 5: CONCLUSIONS AND RECCOMENDATIONS

5.1 SUMMARY

The T^*_ε contour integral has been numerically evaluated along a 3-D, tunneling crack front in a thick, plane strain specimen. This numerical value has been compared near the surface with T^*_ε calculated on the surface of the aluminum, 3-point bend specimen from a moiré displacement field generated in the experimental process. In addition, values of incremental *J*-integral and *CTOA* were obtained for the purpose of comparison. Since T^*_ε has been primarily studied experimentally and numerically in 2-D form, or 3-D form without crack extension, the evaluation of T^*_ε for this 3-D tunneling case with crack extension and a plane strain interior represents a unique contribution to the study of the mechanics of ductile fracture.

A good correlation between T^*_ε calculated with incremental theory of plasticity and an extending contour and T^*_ε calculated using deformation theory of plasticity and a truncated contour was observed. This implies that the far simpler, deformation theory approach may be used in place of the extremely difficult and time consuming incremental theory approach. In addition, much less mesh refinement would likely be required if only the current displacement field is used for the calculation. The ability to use this approach would vastly improve the status of T^*_ε as an applicable "in the field" fracture toughness parameter.

The downward trend in T^*_ε values as the mid-plane is approached is indicative of the lack of development of an appreciable amount of strain energy and/or plastic dissipation. The crack tunnels to an extreme extent in comparison to the propagation of the crack tip at the surface because there is far less resistance to crack propagation in the interior of the specimen where the T^*_ε toughness value is lower. The constraint present in the interior

of the specimen forces this state of plane strain much closer to the crack tip than near the surface where almost a complete plane stress state exists. Up to, and at the point of crack extension for a mildly tunneled, or straight crack, the material surrounding the crack tip is allowed to build up elastic strain energy and very little plastic dissipation. In this case, the T^*_ε integral behaves in a fashion similar to the *J*-integral, that is, a slight rising trend along the crack front toward the specimen mid-plane. At this point, both T^*_ε and *J*-integral are functions of elastic strain energy, and are directly related to the linear elastic fracture toughness, so this is expected. After tunneling begins, the T^*_ε integral is larger at the surface and smaller near the mid-plane, because there is far more plastic distortion near the surface where a majority of the current load is carried. This trend is reflected in the *CTOA* variation through the thickness as well. At the surface, where there is large plastic deformation, *CTOA* is close to its accepted value of between 5-8 degrees but drops as the mid-plane is approached in a similar manner as the T^*_ε integral. Although there is no direct correlation between the two parameters, the fact that *CTOA* is a geometrical parameter that is generally accepted as a stable fracture characterizing parameter means a similar trend in T^*_ε is a good sign.

The interior T^*_ε values are similar to incremental *J*-integral, except that they are still calculated on a contour that has extended with the crack and therefore contain the entire history of the crack extension. It is interesting to note that incremental *J*-integral trends seem to follow a pattern of reaching a peak in an ever-closer proximity to the model surface as the crack extends. This tends to imply some physical connection between incremental *J*-integral and the formation of plasticity in front of the crack tip. Regardless, incremental *J*-integral has no physical meaning after a crack extension equal to the contour size because of the contribution of the integration is in the wake zone behind the current crack tip. In addition, closing the contour of integration through an active wake zone will definitely lead to numerical difficulties. This effect is seen in the difference between T^*_ε and incremental *J*-integral.

A reasonably good correlation is seen between experimentally obtained, surface values of T^*_ε and the near surface, numerically obtained values. The fact that the numerically obtained values are slightly lower than the experimental surface values can be attributed to the inability to obtain numerical results at the extreme surface. Rather, they are obtained at the interface between the first and second element layers (0.25 mm from real surface). The reasons for this are; first, the surface singularity was very coarsely modeled, using a thin (0.25 mm) element layer near the surface and the effects of this are unknown, second, the use of a triangular *s*-function does not allow a calculation at the extreme outer and inner nodes.

5.2 CONCLUSIONS

- T^*_ε values generally reach a peak of approximately 175 MPa-mm on the surface and approximately 30 MPa-mm in the mid-plane. This significant difference is due to the existence of a plane stress state at the extreme surface, and a plane strain region at the mid-plane of the specimen.

- A deformation theory of plasticity with a truncated contour can be used in the FE analysis to provide a good measure of ease of use in comparison to a full calculation involving the incremental theory of plasticity and an elongating integration contour.

- T^*_ε for the 3-D configuration and tunneling crack front behaves similarly to the local crack tip parameter, *CTOA* for corresponding through-thickness resistance curves. Thus, local T^*_ε is assumed to represent the point-wise energy inflow to the crack front.

- T^*_ε is very sensitive to the constraint level in the material surrounding the crack tip and will exhibit distinct plane stress and plane strain values. The ratio of the

plane strain T^*_ε and planes stress T^*_ε values is approximately 10% for this material and specimen geometry.

- A good quantitative comparison between the ratios of plane strain and plane stress linear elastic fracture toughness and plane strain and plane stress T^*_ε presents the possibility for a relationship to exist between plane states and corresponding T^*_ε values.

- The *J*-integral estimation within the single specimen technique of ASTM E 813 may require additional thought with regard to the implications of assuming an average, straight crack front.

5.3 RECCOMENDATIONS

1) As computing power becomes more readily available, the numerical model should be refined to include more layers through the specimen thickness and a different approach to focusing the mesh to the crack tip.

2) The post-processing software should be enhanced to allow use with a variety of element types. It should also be build to accommodate the tunneling crack front by allowing rotation of the EDI region to adapt to the current crack front.

3) A detailed analysis of the deformation field in the vicinity of the crack tip should performed with a goal of defining how the EDI region should be defined for thick model configurations that incorporate tunneling.

4) This work should be extended to a creep analysis. This would incorporate large deformation and would highlight connections between the T^*_ε integral and the amount of plastic dissipation in the region of interest.

5) The resulting local T^*_ε toughness curves should be used in an application phase to attempt prediction of tunneling behavior in a numerical model.

6) A further exploration of the use of the truncated contour of integration approach should be considered for use with FE analyses. While this approach is not a replacement for the incremental plasticity approach, it still provides a reasonable estimate of numerical T^*_ε.

7) T^*_ε should be calculated for the case of a growing, semi-elliptical surface flaw in a tensile specimen. Tunneling will be much less severe for this type of specimen. The elliptical surface flaw should also allow a more natural EDI region to be used and will still have the capability for characterizing plane stress and plane strain T^*_ε, but only for short crack extensions.

8) The extreme crack tunneling case should be studied further as it may lead to a mechanistic explanation of the ductile to brittle transition by way of differences seen in constraint levels as the specimen thickness is traversed.

BIBLIOGRAPHY

1. Dawicke, D.S., Newman, J.C. Jr., and Bigelow, C.A., "Three Dimensional *CTOA* and Constraint Effects During Stable Tearing In A Thin-Sheet Material." *NASA TM-109183*, February, 1995.

2. Atkins, A.G., and Mai, Y.W., *Elastic and Plastic Fracture*, Ellis Horwood Limited, 1985, pp. 269-368.

3. Wells, A. A., "Unstable Crack Propagation in Metals: Cleavage and Fast Fracture." *Proceedings of the Crack Propagation Symposium*, Vol. 1, Paper 84, Cranfield, UK, 1961.

4. Cottrell, A. H., *I.S.I. Special Reports No. 69*, 1961, p. 281.

5. Anderson, T.L., *Fracture Mechanics: Fundamentals and Applications*, 2nd Edition, CRC Press, Boca Raton, 1995.

6. Rice, J.R., "A Path Independent Integral and the Approximate Analysis of Strain by Notches and Cracks." *Journal of Applied Mechanics*, Vol. 35, 1968, pp. 379-386.

7. Burdekin, F.M., and Dawes, M.G., "Practical Use of Linear Elastic and Yielding Fracture Mechanics with Particular Reference to Pressure Vessels." *Proceedings of the Institute of Mechanical Engineers Conference*, London, May 1971, pp. 28-37.

8. Kanninen, M.F., and Popelar C.H., *Advanced Fracture Mechanics*, Oxford University Press, Inc., New York, 1985.

9. Shih, C. F., De Lorenzi, H.G., and Andrews, W. R., "Studies on Crack Initiation and Stable Crack Growth." *Elastic-Plastic Fracture, ASTM STP 668*, J. D. Landes, J. A. Begley, and G. A. Clark, Eds., American Society for Testing and Materials, 1979, pp. 65-120.

10. Kanninen, M. F., Rybicki, E. F., Stonesifer, R. B., Broek, D., Rosenfield, A. R., Marschall, C. W., and Hahn, G. T., "Elastic-Plastic Fracture Mechanics in Two-Dimensional Stable Crack Growth and Instability Problems." *Elastic-Plastic Fracture, ASTM STP 668*, J. D. Landes, J. A. Begley, and G. A. Clark, Eds., American Society for Testing and Materials, 1979, pp. 121-150.

11. Brocks, W., and Yuan, H., "Numerical Studies on Stable Crack Growth." *Defect Assessment in Components - Fundamentals and Applications*, ESIS/EGF9, Blauel, J. G., and Schwalbe, K. -H., Eds., Mechanical Engineering Publications, London, 1991, pp. 19-33.

12. Schwalbe, K. H., and Cornec, A., "The Engineering Treatment Model (ETM) and its Practical Application." *Fatigue and Fracture of Engineering Materials and Structures*, Vol. 14, No. 4, 1991, pp. 405-412.

13. Newman, J. C. Jr., Bigelow, C. A., and Dawicke, D. S., "Finite-Element Analysis and Fracture Simulation in Thin-Sheet Aluminum Alloy." *Proceedings of the International Workshop on Structural Integrity of Aging Airplanes*, Atluri, S. N., Harris, C. E., Hoggard, A., Miller, N., and Sampath, S. G., Eds., 1992, pp. 167-186.

14. Newman, J. C. Jr., Dawick, D. S., Sutton, M. A., and Bigelow, C. A., "A Fracture Criterion for Widespread Cracking in Thin-Sheet Aluminum Alloys." *International Committee on Aeronautical Fatigue: 17th Symposium*, Stockholm, Sweden, 1993.

15. Bakuckas, J. G. Jr., and Newman, J. C. Jr., "Prediction of Stable Tearing of 2024-T3 Aluminum Alloy Using the Crack-Tip Opening Angle Approach." *NASA-TM-109023*, September, 1993.

16. Dawicke, D. S., Sutton, M. A., Newman, J. C. Jr., and Bigelow, C. A., "Measurement and Analysis of Critical *CTOA* for an Aluminum Alloy Sheet." *Fracture Mechanics: 25th Volume ASTM STP 1220*, Erdogan, F., Ed., American Society for Testing and Materials, Philadelphia, 1995, pp. 359-379.

17. Newman, J. C. Jr., Shivakumar, K. N., and McCabe, D. E., "Finite Element Fracture Simulation of A533B Steel Sheet Specimens." *Defect Assessment in Components – Fundamentals and Applications*, ESIS/EGF9, Blauel, J. G., and Schwalbe, K.-H., Eds., Mechanical Engineering Publications, London, 1991, pp. 117-126.

18. Dawicke, D. S., "Residual Strength Predictions using a *CTOA* Criterion." *Proceedings of the FAA-NASA Symposium on the Continued Airworthiness of Aircraft Structures*, July 1997, pp. 555-566.

19. Hom, C. L., and McMeeking, R. M., "Large Crack Tip Opening in Thin Elastic-Plastic Sheets." *International Journal of Fracture*, Vol. 45, 1980, pp. 103-122.

20. Gullerud, A. S., Dodds, R. H. Jr., Hampton, R. W., and Dawicke, D. S., "3-D Finite Element Modeling of Ductile Crack Growth in Thin Aluminum Materials." *Fatigue and Fracture Mechanics: 30th Volume*, Jerina, K. L., and Paris, P. C., Eds., ASTM, 1998.

21. Bilby, B. A., and Eshelby, J. D., "Dislocations and the Theory of Fracture." *Fracture, An Advanced Treatise*, Vol. A1, Liebowitz, H., Ed., Academic Press, New York, 1968, pp. 99-182.

22. Cherapanov, G. P., "Crack Propagation in Continuous media." *Prikl. Mat. Mekh.*, Vol. 31, 1967, pp. 476-488.

23. Griffith, A. A., "The Phenomena of Rupture and Flow in Solids." *Philosophical Transactions*, Series A., Vol. 221, 1920, pp. 163-198.

24. Irwin, G. R., "Onset of Fast Crack Propagation in High Strength Steel and Aluminum Alloys." *Sagamore Research Conference Proceedings*, Vol. 2, 1956, pp. 289-305.

25. Hutchinson, J. W., "Singular Behavior at the End of a Tensile Crack Tip in a Hardening Material." *Journal of the Mechanics and Physics of Solids*, Vol. 16, 1968, pp. 13-31.

26. Rice, J. R., and Rosengren, G. F., "Plane Strain Deformation near a Crack Tip in a Power Law Hardening Material." *Journal of the Mechanics and Physics of Solids*, Vol. 16, 1968, pp. 1-12.

27. Hutchinson, J. W., and Paris, P. C., "Stability Analysis of J-Controlled Crack Growth." *Elastic-Plastic Fracture, ASTM STP 668*, Landes, J. D., Begley, J. A., and Clarke, G. A., Eds., American Society for Testing and Materials, 1979, pp. 37-64.

28. Li, Y, and Wang, Z., "Higher-Order Asymptotic Field of Tensile Plane-Strain Nonlinear Crack Problems." *Scientia Sinica*, Series A, Vol. 29, No. 9, pp. 941-955.

29. O'Dowd, N. P., and Shih, C. F., "Family of Crack-Tip Fields Characterized by a Triaxiality Parameter –I. Structure of Fields." *Journal of the Mechanics and Physics of Solids*, Vol. 39, 1991, pp. 898-1015.

30. O'Dowd, N. P., and Shih, C. F., "Family of Crack-Tip Fields Characterized by a Triaxiality Parameter –II. Fracture Applications." *Journal of the Mechanics and Physics of Solids*, Vol. 40, 1992, pp. 939-963.

31. Kobayashi, A. S., "3-D Experimental Fracture Analysis at High Temperature II." *Proposal to Department of Energy*, University of Washington, Oct. 1, 1996.

32. Chao, Y., and Lam, P., "On the Use of Constraint Parameter *A2* Determined from Displacement in Predicting Fracture Event." *Engineering Fracture Mechanics*, Vol. 61, 1998, pp. 487-502.

33. Dadkhah, M. S., Kobayashi, A. S., and Morris, W. L., "Further Studies in the *HRR* Field of a Moving Crack, An Experimental Analysis." *Journal of Plasticity*, Vol. 6, 1990, pp. 636-650.

34. Dadkhah, M. S., and Kobayashi, A. S., "Two Parameter Crack Tip Stress Field Associated with Stable Crack Growth in a Thin Plate." *Fracture Mechanics, Twenty Fourth Volume, ASTM STP 1207*, Landes, J. D., McCabe, D. E., and Boulet, J. A. M., Eds., 1994, pp. 48-61.

35. Sciammarella, C. A., and Combel, O., "An Elasto-Plastic Analysis of the Crack Tip Field in a Compact Tension Specimen." *Engineering Fracture Mechanics*, Vol. 55, No. 2, 1996, pp. 209-222.

36. Moran, B., and Shih, C. F., "Crack Tip and Associated Domain Integrals from Momentum and Energy Balance." *Engineering Fracture Mechanics*, Vol. 27, No. 6, 1987, pp. 615-642.

37. Cotterell, B., and Atkins, A. G., "A review of the *J* and *I* integrals and their Implications for Crack Growth Resistance and Toughness in Ductile Fracture." *International Journal of Fracture*, Vol. 81, 1996, pp. 357-372.

38. Siverns, M. J., and Price, A. T., "Crack Propagation Under Creep Conditions in a Quenched 2 ¼ Chromium 1 Molybdenum Steel." *International Journal of Fracture*, Vol. 9, No. 2, 1973, pp. 199-207.

39. Landes, J. D., and Begley, J. A., "A Fracture Mechanics Approach to Creep Crack Growth." *Mechanics of Crack Growth: ASTM STP 590*, American Society for Testing and Materials, 1976, pp. 128-148.

40. Goldman, N. L., and Hutchinson, J. W., "Fully Plastic Crack Problems: The Center-Cracked Strip Under Plane Strain." *International Journal of Solids and Structures*, Vol. 11, 1975, pp. 575-591.

41. Hoff, N. J., "Approximate Analysis of Structures In the Presence of Moderately Large Creep Deformations." *Quarterly of Applied Mathematics*, Vol. 12, No. 1, 1954, pp. 49-55.

42. Ohji, K, Ogura, K., and Kubo, S., *Transactions, Japanese Society of Mechanical Engineers*, Vol. 42, 1976, pp. 350-358.

43. Nikbin, K. M., Webster, G. A., and Turner, C. E., *Cracks and Fracture (9th Conference), ASTM STP 601*, American Society for Testing and Materials, Philadelphia, 1976, pp. 47-62.

44. "Standard Test Method for J_{IC}, A Measure of Fracture Toughness." *ASTM Standard E813-89*, 1993, pp. 738-752.

45. Riedel, H., "Creep Crack Growth." *Fracture Mechanics: Perspectives and Directions (Twentieth Symposium) ASTM STP 1020*, Wei, R. P., and Gangloff, R. P., Eds., American Society for Testing and Materials, Philadelphia, 1989, pp. 101-126.

46. Riedel, H., "The Extension of a Macroscopic Crack at Elevated Temperature by the Growth and Coalescence of Microvoids." *Creep in Structures*, Ponter, A. R. S., and Hayhurst, D. R., Eds., Springer-Verlag, Berlin, 1981, pp. 504-519.

47. Hui, C. Y., and Banthia, V., "Extension of Cracks at High Temperatures by Growth and Coalescence of Voids." *International Journal of Fracture*, Vol. 25, 1984, pp. 53-67.

48. Riedel, H., and Wagner, W., *Advances in Fracture Research, Proceedings 6th International Conference on Fracture*, Vol. 3, Valluri, S. R., et al, Eds., Pergamon Press, Oxford, 1985, pp. 2199-2206.

49. Detampel, V., "An Investigation of Creep Crack Growth in Creep-Resistant Pipe Steels." *Ph.D. Thesis*, RWTH Aachen, Germany, 1987.

50. Saxena, A., "Creep Crack Growth under Non-Steady-State Conditions." *Fracture Mechanics: Seventeenth Volume, ASTM STP 905*, Underwood, J. H., Chait, R., Smith, C. W., Wilhelm, D. P., Andrews, W. A., and Newman, J. C., Eds., American Society for Testing and Materials, Philadelphia, 1986, pp. 185-201.

51. Ehler, R., and Riedel, H., "A Finite Element Analysis of Creep Deformation in a Specimen Containing a Macroscopic Crack." *Advances in Fracture; Proceedings of the Fifth International Conference on Fracture*, Vol. 2, Francois, D., Ed., Pergamon, New York, 1981, pp. 691-698.

52. Ainsworth, R. A., and Budden, P. J., "Crack Tip Field under Non-Steady Creep Conditions—I. Estimates of the Amplitude of the Fields.", *Fatigue Fracture in Engineering Structures*, Vol. 13, 1990, pp. 263-276.

53. Dogan, B., Saxena, A., and Schwalbe, K. H., "Creep Crack Growth in Creep-Brittle Ti-6242 Alloys." *Materials At High Temperatures*, Vol. 10, No. 2, 1992, pp. 138-143.

54. Linkens, D., Busso, E. P., Dean, D. W., "Predictions of Non-Steady Asymptotic Crack Tip Fields in Power Law Creeping Materials." *Nuclear Engineering and Design*, Vol. 158, No. 2-3, 1995, pp. 377-385.

55. Riedel, H., and Rice, J. R., "Tensile Cracks in Creeping Solids." *Fracture Mechanics: Twelfth Conference, ASTM STP 700*, American Society for Testing and Materials, 1980, pp. 112-130.

56. Busso, E. P., Dean, D. W., and Linkens, D., "On the Effects of Loading Conditions and Geometry on Time-Dependent Singular Crack Tip Fields." *Engineering Fracture Mechanics*, Vol. 50, No. 2, 1995, pp. 231-247.

57. Atluri, S. N., "Path Independent Integrals in Finite Elasticity and Inelasticity, With Body Forces, Inertia, and Arbitrary Crack Face Conditions." *Engineering Fracture Mechanics*, Vol. 16, 1982, 341-364.

58. Stonesifer, R. B., and Atluri, S. N., "On a Study of the (ΔT) and C^* Integrals for Fracture Analysis Under Non-Steady Creep." *Engineering Fracture Mechanics*, Vol. 16, No. 5, 1982, pp. 625-643.

59. Atluri, S. N., Nishioka, T., and Nakagaki, M., "Incremental Path-Independent Integrals in Inelastic and Dynamic Fracture Mechanics." *Engineering Fracture Mechanics*, Vol. 20, No. 2, 1984, pp. 209-244.

60. Brust, F. W., Nishioka, T., Atluri, S. N., and Nakagaki, M., "Further Studies on Elastic-Plastic Stable Fracture Utilizing the T^* Integral." *Engineering Fracture Mechanics*, Vol. 22, No. 6, 1985, pp. 1079-1103.

61. Atluri, S. N., "Energetic Approaches and Path Independent Integrals in Fracture." *Computational Methods in the Mechanics of Fracture*, Atluri, S. N., Ed., North Holland Publishing Company, 1986, pp. 121-162.

62. Pyo, C. R., Okada, H., and Atluri, S. N., "Residual Strength Prediction for Aircraft Panels with Multiple-Site Damage, Using the 'EPFEAM' for Stable Crack Growth." *Computational Mechanics*, Vol. 16, 1995, pp. 190-196.

63. Nikishkov, G. P., and Atluri, S. N., "An Equivalent Domain Integral Method for Computing Crack-Tip Integral Parameters in Non-Elastic, Thermo-Mechanical Fracture." *Engineering Fracture Mechanics*, Vol. 26, 1987, pp. 851-867.

64. Li, F. Z., Shih, C. F., and Needleman, A., "A Comparison of Methods for Calculating Energy Release Rates." *Engineering Fracture Mechanics*, Vol. 21, No. 2, 1985, pp. 405-421.

65. Brust, F. W., McGowan, J. J., and Atluri, S. N., "A Combined Numerical/ Experimental Study of Ductile Crack Growth after a Large Unloading using *T**, *J*, and *CTOA* Criteria." *Engineering Fracture Mechanics*, Vol. 23, No. 3, 1986, pp. 537-550.

66. Narasimham, R., and Rosakis, A. J., "Three-Dimensional Effects Near a Crack Tip in a Ductile Three-Point Bend Specimen: Part I-A Numerical Investigation." *Journal of Applied Mechanics*, Vol. 57, 1990, pp. 607-617.

67. Okada, H. and Atluri, S. N., "A Further Study on the Near Tip Integral Parameter T^*_{ε} in Stable Crack Propagation in Thin Ductile Plate." *Proc. Of Aerospace Division*, ASME AD-Vol. 52, Chang, J. C. L. et al, Eds. 1996, pp. 281-288.

68. Wang, L., Brust, F. W., and Atluri, S. N., "The Elastic-Plastic Finite Element Alternating Method (EPFEAM) and the Prediction of Fracture under WFD Conditions in Aircraft Structures. Part I: EPFEAM Theory." *Computational Mechanics*, Vol. 19, 1997, pp. 356-369.

69. Nikishkov, G. P., and Atluri, S. N., "An Analytical-Numerical Alternating Method for Elastic-Plastic Analysis of Cracks." *Computational Mechanics*, Vol. 13, No. 6, 1994, pp. 427-442.

70. Okada, H., Atluri, S. N., Omori, Y., and Kobayashi, A. S., "Direct Evaluation of T^*_{ε} Integral From Experimentally Measured Near Tip Displacement Field, for A Plate With Stably Propagating Crack." *International Journal of Plasticity*, Vol. 15, 1999, pp. 869-897.

71. Omori, Y., Okada, H., Ma, L., Atluri, S. N., and Kobayashi, A. S., "T^*_ε Integral Under Plane Stress Crack Growth." *Fatigue and Fracture Mechanics, 27th Volume, ASTM STP 1296*, Piascik, R. S., Newman, J. C., and Dowling, N. E., Eds., American Society for Testing and Materials, 1997, pp. 61-71.

72. Omori, Y., Kobayashi, A. S., Okada, H., Atluri, S. N., and Tan, P., "T^*_ε Integral Analysis of Aluminum Specimens." *Proceedings of Aerospace Division, ASME AD-Vol. 52*, Chang, J. D. L., et al, Eds., 1996, pp. 281-288.

73. Walker, C. and MacKenzie, P., "The Assessment of the *T** Fracture Parameter During Creep Relaxation.", *unpublished conference proceedings*, Strathclyde University, U. K., 1998.

74. Brust, F. W., "Investigations of High Temperature Deformation and Crack Growth Under Variable Load Histories." *International Journal of Solids and Structures*, Vol. 32, No. 15, 1995, pp. 2191-2218.

75. Newman, J. C. Jr., and Raju, I. S., "Analysis of Surface Cracks in Finite Plates under Tension, or Bending Loads." *NASA TP 1578*, National Aeronautics and Space Administration, Washington D. C., 1979.

76. Shah, R. C., and Kobayashi, A. S., "Stress Intensity Factor for an Elliptical Crack Approaching the Surface of a Plate in Bending." *Stress Analysis and Growth of Cracks, ASTM STP 513*, American Society for Testing and Materials, Philadelphia, 1972, pp. 3-21.

77. Dodds, R. H. Jr., Carpenter, W. C., and Sorem, W. A., "Numerical Evaluation of a 3-D *J*-Integral and Comparison with Experimental Results for a 3-point Bend Specimen." *Engineering Fracture Mechanics*, Vol. 29, No. 3, 1988, pp. 275-285.

78. Amestoy, M., Bui, H. D., and Labbens, R., "On the Definition of Local Path Independent Integrals in Three-Dimensional Crack Problems." *Mechanics Research Communications*, Vol. 8, No. 4, 1981, pp. 231-236.

79. Raynund, M., and Palusamy, S. S., "*J*-integral for 3-D With Center-Cracked Plate Tests." *Computers and Structures*, Vol. 13, 1981, pp. 691-697.

80. Sakata, M., Aoki, S., Kishimoto, K., and Takagi, R., "Distribution of Crack Extension Force, the $\hat{J}$-integral, Along a Through-Crack-Front of a Plate." *International Journal of Fracture*, Vol. 23, 1983, pp. 187-200.

81. Carpenter, W. C., Read, D. T., and Dodds, R. H., "Comparison of Several Path Independent Integrals Including Plasticity Effects." *International Journal of Fracture*, Vol. 31, 1986, pp. 303-323.

82. De Lorenzi, H. G., "On the Energy Release Rate and the *J*-integral for 3-D Crack Configurations." *International Journal of Fracture*, Vol. 19, 1982, pp. 183-193.

83. Sumpter, J. D., and Turner, C. E., "Method of Laboratory Determination of J_C." *ASTM STP 601*, American Society for Testing and Materials, 1976, pp. 3-18.

84. Shih, C. F., Moran, B., and Nakamura, T., "Energy Release Rate Along a Three-Dimensional Crack Front in a Thermally Stressed Body." *International Journal of Fracture*, Vol. 30, 1986, pp. 79-102.

85. Parks, D.M., "The Virtual Crack Extension Method for Nonlinear Material Behavior." *Computer Methods in Applied Mechanics and Engineering*, Vol. 12, 1977, pp. 353-364.

86. Nikishkov, G. P., and Atluri, S. N., "Calculation of Fracture Mechanics Parameters for an Arbitrary Three-Dimensional Crack, By the 'Equivalent Domain Integral' Method." *International Journal For Numerical Methods In Engineering,* Vol. 24, 1987, pp. 1801-1821.

87. Dodds, R. H. Jr., Read, D. T., "Experimental and Numerical Studies of the *J*-Integral for a Surface Flaw." *International Journal of Fracture*, Vol. 43, 1990, pp. 47-67.

88. Kolednik, O., Yan, W. Y., Shan, G. X., and Fischer, F. D., "Tridimensional FE-Analysis of Stable Crack Growth in a CT-Specimen of a Structural Steel." *Proceedings of the ASME Aerospace Division*, AD-Vol. 52, Chang, J. C. I., et al, Eds., American Society of Mechanical Engineers, 1996.

89. Ohgi, J., and Hatanaka, K., "Assessment of *J*-integral for Three-Dimensional Surface Crack at Notch Root." *JSME International Journal*, Series A., Vol. 40, No. 3, 1997, pp. 290-297.

90. Zehnder, A. T., and Rosakis, A. J., "Three-Dimensional Effects Near a Crack Tip in a Ductile Three-Point Bend Specimen: Part II—An Experimental Investigation Using Interferometry and Caustics." *Journal of Applied Mechanics*, Vol. 57, 1990, pp. 618-626.

91. Jackson, J. H., *Characterization of the T^*_ε Integral Under Stable Crack Growth Conditions*, Master's Thesis, University of Washington, 1998.

92. Ma, L., *Crack Link Up and Residual Strength of Aircraft Structures Containing Multiple Site Damage*, Ph.D. Dissertation, University of Washington, 1999.

93. Woldemicheal, B., *T^*_ε Integral Analysis Under Conditions of Low-Cycle Fatigue Crack Growth*, Master's Thesis, University of Washington, 1998.

94. Lam, P. W., Kobayashi, A. S., Okada, H., Atluri, S. N., and Tan, P. W., "T^*_ε Integral for Curved Crack Growth." *Proceedings of FAA/NASA Symposium on Continued Airworthiness of Aircraft Structures*, Vol. II, Bigelow, C. A., Ed., DOT/FAA/AR-97-2, 1997, pp. 643-653.

95. Ghadiali, N. D., and Brust, F. W., "Final Report on TSTAR Software to Thiokol Corporation." *Battelle, Columbus Laboratories*, 1989.

96. Hinton, E., Scott, F. C., and Ricketts, R. E., "Local Least Squares Stress Smoothing For Parabolic Isoparametric Elements." *International Journal For Numerical Methods in Engineering*, vol. 9, 1975, pp. 235-256.

97. *ABAQUS Theory Manual V. 5.8*, Hibbit, Karlsson & Sorenson, Inc., 1998.

98. Post, D., "Moiré Interferometry." *Handbook on Experimental Mechanics, 2nd Edition*, Kobayashi, A. S., Ed., Society for Experimental Mechanics, 1993, pp. 297-364.

99. Ifju, P., and Post, D., "Zero-Thickness Specimen Gratings for Moiré Interferometry." *Experimental Techniques*, Vol. 15, No. 2, 1991, pp. 45-47.

100. Wang, F. X., May, G. B., and Kobayashi, A. S., "Low-Spatial-Frequency Steep Grating for Use in Moiré Interferometry." *Optical Engineering*, Vol. 33, No. 4, 1994, pp. 1125-1131.

101. Santana, L. F., "Experimental Characterization of Stable Crack Tearing in 4130 Steel Center Cracked Tension Specimen." *Master's Thesis*, University of Washington, 1997, p. 61.

102. Kokaly, M. T., Omori, Y., Kobayashi, A. S., Atluri, S. N., and Tan, P. W., "T^*_ε as a Low-Cycle Fatigue Crack Growth Parameter." *Fatigue in New and Aging Aircraft*, Poole, P., and Cooke, R., Eds., EMAS Publishing, 1997, pp. 155-164.

103. “Aluminum 2024-T3 Properties” *http://www.matweb.com*, 1999.

104. Mendelson, Alexander, *Plasticity: Theory and Application,* Krieger Publishing Company, Malabar, Fl., 1968.

105. *Damage Tolerant Design Handbook,* Metals And Ceramics Information Center, Battelle Columbus Laboratories, Columbus, OH., 1975.

APPENDIX A: EXPERIMENTAL SETUP WITH MOIRE BENCH

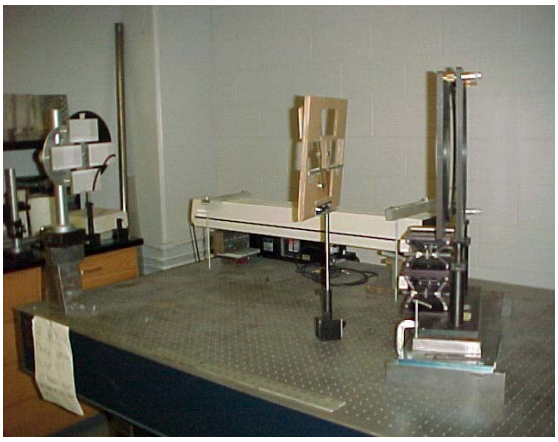

Figure A1: Moire bench with redirecting mirrors, mask, and collimating lens.

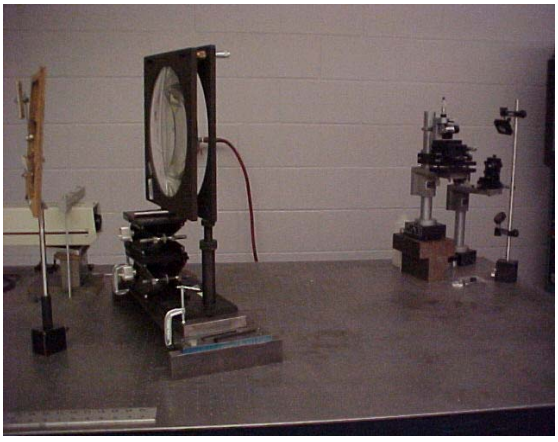

Figure A2: Spatial filter assembly in front of collimating lens.

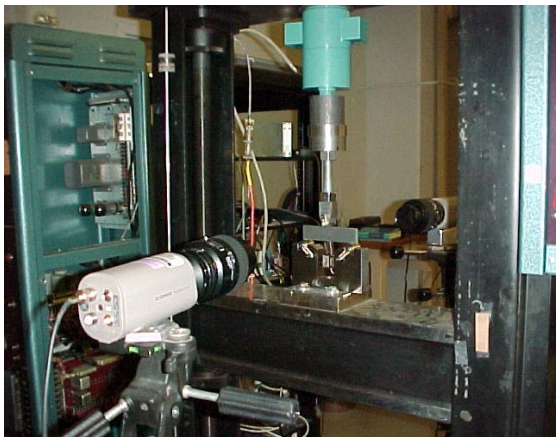

Figure A3: Front view of specimen in load frame, and front camera.

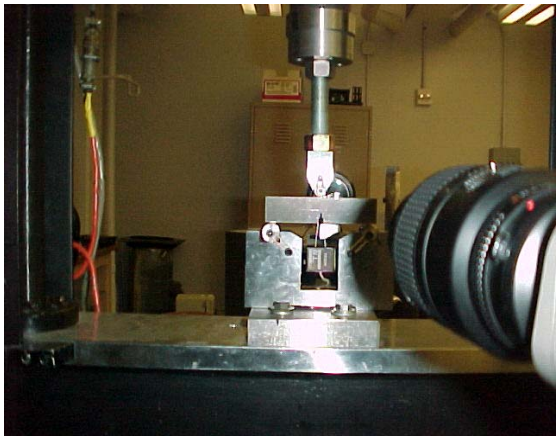

Figure A4: Closeup view of specimen with CMOD gage attached.